Local metabolism in preclinical disease models studied with mass spectrometry imaging

Local metabolism
in preclinical disease models studied with
mass spectrometry imaging

Jian-Hua Cao

Local metabolism
in preclinical disease models
studied with
mass spectrometry imaging

DISSERTATION

To obtain the degree of doctor at Maastricht University,

on the authority of the Rector Magnificus

Prof. dr. Pamela Habibović,

in accordance with the decision of the Board of Deans,

to be defended in public on

Thursday the 6th of October 2022 at 10.00 hours

By

Jian-Hua Cao

Promotor

Prof. dr. Ron M.A Heeren

Co-promotor

Dr. Benjamin Balluff

Assessment Committee

Prof. dr. Maarten Honing (Chairman)

Prof. dr. Daisy Jonkers

Prof. dr. Ronit Sverdlov

Prof. dr. Gijs van Soest, Erasmus University

Prof. dr. Per Andren, Uppsala University

Maastricht University *Leading in Learning!*

CONTENTS

Prologue

Many complex multicellular organisms are made up of one or more organs where different organs work together as a unit to maintain an organism functioning. Each organ is composed of distinct tissues. A tissue is an ensemble of cells that interlinked with each other accomplishes a specific function. Within a cell, thousands of different life-sustaining chemical reactions are constantly taking place to keep the living state of the cell and the entire organism. The sum of all these reactions is referred to as metabolism. Dysregulations in these metabolic reactions constitute a global health problem as they can be found in many diseases such as obesity, diabetes, chronic kidney disease, cardiovascular diseases, cancer, cognitive disorders, and respiratory pathologies.

Metabolites are small molecules (<1.5 KDa) such as lipids, amino acids, sugars, organic acids, nucleotides, small peptides, vitamins and hormones, all of which constitute intermediates or end products in the cellular metabolism. These metabolic processes are dynamic and complex, and are influenced by many environmental and lifestyle factors, such as diet, medication, stress, physical activity, or the microbiome within an organism. The latest release of the Human Metabolome Database (https://hmdb.ca) lists not less than 114,000 different metabolites. Obtaining an overview of all metabolites and their levels at the different places in an organism is therefore an extremely challenging endeavor in biomedical research.

In that context, *metabolomics* aims at comprehensively studying metabolites in a biological system (i.e. in a cell, tissue, organ, biofluid, or organism) using high-throughput technologies, thus providing a systematic readout of the metabolic status of an individual mostly in relation to genetic and changing environmental conditions. In general, metabolomics can be divided into targeted and non-targeted metabolomics. Non-targeted metabolomics typically aims to comprehensively analyze all measurable known/unknown metabolites in a sample, while targeted metabolomics attempts to detect and quantify a predefined set of metabolites. While the first approach is more advantageous in a discovery scenario, the latter approach is characterized by a higher specificity, sensitivity, and accuracy in determining the real abundances in a sample.

Mass spectrometry (MS) is one of the most extensively used analytical techniques for metabolomics studies, where a molecular profile of a sample can be created through the separation of the metabolites based on their mass-to-charge ratio (*m/z*). In order to achieve this, a mass spectrometer consists of three major components: an ion source, a mass analyzer, and a detector. An ion source is used to electrically charge the metabolites in a sample. A mass analyzer then separates the ionized molecules based on their mass-to-charge ratios. A detector subsequently generates a signal from these separated ions, where the intensity of that signal corresponds to the number of ions. The results are typically presented as a mass spectrum, a graph of the ion abundance (y-axis) versus the mass-to-charge ratio (x-axis).

MS coupled with chromatographic separation techniques such as liquid chromatography mass spectrometry (LC-MS) or gas chromatography mass spectrometry (GC-MS) are the most extensively used strategies for metabolomics analyses. However, these approaches

involve a metabolite extraction step from the sample. Unlike biofluids, tissue samples are preceded by an additional homogenization pretreatment. This leads, unfortunately, to the loss of the spatial localization of the metabolites in the target tissue sample and in consequence also to the loss of the possibility to assign metabolic profiles to the different cell-types. The latter is however required since most of biological tissues are made of many different cell types which are spatially highly organized and structured to perform their dedicated function. Therefore, the spatial information of metabolites in heterogeneous cell populations is indispensable to reveal and understand the complexity of disease mechanisms. Consequently, it is important to study metabolites locally on tissue using methodologies that analyze the samples in a spatially resolved manner such as offered by imaging technologies.

In order to combine the advantages of MS while maintaining the tissue's structure, mass spectrometry imaging (MSI) has been conceived. It is a family of mass spectrometry-based imaging techniques for the simultaneous *in situ* mapping of a wide range of molecules while preserving the morphological integrity of the analyzed tissue; hence an approach which captures both the spatial as well as the molecular complexity of biological tissues. All MSI techniques require a desorption and ionization probe which rasters across a tissue sample surface in a pixel-by-pixel manner. At each measurement position, desorbed and ionized molecular species are created locally and analyzed by the MS system. In this way, a mass spectrum is generated at each measurement coordinate. This set of mass spectra allows the reconstruction of molecular images by showing the abundance of each *m/z* value as a function of each spectrum's coordinate across the rastered sample.

As mentioned, MSI is a family of techniques, whose members distinguish themselves by the use of different *in situ* ionization mechanisms. Of all techniques, matrix-assisted laser desorption/ionization (MALDI) is the most commonly employed ionization technology in MSI since it provides the best trade-off between spatial resolution (nowadays at single cell level) and the range of detectable molecular classes, which range from metabolites to proteins.

While MALDI-MSI has been widely applied in biomedical studies to molecularly characterize different tissue-based pathologies, it is an underexplored technique in atherosclerosis, wound healing, and dynamics of cancer metabolism. In all of these fields of research, animal models are an indispensable tool to investigate the complex molecular mechanisms of these diseases. Among them, mice and rats are the most widely used animal species due to their friendly cost, small size, and prompt reproduction. These allow researchers to carry out dynamic MSI studies over time, where each time point – due to the invasive nature of the technology – usually corresponds to one animal, unless multiple tissue sampling is possible from one subject, e.g. as offered by fine-needle aspiration. In atherosclerosis studies, the genetically manipulated mouse models are the most frequently employed species, whereas in preclinical cancer research, the human tumor xenograft murine model is one of the preferred animal models due to its similarity to real human tumors. In contrast, for studies of surgical interventions, such as studies on wound healing, larger

animals, such as rats, rabbits or pigs, are preferred models over mice owing to the fact that surgery is generally easier in larger sized animals.

In summary, metabolites constitute an extremely complex and rich molecular class, which – combined with the spatial complexity of tissues – makes their investigation extremely difficult. In this context, it is important to study these diseases with a spatial metabolomics approach. Furthermore, metabolic processes are not only very localized, but also systemic and dynamic. Therefore, in order to obtain a more complete picture of these metabolic processes, it is important to do multiple sampling from different places (organs) and over time (Figure 1), which is in general only possible in animals.
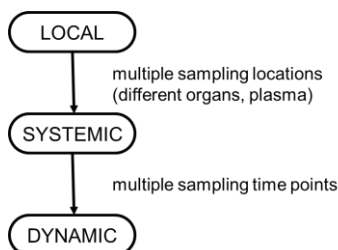
Figure 1. The workflow for obtaining a full metabolism picture.

Therefore, the work presented in this thesis concentrates on the investigation of the local metabolism in atherosclerosis, wound healing, and cancer using animal models and MALDI mass spectrometry imaging for spatial metabolomics (Figure 2).
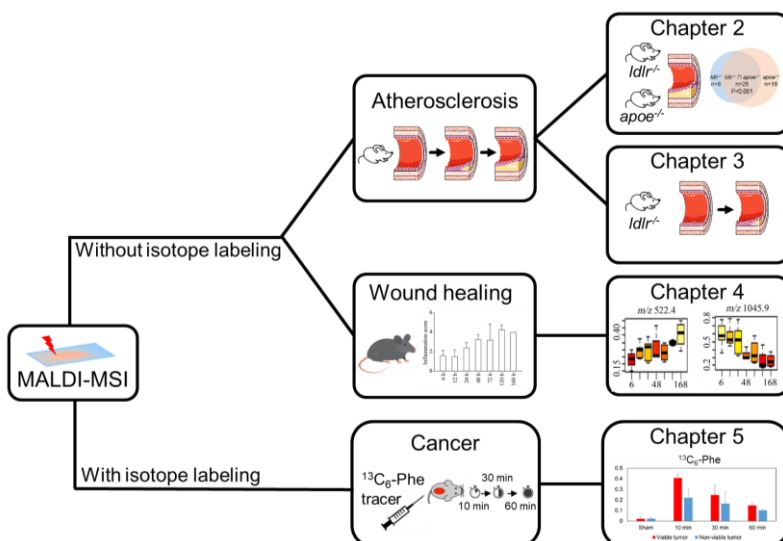
Figure 2. The overview of all experimental chapters in this thesis.

In **chapters 2** and **3** of this thesis, untargeted metabolomics on atherosclerotic tissues from transgenic mice is applied. Of note, in **chapter 2**, high-spatial-resolution 2-dimensional and

three-dimensional MALDI-MSI were used to identify aortic plaque-specific lipids in both low density lipoprotein receptor deficient ($ldlr^{-/-}$) mice and apolipoprotein E deficient ($apoe^{-/-}$) mice, the two of the most widely studied mouse models for atherosclerosis. **Chapter 3** complements **chapter 2** by focusing on metabolomic alterations and atherogenesis. Therefore, I applied untargeted MALDI-MSI metabolomics on aortic tissue using the $ldlr^{-/-}$ mouse model fed with high fat diet compared to control mice fed with normal diet. In **chapter 4**, abdominal fascia healing in the first postoperative week in a rat model using untargeted MALDI-MSI metabolomics is investigated.

Most of targeted MALDI-MSI metabolomics studies mainly focus on imaging the accumulation of drugs, toxicants and their metabolites in different tissues and thereby to investigate their pharmacological/toxicological effects. Combining MSI and stable isotope labeling of metabolites administered to the living animal can reveal spatially resolved dynamics of molecule synthesis and turn over occurring in different cellular compartments and organs. This adds an extra dimension to the comprehensive description of the metabolism, deepening our understanding of dysregulated metabolism in many diseases. However, in terms of isotopic labeled targeted metabolomics, MSI remains underexplored. This is the reason in **chapter 5** of this thesis, why I investigated the local ^{13}C-labeled L-phenylalanine metabolism in a human non-small cell lung carcinoma xenografted mouse model in the context of cancer tissue morphology using MALDI-MSI.

All of these efforts give evidence for the usefulness of MSI applied to animal models to capture the local and systemic dynamics of disease metabolism in cancer, wound healing, and atherosclerosis. While all studies have technically been based on non-targeted MS, translating the results to a clinical scenario using targeted approaches harbors great potential for disease diagnostics. In that line, I investigated in **chapter 3** if and how results from non-targeted MSI can be exploited by targeted SRM-MS in human plasma samples. Finally, some of the experimental strategies shown can also serve as blueprint for the study of other diseases.

.

Chapter 1

General introduction

1. Metabolomics

All living organisms are composed of one or more cells. Cells are dynamic machines that constantly operate sequences of biochemical reactions to maintain every organism alive and healthy. The sum of all the life-sustaining reactions in an organism is called metabolism (from Greek: μεταβολή, meaning "change") [1]. Metabolic reactions (Figure 1.1) can be categorized as catabolic (the degradation of compounds which releases energy) or anabolic (the synthesis of molecules which consumes energy) [1]. Metabolites are low molecular weight (< 1500 Da) compounds which are the reactants, intermediates, or products of metabolic reactions [2]. To date, over 8,700 metabolic reactions and 16,000 metabolites have been annotated in the Kyoto Encyclopedia of Genes and Genomes (KEGG) database [3].
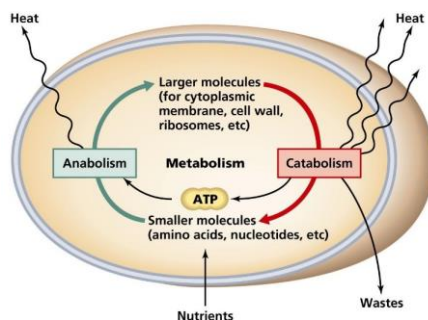
Figure 1.1 Simple scheme of cellular metabolism. Anabolism is the synthesis of lager molecules from smaller units accompanied by the absorption of energy, whereas catabolism breaks down large molecules into smaller ones together with releasing energy. Adenosine triphosphate (ATP) is the main energy source for most cellular activities. This figure has been reproduced from *https://wingsnfitness.wordpress.com*.

Metabolites can be endogenous compounds such as lipids, non-essential amino acids, short peptides, nucleic acids, sugars, alcohols, vitamins or organic acids that are routinely produced by endogenous catabolism or anabolism [4]. Endogenous metabolites are the building blocks for all other biochemical species and structures including proteins (e.g. amino acids), genes and transcripts (e.g. nucleotides), and cell walls (e.g. lipids) [2]; they are key components in essentially every cellular process and cellular function [1]. For example, lipids constitute approximately 50% of the mass of cell membranes and play essential roles as building blocks of the cellular membrane bilayer (e.g. phospholipids and cholesterol), regulate the cellular membrane fluidity (e.g. cholesterol), are involved in cell signaling pathways (such as prostaglandins and leukotrienes), and constitute energy resources (triacylglycerol esters and steryl esters) [5]. Amino acids are the principle building blocks of polypeptides and proteins. They also serve as key precursors to many biologically active molecules, such as hormones [6] and neurotransmitters (e.g. dopamine and epinephrine) [7]. Amino acids play important roles in homeostasis, cell signaling, gene expression, and antioxidative responses [8]. In addition to endogenous metabolites, the category of metabolites can also include xenobiotic compounds coming from the diet or the environment, such as food additives, prescription drugs, microbial byproducts, cosmetic chemicals, chemical contaminants, and pollutants [4].

The wide range of metabolites results in a large diversity of chemical properties such as molecular weight, concentration, polarity, solubility. Additionally, unlike genes or proteins, which can change in fluctuating environments within minutes to hours [9], metabolites can respond to environmental influences in seconds or even milliseconds [9], thus metabolites are also characterized by a ultrahigh degree of dynamics. In the same context, abnormal changes in the level of metabolites can be caused by genetic or environmental factors, as well as diseases, exposure to microbiota, drugs, toxins, etc. [10]. Alterations in metabolite levels have been reported in a myriad of global health problems including obesity, diabetes, chronic kidney disease, cardiovascular diseases, cancer, cognitive disorders, and respiratory pathologies [11]. For instance, diabetes mellitus is characterized by an excessive blood glucose level. Similarly, elevated levels of blood lipids (e.g. cholesterol and triglyceride) are well documented risk factors for several cardiovascular diseases (CVD) [12] and dysregulated glucose and glutamine metabolism is a well-known hallmark of cancer cells [13].

The complete number of metabolites that exist in a human is still not known and poses an immense analytical challenge due to the complexity and diversity of metabolites [14]. The total number of metabolites in the latest release of the Human Metabolome Database (HMDB 4.0) has been expanded from 40,153 (HMDB 3.0) to 114,100 [15]. Therefore, high throughput analysis is highly required to comprehensively study metabolites within a biological system. The large-scale study of metabolites present within a given biological system (e.g. biofluids, organelles, cells, tissues, organs and organisms) is referred to as metabolomics [2]. Metabolomics studies show great potential in discovering novel candidate biomarkers and understanding biochemical pathways for gaining insights into the pathogenesis, progression and diagnosis of diseases [10]. Mass spectrometry (MS) is one of the most sensitive and extensively used analytical techniques for metabolomics studies [16].

2. Mass Spectrometry

Mass spectrometry (MS) measures the mass-to-charge ratio (m/z where m refers to the molecular weight and z to the number of charges of the molecule) of molecules present in a sample. The results are typically presented as a mass spectrum, a graph of the ion abundance versus the mass-to-charge ratio. The first mass spectrum was obtained a century ago by the physicist Joseph John Thomson, who separated the two isotopes of Neon (^{20}Ne and ^{22}Ne) by their mass [17]. Nowadays, applications of MS have been expended exponentially from physics to chemistry and biology [18].
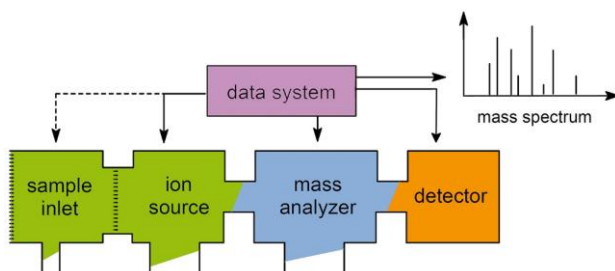
Figure 1.2. A mass spectrometer is composed of a sample inlet, an ion source, a mass analyzer and a mass detector. The data system is utilized for collecting and processing data from the mass detector. This figure has been reproduced from *http://wp.ms-textbook.com*.

In a typical MS setup (Figure 1.2), a sample, which can be solid, liquid or gaseous, is introduced into the mass spectrometer through a sample inlet. Then the molecules from the sample are converted to ions by the ionization source. Once formed, ions are electrostatically propelled into the mass analyzer where they are separated according to their *m/z* values. The detector converts the ions' energy into electrical signals, which are then amplified and digitalized to store the mass spectrum on a computer.

Nowadays, mass spectrometry offers the multiplex analysis of many molecules simultaneously with high sensitivity (at the attomol to femtomol level) [19] and selectivity [20] due to the ability of determining a molecule's identity based on high-mass resolving power and/or its specific fragmentation pattern. The latter can also aid in separating isomeric or isobaric species. Moreover, combining MS with a chromatographic separation technique such as liquid chromatography (LC) or gas chromatography (GC) [10] reduces the complexity of a sample by separating its compounds based on their retention time within the chromatographic column [10]. Adding the retention time as additional dimension, greatly improves the sensitivity of mass spectrometric experiments, especially for biological samples (e.g. biofluids and tissues), which are characterized by a high chemical complexity in terms of number of different compounds and their dynamic range of concentrations. However, these chromatographic approaches require the sample in solution. To extend these types of analyses to tissue samples, it is needed to homogenize them before analysis, which leads to the loss of the spatial localization of the molecules in the target tissue.

This thesis mainly focuses on tissue samples and most biological tissues are characterized by a high cellular heterogeneity [21]. Different cell types exhibit widely distinct morphologies, phenotypes, and functions [21, 22] based on an extensive molecular variability [23, 24]. Moreover, cells from the same genus can vary in membrane composition with symmetrical distribution [25]. This molecular and cellular heterogeneity is crucial in understanding the biological complexity of diseases [26]. Therefore, in the context of biological tissue samples, comprehensively profiling molecules while maintaining their specific spatial information at the cellular level is pivotal to fully unravel molecular and spatial complexity of various biological and pathological processes. While laser capture microdissection is typically used

to isolate specific groups of cells from target tissue for further extraction-based molecular analysis [27], this method is time-consuming and is based on known tissue dyes, thus it is not the perfect approach for metabolomics analysis with discovery character.

In contrast, modern imaging techniques such as fluorescence microscopy, magnetic resonance imaging (MRI), near-infrared imaging and positron emission tomography (PET) enable deliver spatially resolved information of targeted molecules with high sensitivity, but these techniques require the prior knowledge of the target analytes and lack multiplex capabilities (only a small number of observable molecules at any given time) [28], thus they are unsuited for discovery-based research. Additionally, the spatial resolution of several molecular imaging modalities such as PET and MRI is limited to the millimeter scale, thus they are not able to provide spatial information of molecules at cellular (micrometer) level. In contrast, mass spectrometry imaging (MSI) has the ability of simultaneous imaging thousands of molecules in different cell types throughout a tissue section in a label-free manner, where *a priori* knowledge of their presence is not required.

3. Mass spectrometry imaging

Mass spectrometry imaging (MSI) is an imaging technology that makes it possible to *in situ* detect simultaneously a broad range of molecules present in tissue without the need for prior knowledge of the analytes (Figure 1.3), thus it captures both spatial and molecular complexity of biological tissues. This enables visualizing many different metabolites in the tissue, which is suited for both preclinical and clinical discovery-based studies [29].

There are different MSI techniques all of which require a desorption and ionization probe to continuously move over a sample's surface in order to locally desorb and ionize molecular species. These ions are subsequently separated according to their mass-to-charge ratio (*m/z*) inside the mass analyzer. There are different types of mass analyzers such as a magnetic sectors, time of flight (TOF), quadrupoles, ion traps, or Fourier transform ion cyclotron resonance (FTICR) mass analyzers. The ions are then detected by a detector, such as an electron multiplier. In this way, a mass spectrum is generated at each measurement coordinate [30]. An image of a selected *m/z* species can then be reconstructed by plotting the intensity as a function of the spatial coordinates, which were recorded during the acquisition. This provides the spatial distribution and abundance information of all detected molecules (based on its known *m/z* value) within the sample (Figure 1.3).
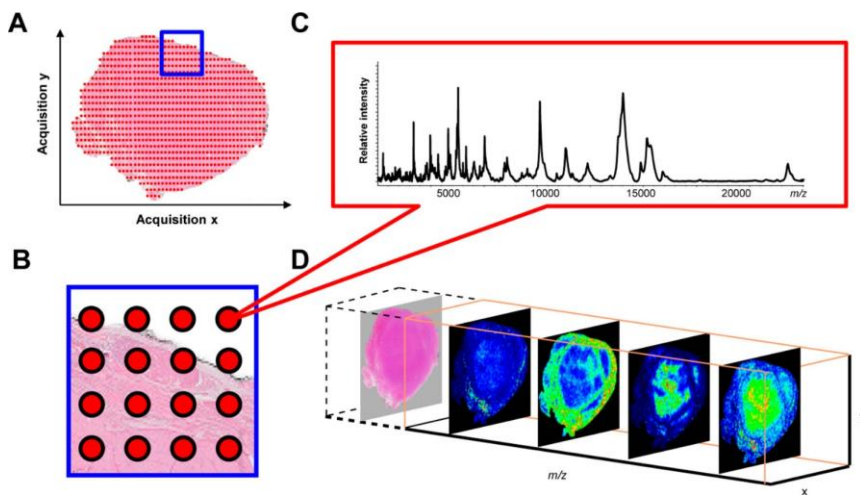
Figure 1.3. The fundamentals of mass spectrometry imaging (MSI). An MSI experiment is performed in an (x, y) grid-wise manner across the surface of the targeted tissue section, and mass spectrum of every measuring raster spot is acquired. This results in any mass signal (*m/z*) in each mass spectrum can be spatially mapped. The exact same tissue section can thereafter be stained histologically (e.g. hematoxylin and eosin staining) and co-registered with the MSI data. This figure has been reproduced from [31].

MSI has originally been developed for imaging elements and small molecular fragments on complex semiconductor surfaces using secondary ion mass spectrometry (SIMS) in the early 1960s [32]. Around 25 years later, two different ionization methods including matrix-assisted laser desorption/ionization (MALDI) and electrospray ionization (ESI) were introduced consecutively for analyzing intact macromolecules [32]. In the late 1990s, MSI based on MALDI was applied to visualize intact proteins directly on tissue samples for the first time [33]. Over the past decades, MALDI-MSI has been quickly and successfully expanded to image a wide variety of low-molecular weight compounds such as metabolites or drugs on different tissue samples [18, 30]. In addition to SIMS and MALDI, another ionization method, desorption electrospray ionization (DESI), entered the field of MSI. DESI has been developed by Cooks and coworkers in 2004 [34] and can be employed for MSI under ambient environment [34]. Nowadays, MALDI is the most popular ionization approach for MSI on tissue samples due to its broad molecular coverage (from small molecules to macromolecules) [18] and versatility in spatial resolution (down to single cell resolution) [35]. In the following section, I will briefly introduce the principle of these three main ionization techniques (Figure 1.4) for MSI with a focus on MALDI-MSI.

Figure 1.4. The most common used ionization approaches. (a) Matrix-assisted laser desorption/ionization (MALDI) is a soft ionization technique that involves an organic matrix that absorbs the energy from the irradiated laser (e.g. ultraviolet laser) and facilitates analyte and matrix molecules converted into gas phase ions to be analysed by the mass spectrometer. (b) Desorption electrospray ionization (DESI) is an ambient ionization technique that employs a fast-moving charged solvent spray to extract analytes from the specimen and transfer them to the mass spectrometer inlet. (c) Secondary ion mass spectrometry (SIMS) uses a focused and high-energy primary ion beam to locally generate secondary ions for introduction to a mass analyzer. This figure has been reproduced from [30].

3.1 SIMS-MSI

Secondary ion mass spectrometry (SIMS) is a desorption and ionization technique which employs a focused, high-energy primary ion beam (e.g. Bi^+, Au^+, C_{60}^+, Bi_3^+, Ar_{700}^+, $(H_2O)_n^+$ etc.) to generate secondary ions upon impact of the primary ion beam from the specimen surface (Figure 1.4c) [18]. These secondary ions are subsequently accelerated and introduced to a mass analyzer (most commonly TOF) for their separation [18, 36]. This ionization method offers the highest lateral spatial resolution (<100 nm) [37, 38]. However, the typical energy (5-25 eV) of the primary ion beam is substantially higher than usual bond energies of the molecules [18]. Consequently, it will cause extensive fragmentation of the ionized molecules, thus its sensitivity is limited to ions below m/z 1000 [18]. Therefore, SIMS mass spectrometry imaging is very suitable for detecting elemental ions, stable metabolites and lipids up to 1000 m/z at the cellular and subcellular level [39].

3.2 DESI-MSI

Desorption electrospray ionization (DESI) is an ambient ionization method, combining both electrospray ionization (ESI) and desorption ionization [18]. DESI deploys a charged solvent spray onto the sample surface to desorb and ionize molecules (Figure 1.4b) [40]. The solvent composition determines the targeted molecular classes. It is commonly used for detecting drugs and metabolites in tissues under ambient conditions [40, 41]. It also used for samples that do not tolerate a vacuum environment, and for molecules, which could not be ionized using SIMS or MALDI [42]. However, the spatial resolution is limited for DESI-MSI (usually 50-200 µm), and the DESI-MSI image might suffer from significant delocalization due to the wetted surface using solvent droplets [43].

3.3 MALDI-MSI

Matrix-assisted laser desorption/ionization (MALDI) is the most commonly employed ionization technology in MSI [44]. It allows spatially resolved analysis intact proteins,

peptides, glycans, lipids, metabolites and drugs from a wide range of specimens, e.g. single cells [45], microorganisms [46], human [30], animal [47], and plant tissues [48] as well as fruits [49]. MALDI (Figure 1.4a) is a soft ionization method that utilizes a pulsed laser beam such as a nitrogen laser (337 nm) or neodymium-doped yttrium aluminum garnet (355 nm) in combination with an energy-absorbing matrix crystals [18]. Sample analytes are co-crystallized with the matrix reducing the direct interaction of the analytes with the laser. The matrix has conjugated double bonds which can efficiently absorb the majority of the laser energy and transfer this energy to the analytes, resulting in an explosive desorption of the analytes-matrix structure into the gas phase without significant degradation of the analytes [18]. Contrary to DESI, which produces multiply charged ions, MALDI mainly yields singly changed ions [18]. This ionization technique is usually coupled to a time of flight (TOF) or Fourier transform ion cyclotron resonance (FTICR) mass analyzer. These two mass analyzers are predominantly used in this thesis and will feature in the following section 3.4. The other different mass analyzers utilized for MSI have been extensively described elsewhere [18].

3.4 Mass analyzers

Time of flight mass analyzer

The time-of-flight (TOF) mass analyzer (Figure 1.5) was introduced in 1946 by Stephens *et al.* [50]. It uses an electric field (typically 2-25 kV) to one-directionally accelerate the ionized molecules with the same potential energy achieving theoretically at the end of the acceleration the same kinetic energy [51]. Given the same kinetic energy, molecules with different weights will have different velocities. This allows separating them and determining their molecular weight by measuring the time it takes the ions to travel a fixed-length (typically 1-2 meters) vacuum flight tube until reaching to the detector [18]. Modern MALDI-TOF mass spectrometers are commonly equipped with both linear and reflectron TOF analyzers. The linear TOF analyzer is able to detect ions over a very wide mass range with high sensitivity, which has been extensively applied for detecting proteins [18]. However, one of the drawbacks for linear TOF is poor mass resolution for lighter molecules, i.e. metabolites and lipids. It has been found that a reflectron can significantly improve the mass resolving power (R_M= m1/(m2−m1)), i.e. the ability to distinguish two adjacent mass spectral peaks of equal height and width, of a TOF analyzer [52]. The reflectron geometry uses an ion mirror at the end of the first flight tube thereby increasing the length of the "free flight" path, which enables compensating the initial kinetic energy distributions and therefore results in a better mass resolution [53]. The reflectron TOF (Figure 1.5) ($R_M=10^3$-10^4) [18] is commonly used for measuring glycans, metabolites, lipids and drugs. In this thesis, the reflectron TOF mass analyzer has been used in form of the rapifleX MALDI Tissuetyper™ (Bruker Daltonik, Bremen, Germany) in **chapters 2** and **4**.
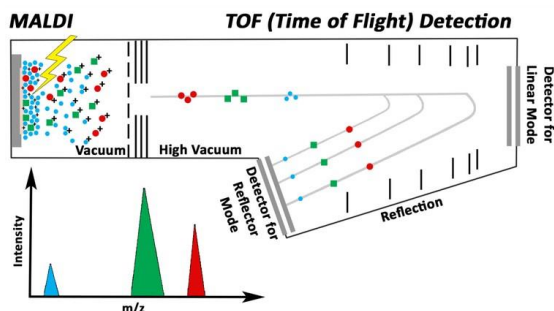
Figure 1.5. Principle of linear and reflectron time-of-flight (TOF) mass analyzer. All ionized molecules are accelerated by an electric field at a given strength to allow all ions have the same kinetic energy before traveling through a field-free drift region. In the linear mode, the ionized molecules are separated based on their time-of-flight they need to travel through the tube and arrive at the detector, which is widely used to separate heavier molecules such as proteins. In reflectron mode, ions with same mass but slightly different kinetic energies are aligned by an electric field at the end of the drift tube, which also reflects the ions to a second detector. This leads to a higher mass resolution, especially in the mass range of peptides and lipids. This figure has been reproduced from [54].
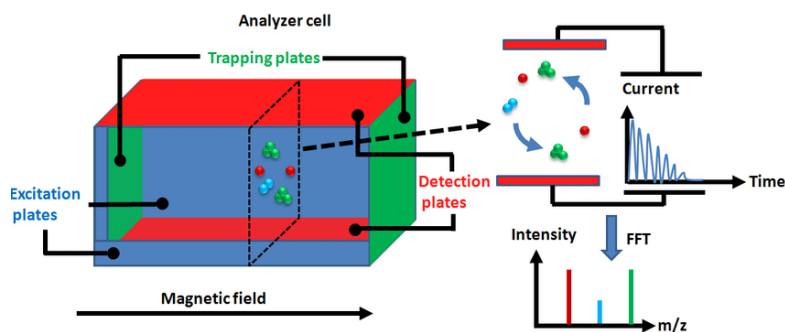
Figure 1.6. Schematic principle of the Fourier transform ion cyclotron resonance (FTICR) mass analyzer. Ionized analyzes are trapped inside an analyzer cell with a constant magnetic field where they are put in an orbital motion. During their orbit, ions induce a charge in the two detection electrodes. This time-domain ICR signal is digitized based on the voltage difference between the two detection electrodes as a function of time. After applying Fourier transform to this signal, the cyclotron frequency spectrum is yielded, which in turn can be converted into the corresponding mass spectrum. This figure has been reproduced from [55].

Fourier transform ion cyclotron resonance mass analyzer

Unlike TOF-MS, a FTICR mass analyzer (Figure 1.6) is a trapped ion technique which was first introduced in 1974 by Comisarow and Marshall [56] and currently provides ultra high mass resolving power ($R_M > 10^6$) and up to parts-per-billion mass accuracy [57]. It determines the *m/z* values of ions based on their cyclotron frequency in a fixed magnetic field. After ions are generated, ions are trapped electrostatically within the ion cyclotron resonance (ICR) cell, which typically comprises two trap electrodes, two excitation electrodes and two detection electrodes. Using a radio-frequency electrical pulse on the excitation electrodes, not only all ions are excited to a larger cyclotron radius but also ions with the same *m/z* value will start orbiting coherently. During their orbit, ions induce a charge in the two detection electrodes. This time-domain ICR signal is digitized based on the voltage difference between the two

detection electrodes as a function of time. After applying Fourier transform to this signal, a cyclotron frequency spectrum can be yielded, which in turn (based on a previous calibration) can be converted into a mass spectrum [58]. Thus, FTICR-MS has become an extremely powerful tool to identify metabolites directly based on their accurate mass alone [59] due to its ultra high mass resolution, mass accuracy and sensitivity. It has also been widely applied for other molecules such as proteins [60], lipids [57] and drugs [61]. In this thesis, the FTICR mass analyzer was used in form of a MALDI-FTICR instrument (Solarix, 9.4T, Bruker Daltonics, Bremen, Germany) for the detection of metabolites in **chapters 3** and **5**.

4. Experimental workflow of MALDI-MSI

Fresh frozen and formalin-fixed paraffin-embedded (FFPE) tissue samples are routinely used in MALDI-MSI. A typical workflow for an MALDI-MSI experiment (Figure 1.7) consists of sample preparation, matrix application, data acquisition, and data analysis [18]. Briefly, the first step is sectioning of the tissue to obtain a thin slice of the sample. The general thickness of fresh frozen and FFPE tissue sections for MSI is 5–20 μm and 2–7 μm, respectively [62]. Later, sections are placed onto conductive indium-tin-oxide coated glass slides. Depending on the targeted molecular class and tissue types, extra sample preparation steps are required prior to the matrix application step. For instance, for detecting peptides using MSI, several washing steps are recommended to reduce ion suppression caused by interfering molecule such as matrix or lipids [63]. This is then followed by coating the section homogeneously with a proteolytic (e.g. trypsin) enzyme solution and incubating it overnight in a humidity chamber [63]. In the case of protein-bound modifications such as glycans, enzymatic treatment such as utilizing peptide N-glycanase (PNGaseF) can release these modifications to be spatially mapped by MSI [64]. Moreover, the application of MALDI-MSI for FFPE tissues requires much more time-consuming steps (such as deparaffinization) before matrix coating, which have been described elsewhere [65-69].

Then the matrix is homogeneously brought onto the slides using either an automated sprayer system such as HTX sprayer [47] or by solvent-free sublimation [70]. After matrix application, the matrix coated tissue samples are introduced in the MALDI-MSI instrument; the laser beam with defined-repetition rate rasters across the surface of the matrix-covered samples. A mass spectrum is recorded at every measurement positions, which represents the molecular profile of that specific position. For modern MALDI-TOF instrument, the acquisition speed can reach 50 pixels per second using a 10 KHz Nd:YAG laser [71]. The spatial resolution or pixel size in commercial MALDI-TOF instruments is can go up to around 10 μm [71]. Moreover, Zavalin *et al.* have already pushed the limit of the spatial resolution to 1μm via a transmission geometry ion source [72].
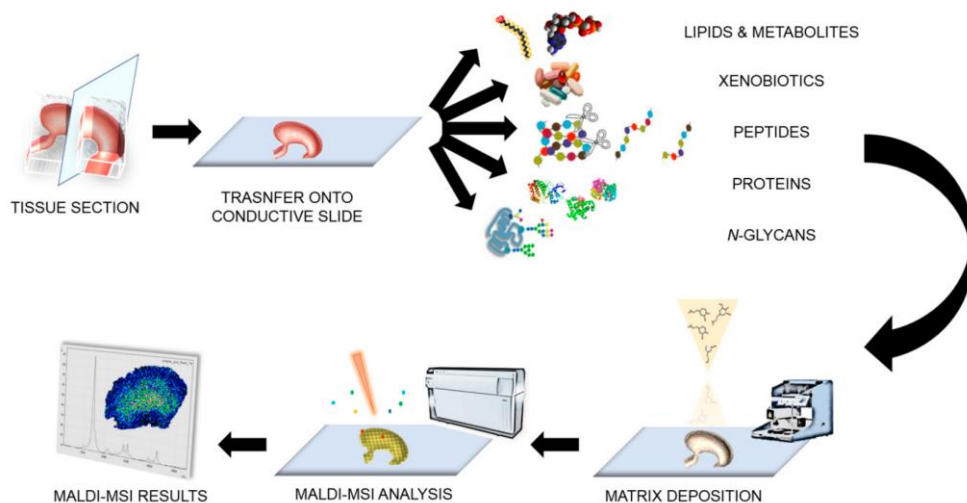
Figure 1.7. Schematic workflow of MALDI mass spectrometry imaging (MALDI-MSI). After tissue sectioning and sections are transferred onto a conductive glass slide and the matrix of choice (depends on the types of molecules targeted) is homogeneously brought onto the slide. Then the matrix coated tissue samples are introduced in a MALDI-MSI instrument and the laser beam with high-repetition rates is rastered across the surface. A mass spectrum is recorded at every raster position, which represents the molecule profile of that specific spot. In this way, the spatial distribution of each *m/z* signal can be visualized. This figure has been reproduced from [73].

After MALDI-MSI data acquisition, the residual matrix can be washed away and histopathological staining can be performed on the very same tissue section. After microscopic digitalization of the stained tissue section, image co-registration, pathological annotation, data analysis, and data interpretation performed [62]. In the following section of this chapter, I will describe the steps of MALDI-MSI for metabolomics studies in more detail, especially in terms of sample preparation and matrix deposition.

Sample preparation for metabolomics using MALDI-MSI

As mentioned earlier, metabolites are a molecular class of high compositional diversity (lipids, amino acids, sugars, etc.) and structural heterogeneity [2]. Consequently, they have a broad range of physicochemical properties (molecular weight, hydrophobicity/hydrophilicity, acidity/basicity) [2] and occur at a wide level of concentrations in living beings [74]. Mass spectrometry imaging of metabolites can therefore be challenging, especially since metabolites are also highly susceptible to post-mortem changes [75]. Hence, sample preparation, including sample collection and embedding, storage, tissue sectioning, on-tissue derivatization (targeted metabolomics), and matrix deposition are critical steps for the successful *in situ* analysis of metabolites in tissues by MALDI-MSI.

4.1. Sample collection and embedding

The first step for MALDI-MSI is sample collection. Right after sample collection, different stabilization approaches such as snap-freezing or heat-stabilization [75] can be applied to

stop all biological processes and preserve the sample's morphology as well as minimize molecular degradation for MSI [18]. The majority of tissue samples used in MALDI-MSI metabolomics' studies are fresh-frozen and stored at maximum −80 °C before cryo-sectioning. In some cases, tissues are too small to be easily and precisely sliced. To alleviate tissue sectioning of tiny tissues they need to be snap frozen in liquid nitrogen or isopropanol for 30−60 seconds [18], and then embedded into a solidifying medium, such as the optimal cutting temperature (OCT) polymer, 2% (wt/vol) carboxymethylcellulose, gelation or other embedding materials [18]. Formalin-fixed and paraffin-embedded (FFPE) tissue specimens have also been used for metabolomics studies with MALDI-MSI [65]. In this thesis, mouse aorta samples were embedded in OCT (**chapters 2** and **3**) and rat abdominal fascia tissues (**chapter 4**) and mouse tumor samples (**chapter 5**) were fresh frozen without a further embedding due to their manageable size.

4.2. Tissue cryo-sectioning

The next step for MALDI-MSI is tissue sectioning. The sectioning temperature is typically between -5 and -25 °C, depending on the tissue type [18]. Tissues are usually sliced to a thickness of 5−20 μm, thus the majority of the cells in the slice are cut open, exposing their intracellular contents for analysis [18]. Then the tissue sections are thaw-mounted on conductive indium tin oxide glass slides. Most tissue sections used in this thesis were of 10 μm or 12 μm thickness.

4.3. On-tissue chemical derivatization

Some metabolites suffer from indetectability in MALDI due to their low ionization efficiency combined with interferences in the same mass range with matrix-related signals in MALDI, such as amino acids with a molecular weight <250 Da. One way to overcome this is the use of on-tissue chemical derivatization, which has already been used to improve the detection sensitivity of poorly ionizable metabolites in MALDI mass spectrometry imaging [76]. On-tissue chemical derivatization chemically reacts with specific functional groups including amine, phenolic hydroxyl, carbonyl, carboxylic acid, thiol, and double bonds [76, 77], resulting in mass shifting of the derivatized product out of the matrix's mass range, thus improving the ionization efficiency and sensitivity for targeted metabolites and minimizing their ion suppression in MALDI-MSI [76, 77]. Generally, an automatic sprayer such as from HTX or SunChrom is used to apply derivatization reagents homogeneously onto tissue sections followed by an incubation in a humid atmosphere at room temperature or slightly higher temperature for several hours [77]. For example, p-N,N,N-trimethylammonioanilyl N'-hydroxysuccinimidyl carbamate iodide (TAHS), is a derivatization reagent that briefly reacts with the amino group, leading to form derivatives of amino acids which are positively charged in the trimethylanilynium moiety (Figure 1.8) [78], resulting in a mass shift of 177.1022 Da. This leads to a significant improvement in ionization efficiency for multiple amino acids (Figure 1.9) [79, 80]. The combination of on-tissue TAHS derivatization and MALDI-MSI has been successfully applied to mouse brain [79], human cancer xenografts

[78, 80] and mouse liver [81]. In addition to TAHS, trans-cinnamaldehyde, 4-hydroxy-3-methoxycinnamaldehyde, 2,4-diphenyl-pyranylium tetrafluoroborate, 2-nitrobenzaldehyde and 2-fluoro-1-methyl pyridinium reagents can also react with amine groups and have been applied in MALDI-MSI on different tissues [77]. Moreover, 2-fluoro-1-methylpyridinium p-toluene sulfonate for derivatization of the phenolic hydroxyl group. 4-(N-methyl) pyridinium boronic acid was applied for the derivatization of catecholamines. Girard's reagent T can react with the ketone group and forms hydrazine derivatives [77]. 2-picolylamine and N,N-dimethylpiperazine iodide can form stable derivatization products with a carboxylic acid [77]. (E)-2-cyano-N-(2-(2,5-dioxo-2,5-dihydro-1H-pyrrol-1-yl)ethyl)-3-(4-hydroxyphenyl)-acrylamide is a thiol derivatization reagent [77]. Benzaldehyde and benzophenone can be applied for distinguishing and imaging of double bonds in lipids [77]. In this thesis, TAHS derivatization was used for improving the ionization efficiency of targeted amino acids (Phenylalanine and Tyrosine) in mouse tumor samples (**chapter 5**), considering that TAHS showed better derivatization results for both Phenylalanine and Tyrosine based on a comparative study of different derivatization methods published by Esteve *et al.* [79].
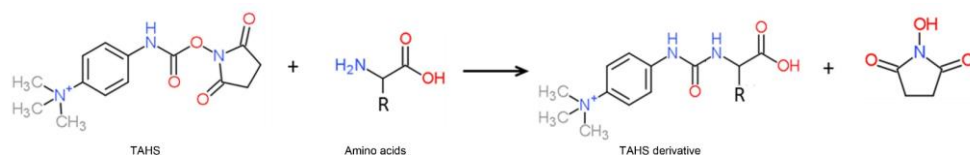
Figure 1.8. The p-N,N,N-trimethylammonioanilyl N'-hydroxysuccinimidyl carbamate iodide (TAHS), is a derivatization reagent to react with the amino group, leading to form derivatives of amino acids which are positively charged in the trimethylanilynium moiety and which results in a mass shift of 177.1022 Da.
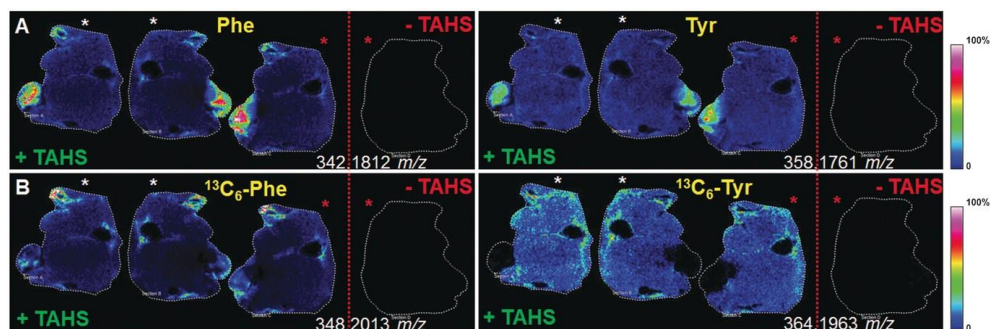
Figure 1.9. The representative MALDI-MSI images of L-phenylalanine(Phe, A panel, left) and L-tyrosine (Tyr, A panel, right) as well as 13C6 isotopically labeled 13C6-Phe (B panel, left) and 13C6-Tyr (B panel, right) with TAHS derivatization (+TAHS) and without (−TAHS) derivatization in mice liver sections. The figure has been reproduced from [81].

4.4. Matrix application

Matrix must be applied homogeneously on the surface of the tissue prior to MALDI-MSI analysis. Automatic spray-coating methods (solvent-based) and sublimation (solvent-free) are often used due to easy handling and the high level of reproducibility [77]. Most automatic

sprayer systems apply a thin matrix layer onto the tissue sections by nebulizing the matrix solution using a spray nozzle that, at a certain height, continuously moves over the tissue slide combined with a fixed drying time between each layer [82]. Several instrumental parameters can be adjusted manually to improve the matrix deposition quality. Such an example is the TM-sprayer (HTX Technologies), which allows adjusting the spray nozzle velocity and temperature, the nitrogen gas pressure, the track spacing, the solvent flow rate, the spray area, the number of layers and the drying time between layers. In contrast to automated matrix sprayers, matrix sublimation is a dry matrix application method. Both, the powdered matrix in a heating plate as well as the tissue slide on the sample holder, are placed in a pressure-controlled chamber. The solid matrix is heated and sublimated to a gaseous state and then condenses on the targeted slide which is locally cooled [83]. Sublimation results in an enhanced matrix purity as well as a much smaller matrix crystal sizes (<1 μm) [70], thus it is widely used for higher spatial resolution MSI [70]. The amount of matrix, the condenser temperature, the pressure, and the sublimation time are the main adjustable parameters for the commercially available Sublimator (HTX Technologies) [83]. Even though sublimation offers several advantages, it can suffer from a lower extraction efficiency compared to solvent assisted spray methods [83-85]. In this thesis, two automatic sprayer systems including the TM-sprayer (HTX Technologies, Chapel Hill, NC, USA) (**chapters 2**, **4** and **5**) and the Suncollect (SunChrom GmbH, Friedrichsdorf, Germany) (**chapter 3**) were used for matrix application.

Importantly, the choice of matrix depends on the mass range analyzed and the target analytes. For instance, lipids in tissues are easily ionized due to their charged polar head groups [86], e.g., phosphatidylcholine (PC) and sphingomyelin (SM) lipids are easily detected in positive ionization mode because they have the positively charged quaternary amine groups, while phosphatidic acids (PA), phosphatidylglycerols (PG), and phosphatidylinositols (PI) and phosphatidylserines (PS) are usually analyzed in negative ionization mode due to the presence of the phosphodiester moiety. Phosphatidylethanolamines (PE) can be detected in both ionization modes [5, 87]. It is therefore recommendable to use both, negative and positive, polarities in a MSI study to cover more lipid classes. The dual polarity matrix norharmane is a commonly used MALDI-MSI matrix to detect lipids in both ionization modes [88], which has been widely applied to different tissues [89-91]. In this thesis, norharmane was applied on mouse aortic tissues (**chapter 2**) and rat abdominal fascia tissues (**chapter 4**) using TM-Sprayer for the detection of lipids in negative and positive ionization modes by MALDI-MSI.

On the other hand, α-cyano-4-hydroxycinnamic acid (CHCA) and 2,5-dihydroxybenzoic acid (DHB) are very popular matrixes for the detection of metabolites in the positive ionization mode using MALDI-MSI [82]. Also, 9-aminoacridine (9-AA) [92] is one of the frequently used matrices suitable for targeting low-molecule-weight compounds (m/z <500) such as adenosine monophosphate (AMP), adenosine diphosphate (ADP), adenosine triphosphate (ATP), uridine diphosphate (UDP), fructose-1,6-bisphosphate in negative ionization mode

by MALDI-MSI. Consequently, a number of studies employed 9-AA as MALDI-MSI matrix for metabolites imaging in human Hela cells [93], rat brain tissues [94], mouse heart tissue [95], rabbit aortic tissue [96], human skin tissue sections [97], human osteoarthritis cartilage [98] and many other tissues. It has also been employed for the *in situ* analysis of metabolites in formalin-fixed and paraffin-embedded (FFPE) tissue specimens [65]. For instance, Aichler *et al*. recently performed MALDI-MSI on Langerhans islets tissues from both mouse and human to characterize metabolic interaction networks of functional pathways. They found classes of metabolites such as stearoylcarnitine, acetylcarnitine and N-acyl taurines involved in insulin synthesis and secretion, which are disrupted in diabetes [99]. Furthermore, several novel MALDI matrices, e.g. N-(1-naphthyl) ethylenediamine dihydrochloride (NEDC) [100], 2-mercaptobenzothiazole (MBT) [101] and 2,5-diaminonapthalene (DAN) [102] have also been applied for the *in situ* MALDI MSI of metabolites. In this thesis, 9-AA was applied on mouse aorta (**chapter 3**) samples using the Suncollect spraying system for the analysis of metabolites in negative ionization mode. DHB (**chapter 5**) was applied on mouse tumor samples using the TM-sprayer for detecting derivatized amino acids in positive ionization mode.

4.5. Three dimensional MALDI-MSI

Amongst all available mass spectrometry imaging systems, MALDI-TOF is the most widely used, owing to its high speed, high sensitivity, and wide mass range. This technique has already been extended to the third dimension, which is called three-dimensional MALDI mass spectrometry imaging (3D-MALDI-MSI). In order to generate a 3D-MALDI-MSI image, a series of consecutive sections from a tissue sample are analyzed to obtain molecular information in the depth dimension. Volumetric 3D-MSI images can be reconstructed based on a stack of 2D MSI images, which allows investigating molecular profiles in all three dimensions and therefore deepens the understanding of complex contextual information about the biological sample. 3D-MSI has already applied to various tumor samples, brain, aorta and other organs [103]. In **chapter 2** of this thesis, 3D-MALDI-MSI of lipids was performed in an atherosclerotic mouse aorta. One important aspect in the reconstruction of 3D-MSI images is the correct alignment of the stack of serial 2D images to a volume true to the original biological sample. The alignment is done using image registration techniques from the field of image processing.

4.6. Co-registration with microscopic images after MALDI-MSI

It is indispensable to contextualize these molecular distribution maps with the underlying histological information for a correct interpretation of MSI data. The combination of MSI with histological and morphological features in the tissue sample enables not only visualizing molecular distributions within the histopathological context, but also to reveal molecular signatures characteristic for regions of interest or specific cell types defined by histological annotation, which is critical for understanding the biological complexity of diseased tissues or cells [30].

The tissue is typically not significantly ablated during the laser ionization process [30] while the matrix is. Therefore, after MALDI-MSI measurement, the very same tissue section can be stained with histological dyes, digitally scanned, and its histological image can then be co-registered to the MSI data [30]. The most common histological staining is hematoxylin and eosin (H&E), which has also been used throughout all chapters of my thesis.

However, due to the complex molecular and cellular nature of diseases, the combination of MSI with a single histological image is usually not sufficient, and hence additional complementary molecular and histological information is needed [104]. For instance, in my work on atherosclerosis (**chapter 3**), four different stainings were conducted to histologically and molecularly characterize the dissected atherosclerotic aortic sections (Figure 3.1) and to correlate them with the MSI data: hematoxylin & eosin staining (gives general overview of the cellular composition and structure of the tissue), Oil red O (shows accumulations of neutral lipids), CD68 immunohistochemistry (visualizes macrophages) and red alizarin (indicates calcification).

5. MALDI-MSI applications on metabolomics in diseases

In general, untargeted and targeted analyses are the two distinct strategies for MS-based metabolomics studies [4]. Non-targeted metabolomics typically aims to comprehensively detect as many metabolites or putative metabolites as possible (>1000) in a sample [4], thus it is well suited for biomarker discovery and hypothesis generation [4]. Meanwhile, targeted metabolomics attempts to detect and quantify a predefined list of chemically characterized and biochemically annotated metabolites [4] in order to investigate specific metabolic pathways such as tricarboxylic acid cycle or validate biomarkers identified from an untargeted study [105]. Since MALDI-MSI offers the unique capability of simultaneously imaging a large number of metabolites directly in tissues, it is well suited for untargeted metabolomics analyses. It can therefore not only be a valuable source of potential new biomarkers but also for yielding important insights into molecular mechanisms of diseases beyond tissue morphological observations [106].

5.1 The relevance of MALDI-MSI metabolomics in disease research

Conventional untargeted MALDI-MSI metabolomics

Non-targeted MALDI-MSI metabolomics has been successfully applied in many different diseases for the *in situ* visualization of metabolites in both preclinical animal models and human samples, particularly of lipids. Lipids are one fundamental building block of cells and account for approximately half of the mass of cell membranes [107], thus they are ubiquitous and abundant across all biological tissues [108]. In addition, lipids play significant roles in a variety of cellular processes owing to their great chemical diversity and physical properties [109]. Lipids have been strongly implicated in various diseases [110]. In the field of MALDI-MSI, this technique has greatly contributed to study the dysfunction of lipids metabolism in many diseases, including cancer [89, 111-116], cardiovascular disease [96, 117-123], obesity

[124, 125], diabetes [99, 126], retinal diseases [127-130], nonalcoholic fatty liver disease [131-133], cholestatic parenchyma [134], osteoarthritis [98, 135], rheumatic diseases [136], kidney diseases [137-141], chronic alcohol use disorders [142], congenital and genetic diseases [143-145], Alzheimer's disease [146-157], Parkinson's disease [158], Huntington's disease [159, 160], Myelin Disease [161], ischemic strokes [162], skin wound healing [163, 164] as well as viral diseases [165-167]. For instance, using MALDI-MSI, Kaya *et al.* revealed alterations of infarct-associated sphingolipids, glycerophospholipids, lysophospholipids, cardiolipins and acylcarnitines in a mouse model of myocardial infarction [117]. Paine *et al.* examined lipids associated with medulloblastoma metastasis, including phosphatidic acids, phosphatidylethanolamines, phosphatidylserines, and phosphoinositides by 3D-MALDI-MSI [89].

Additionally, MALDI-MSI metabolomics is capable of mapping other metabolites on tissue such as amino acids [79], energy-related molecules such as adenosine monophosphate (AMP), adenosine diphosphate (ADP) and adenosine triphosphate (ATP) [168], neurotransmitters [169], carbohydrates, organic acids, vitamins [170], glucose and related metabolites [171], metabolites involved in metabolic networks [172] such as glycolysis, tricarboxylic acid cycle, fatty acids metabolism [173] and kynurenine pathway [174], as well as metal ions [175]. For example, Aichler *et al.* applied MALDI-MSI on Langerhans islets to determine the metabolic characteristics of these islets during type-2 diabetes progression. They found that accumulation of N-acyl taurines and acetylcarnitine is linked with insulin synthesis and secretion [99]. Likewise, Du *et al.* showed that the energy metabolism plays a central role in the functional recovery during cerebral ischemia-reperfusion [176]. Esteve *et al.* found several metabolites to be involved in the purine metabolic pathway in the context of Alzheimer's disease such as uric acid [177]. Similarly, Lou *et al.* identified inositol cyclic phosphate and carnitine were correlated with overall survival and metastasis-free survival in high grade sarcomas patients, respectively [116]. Likewise, Andersen and coworkers revealed several differential metabolites such as nucleotides (AMP, ADP and ATP), citrate and zinc among others in different human prostate tissue types (cancer, non-cancer epithelium, and stroma) [175]. Interestingly, a recent study by Murakami *et al.* identified distinct tissue metabolomic profiles of pheochromocytoma and paraganglioma in relation to tumor genotypes [174]. Of note, there are many other MALDI-MSI metabolomics studies in different pathologies including tumor [178-183], neurodegenerative diseases [179, 184], status epilepticus [185], osteoarthritis [186], ischemic strokes [187] among others, as well as normal tissues such as kidney [169] and bovine lens [171].

In **chapters 2** and **3** of this thesis, I applied non-targeted metabolomics on atherosclerosis in mice. In a similar manner, I studied fascia healing in a rat model in **chapter 4**.

Targeted MALDI-MSI metabolomics

Most of targeted MALDI-MSI metabolomics studies focus on the local detection of drugs, toxicants and their metabolites in different tissues to investigate their

pharmacological/toxicological effects [188]. These exogenous compounds include acetaminophen [189], cyclic peptide melanotan II [190], scutellarin [191], thymoquinone [192], sulfamethoxazole [193], triamcinolone acetonide [194], sunitinib (anti-angiogenic drug) [195], tetrandrine [196], polyphenols [197], citalopram [198], brimonidine [199], amodiaquine [200], methamphetamine [201], platinum-based drugs (cisplatin, carboplatin, and oxaliplatin) [202], tuberculosis [203], oligonucleotide therapeutics [204, 205], irinotecan [206], amitriptyline [207], retigabine [208], dufulin [209], nicotine and mannitol [210], cocaine, benzoylecgonine, and cocaethylene [211], irinotecan [206], fosdevirine [212], l-DOPA [213], as well as seasonal trivalent influenza vaccine [214] among others.

Moreover, targeted MALDI-MSI has also greatly benefited from on-tissue derivatization strategies targeting specific functional-group-containing endogenous metabolites such as sulfur-containing metabolites [215], carboxyl-containing metabolites [216], amine metabolites (*e.g.* amino acids and neurotransmitters) [217], vitamin D metabolites [218], as recently reviewed by Harkin *et al.* [219].

Of note, conventional MSI typically captures a static snapshot of a highly dynamic metabolic system at a single time-point within a given tissue sample [81], hence suffering from sampling bias and the limitation of tracing dynamic metabolic changes over time. In this context, stable isotopic labeling, offers the opportunity to study the dynamics of metabolic fluxes [220], since the incorporation of isotopes (commonly ^{13}C, ^{2}H, and ^{15}N) into target metabolites, amino acids, small peptides or water [221] produces shifted mass signals, including the labeled precursor and the products of its metabolic conversion, which can be detected by MS-based technologies [220]. Combining targeted MSI, stable isotope labeling with the use of animal models can therefore reveal spatially resolved dynamics of targeted molecule synthesis and turn over occurring in tissue samples [81].

To date, several targeted studies have coupled isotope labeling with the MALDI imaging. For example, Louie *et al*. used MALDI-MSI to map the heterogeneous spatial distributions of D_2O-labeled lipids in intratumor subpopulations [222]. Castro-Perez *et al.* investigated the incorporation of an isotopically labeled 2,2,3,4,4,6-d6-cholesterol into atherosclerotic plaques with the same ionization approach [223]. Ellis *et al*. used MALDI-MSI of both methyl-D_9 choline and universally ^{13}C-labeled dipalmitoyl PC administered to mice to visualize lung and surfactant lipid metabolism [224]. Yoshinaga *et al*. revealed that the administered ^{2}H (D) labeled arachidonic acid and docosahexaenoic acid first accumulated in the hippocampus and cerebellar cortex in the brain [225]. Kihara *et al.* analyzed the distribution of ^{57}Fe-heme in the mice spleen using MALDI FTICR-MSI [226]. And finally, Arts *et al.* revealed the localized hepatocellular synthesis of L-phenylalanine in mice with ^{13}C [81].

To conclude, isotope labeling together with MALDI-MSI harbors great potential for the investigation of the spatial dynamics of metabolic processes in many diseases, especially in

cancer. Therefore, in **chapter 5** of this thesis, I studied the kinetics of ^{13}C labeled L-phenylalanine and its derivative L-tyrosine in lung tumor xenografts over time [80].

However, first I applied untargeted MALDI-MSI to tissues from animal models to better understand local metabolic processes in atherosclerosis (**chapters 2** and **3**) and fascia healing (**chapter 4**).

5.2 Atherosclerosis

Atherogenesis and atherosclerotic mouse models

Atherosclerosis is the leading cause of morbidities and mortalities worldwide. It is a chronic lipid-driven inflammatory disease characterized by atherosclerotic plaques formation in the arterial wall [47]. Atherosclerotic plaque formation and progression (Figure 1.10) has been greatly clarified by studies in experimental animals [227]. In general, a normal arterial wall comprises three morphologically distinct layers: the tunica intima (the innermost, facing the lumen of the vessel), the tunica media (the middle layer), and the tunica adventitia (the outermost layer) [227]. The intima is made up of a monolayer of endothelial cells, which acts as a selective permeability barrier between the circulating blood and the other vessel layers [228]. The media layer consists predominantly of multiple longitudinally oriented vascular smooth muscle cells (SMCs) [227]. The adventitia is composed of dispersed fibroblasts, adipocytes, inflammatory cells, SMCs, stem and progenitor cells, as well as perivascular nerves [229]. Each layer presents specific characteristics and essential functions to maintain vascular integrity and homeostasis, as well as to regulate the vascular responses to external stimuli [230].

Endothelial dysfunction plays an important role for the pathogenesis of atherosclerosis (Figure 1.10) [231]. The dysfunctional endothelium results in the accumulation and aggregation of circulating lipoprotein particles and monocytes in the intima [227], where the monocytes subsequently differentiate into macrophages and take up the lipoproteins to convert into foam cells [231]. Form cells make up the characteristic fatty streaks observed in the early stages of atherosclerosis [232]. Those macrophageous foam cells die over time and contribute their lipid-laden contents to form a necrotic core [233]. SMCs from the media layer can also subsequently migrate into the intima, where they produce extracellular matrix components [234] and secrete cytokines to further enhance the accumulation of inflammatory cells in the intima [235], and thereby giving rise to a progressively larger and more complex lesion with a fibrous cap. Those lesions can continue to grow by attracting new monocytes from the blood, which is accompanied by cell proliferation, extracellular matrix production and the accumulation of extracellular lipid [227]. Destabilizing factors such as cell deaths or vascular calcification can result in rupture of the fibrous cap [236], thereby exposing the lipid content to the bloodstream, which can cause thrombus formation, which can result in an acute myocardial infarction or a stroke [227].
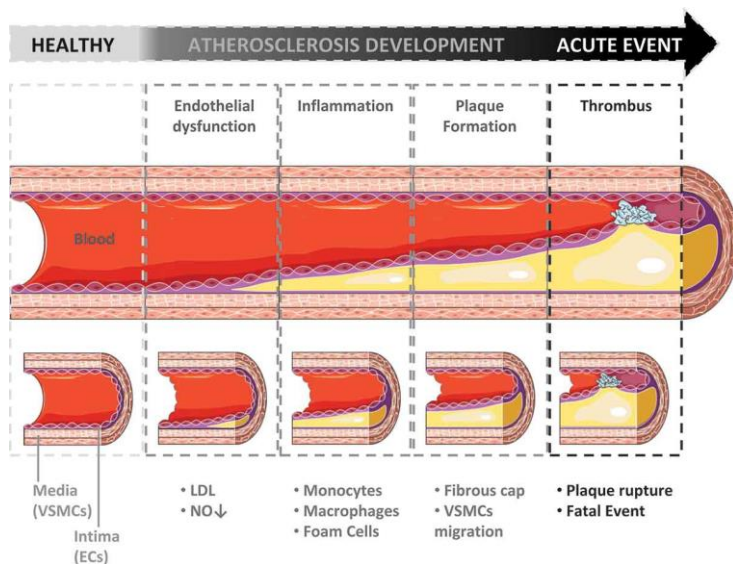
Figure 1.10. Schematic diagram of atherosclerosis progression from a healthy artery (left) to early-and late-stage atheroma (middle and right, respectively). Atheroma formation starts with endothelial dysfunction, followed by accumulation and aggregation of low density lipoprotein (LDL) particles in the intima layer, followed by monocytes proliferation and differentiation into macrophages. Macrophages take up the lipoproteins and form foam cells, resulting in characteristic fatty streaks observed in the early stage of atherosclerosis. Fatty steaks can subsequently accumulate vascular smooth muscle cells (VSMCs) from the media layer. Following the secretion of fibrous elements by the SMCs, together with cell proliferation, extracellular matrix production and the accumulation of extracellular lipids, fibrous atheroma with fibrous cap may continue growing in size and become increasingly complex. Destabilizing factors such as cell death or calcification may result in plaque rupture and release of its contents to the bloodstream, which can lead to acute events such as myocardial infarction or stroke. This figure has been reproduced from [237].

Animal models of atherosclerosis are valuable tools to investigate its etiology [238] and the molecular mechanisms underlying pathogenesis and progression of atherosclerosis [239], as well as to test pharmacological treatments and validate diagnostic imaging techniques [238]. In general, animal models of atherosclerosis are based either on a western type diet enriched in high fat and/or high cholesterol [240], or the introduction of genetic modifications involved in cholesterol synthesis and uptake [239, 240], or both. In atherosclerosis research, mice and rabbits are the predominantly used animals, followed by rats, swine, primates and other animal models [239]. Among them, mice are the leading species to study experimental atherosclerosis due to its friendly cost, small size, prompt reproduction and simplicity of genetic manipulation, together with its feasibility to develop and atherosclerotic symptoms in a reasonable time scale [239]. Both low-density lipoprotein receptor deficient ($ldlr^{-/-}$) mice and apolipoprotein E deficient ($apoe^{-/-}$) mice are the two most widely used genetically modified animal models for atherosclerosis [241]. These two mouse models have been comprehensively reviewed by Emini Veseli *et al.* [239] as well as Getz *et al.* [241] (Figure 1.11). In **chapter 2**, I have used MALDI-MSI to find commonalities and differences in the lipidic composition between the atheromas of both mouse models. More precisely, $ldlr^{-/-}$

mice in **chapter 2** were fed a high fat and high cholesterol diet (HFD) for 16 weeks and $apoe^{-/-}$ mice a normal-diet, both of which resulted in advanced atherosclerotic lesions. In contrast in **chapter 3**, $ldlr^{-/-}$ mice were fed an 8 weeks HFD leading to an earlier stage of atherosclerosis as compared to the mice utilized in **chapter 2**. Moreover, I mainly focused on the aortic atherosclerotic lesion for all mice considering the aortic root are the predominant sites for atherosclerosis development in rodents [239].

Figure 1.11. The overview of the two most widely used genetically modified animal models for atherosclerosis, including low-density lipoprotein receptor deficient ($ldlr^{-/-}$) mice and apolipoprotein E deficient ($apoe^{-/-}$) mice. The $apoe^{-/-}$ mouse model develops advanced atherosclerosis on normal diet (ND), while $ldlr^{-/-}$ mice require western style diet (WD). As consequence, $ldlr^{-/-}$ mice show a more human-like lipid profile as compared to the $apoe^{-/-}$ mice. This figure has been reproduced from [239].

MALDI-MSI metabolomics of atherosclerosis

Atherogenesis involves the interaction of many different molecules in a complex network, which is still not fully unraveled and it is known that lipids are important players in plaque formation and progression. Lipid composition, localization, and alteration along the arterial wall are therefore considered to play a crucial role in the progression of atherosclerosis and the stability of the atheroma [242]. However, lipids constitute an extremely heterogeneous and abundant molecular class, which –combined with the spatial complexity of an atheroma– makes their *in situ* investigation extremely difficult.

In this context, MALDI-MSI has already demonstrated its unique capability of directly accessing a tissue's molecular content in cardiovascular diseases [243]. Specifically in atherosclerotic research however, MALDI-MSI remains an underexplored technique with only a few studies, which have so far have focused on the optimization of the experimental conditions [244] and data processing [122, 245]. For example, Martin-Lorenzo *et al*. applied MALDI-MSI on atherosclerotic rabbits, which showed increased expression of fatty acids

and lysolipids in the intima, and the accumulation of phosphatidylinositol, phosphatidylglycerol and sphingomyelin are in line with an endothelial dysfunction and a triggered inflammatory response [96]. In the same study, triglycerides, phosphatidic acid, sphingomyelin and ceramide phosphoethanolamines were identified specifically located in calcified regions [96]. Castro-Perez *et al*. found specific lysophosphatidylcholines as well as free cholesterol and cholesteryl esters that contribute to atheroma formation using MALDI-MSI on aortic tissue of *apoe*$^{-/-}$ mice [123]. Moreover, they showed distinguished spatial accumulation of non-esterified and esterified versions of (2,2,3,4,4,6-d(6))-cholesterol within aortic plaque regions [123]. Interestingly, Lohofer *et al*. recently applied MALDI-MSI to visualize the localization and measure the concentration of the magnetic resonance imaging probe Gadofluorine P in the *ldlr*$^{-/-}$ mice's aortic plaques which thus adds novel information on the specificity and sensitivity of the marker for magnetic resonance imaging of atherosclerosis [246].

In addition to animal models, MALDI-MSI has also been applied to human samples. For example, Moerman *et al.* applied MALDI-MSI on human carotid atherosclerotic plaques. They found the abundances of sphingomyelin and oxidized cholesteryl ester species were elevated specifically in necrotic intima areas, whereas diacylglycerols and triacylglycerols were spatially correlated to areas containing the coagulation protein fibrin [247]. Likewise, Greco and coworkers investigated lipids on human carotid atherosclerotic plaques by MALDI-MSI. They found macrophage-rich regions from symptomatic lesions to be enriched in sphingomyelins, and intimal SMCs of symptomatic plaques to be enriched in cholesterol and cholesteryl esters [248]. All these studies confirm that MALDI-MSI is a promising tool for the investigation of histologically heterogeneous atherosclerotic tissues. Nevertheless, these studies have so far overlooked the volumetric complexity of atheromas. To address this issue, I used three-dimensional (3D) MALDI-MSI to study the lipids distributions in aortic plaque in a volumetric manner.

While lipids certainly are at the core of atherosclerosis, the triggered inflammatory response during atherosclerosis progression also indicates an imbalance in other low-molecule-weight metabolites. However, there has not been any MSI-based study on both lipids and other metabolites so far. Moreover, novel molecular targets and metabolic marker panels for this silent pathology are strongly needed. This is the reason why in **chapter 3** of this thesis, I applied untargeted metabolomics to explore spatially resolved metabolic alterations while locating them within the aortic structure in high fat, high cholesterol diet *ldlr*$^{-/-}$ mice (n=11) aortic tissues compared to normal diet *ldlr*$^{-/-}$ mice (n=11) using MALDI-FTICR-MSI.

5.3 Wound healing

The stages of wound healing

Not unlike atherosclerosis, wound healing is also a highly complex and dynamic process which involves the interaction and coordination of a myriad of different cells and molecules [249]. Wounds can be generally classified as acute (a few weeks) or chronic (several months

or years) depending on their time frame of healing [249]. Acute wounds can result from traumatic tissue loss, a surgical operation or even from an insect's bite [249]. Acute wound healing undergoes a well-organized process, which is classically divided into four temporarily and spatially overlapping phases: hemostasis, inflammation, proliferation, and remodeling [250] (Figure 1.12). Hemostasis takes place as soon as a wound occurs, where first platelets are activated and which is then followed by the recruitment of immune cells, the stimulation of resident skin cells such as fibroblasts and keratinocytes, as well as a series of enzymatic activities, contributing to the formation of a fibrin clot to seal the injury site and prevent further bleeding [250]. The inflammation stage of healing is characterized by infiltration of resident immune cells (*e.g.* neutrophils, mast cells, T cells and monocytes/macrophages) to elicit the inflammatory responses [251]. As the inflammation diminishes, the wound healing process is dominated by the proliferation phase (growth of new tissue), where angiogenesis, matrix deposition, formation of granulation tissue, and revascularization/angiogenesis occur [252]. During the proliferation stage, keratinocytes are extensively activated and migrated across the wound edge to resurface the wound with a new epithelium layer [253]. Finally, the deposited matrix undergoes controlled remodeling by fibroblasts, and followed by myofibroblasts contributing to overall wound contractions [254]. Later, the resident cells go through apoptosis upon completion of the tissue healing [250].

Currently, several models have been used for investigating wound healing, including different animals (e.g. rodents, rabbits, and pigs) as well as non-animal models such as *in silico* computational models, *in vitro* models (e.g. mono-layered cultures, co-cultures, and skin explants) [255]. The reader can refer to the systematic review by Sami *et al.* [255]. It has been found that a repertoire of lipids are critical players during the different stages of wound healing, including glycerophospholipids (e.g. lysophospholipids and fatty acids) and sphingolipids (e.g. sphingomyelin and ceramide), as recently reviewed by Pils and coworkers [256].

Furthermore, unlike acute wounds, which heal through the routine four healing stages in an orderly and timely manner, a chronic wound comes along with other pathologic factors such as metabolic diseases, peripheral vascular disease, medications, radiation therapy, or external factors (*e.g.* sustained pressure, temperature, depression) [257]. All these factors cause a healing process deviated from the previously described normal stages of healing and ultimately resulting in the non-healing of wounds [257].

In **chapter 4** of this thesis, I focused on the role of localized lipids on acute wound healing.
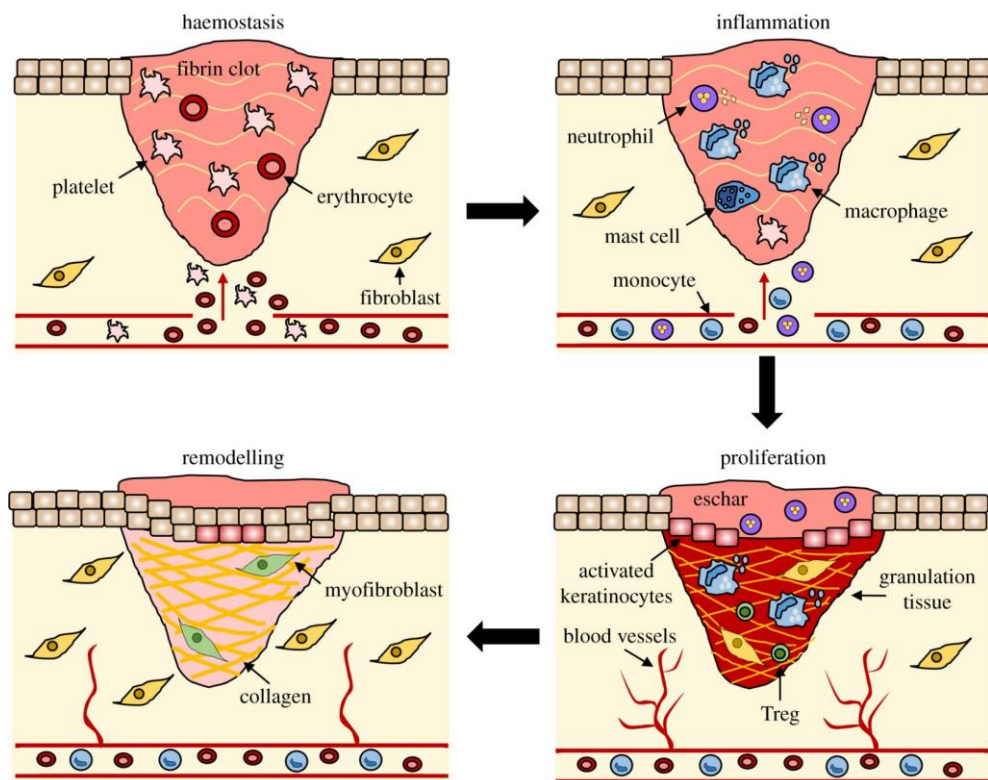
Figure 1.12. The major phases of acute wound healing: hemostasis, inflammation, proliferation, and remodeling (in chronological order). Hemostasis takes place as soon as a wound arises: platelets are activated and followed by the recruitment of immune cells, the stimulation of resident skin cells such as fibroblasts, contributing to the formation of a fibrin clot. The inflammation stage is characterized by the infiltration of resident immune cells (e.g. neutrophils, mast cells, T cells and monocytes/macrophages) to elicit the inflammatory responses. With the diminishing of inflammation, angiogenesis, matrix deposition, formation of granulation tissue, and revascularization/angiogenesis occur in proliferation phase. Finally, the remodeling occurs upon completion of the wound healing. The figure has been reproduced from [250].

MALDI-MSI metabolomics on wound healing

The cellular and molecular mechanisms underpinning acute wound healing remain poorly understood, especially for fascial wound healing owing to most of the wound healing studies having focused on skin wounds [258], which is also true for MALDI-MSI studies [259]. Indeed, MALDI-MSI has successfully applied in a few wound healing metabolomics studies with a specific focus on skin. For instance, Lewis and coworkers examined lipids directly involved in the skin wound healing process using MALDI-MSI in a wounded living skin equivalent model [260]. Likewise, Komprda *et al.* employed MALDI-MSI for evaluating the effects of dietary oils containing polyunsaturated fatty acids on cutaneous wound healing in Wistar rats [261]. Even though acute wounds undergo similar healing process regardless of

skin or fascia, the differences between fascial healing and skin healing have been continuously recognized [262]. More studies with different techniques are hence needed to reveal the specific mechanism of fascial incisions healing. This is the reason why in **chapter 4** of this thesis, I studied lipids alterations exclusively involved in the fascia healing process using MALDI-MSI [263].

5.4 Cancer

Cancer metabolism

Cancer is a group of diseases characterized by the uncontrolled growth and proliferation of any of the different types of cells in the body, and thus there are over 100 distinct known types of cancer [264]. These demonstrate considerably different metabolic features [265], as well as clinical behaviors and responses to treatment [266]. The detailed cancer pathogenesis is beyond the scope of this chapter and the reader is referred to the other review papers [264, 267]. However, metabolic alterations have been well recognized as a hallmark of cancer [13]. The most extensively investigated metabolic change in cancer is the deregulated glucose metabolism, which refers to the Warburg effect [268]. The normal cells are primarily relying on mitochondrial oxidative phosphorylation to obtain the energy required for cellular activities [269]. In contrast, most tumor cells preferentially utilize aerobic glycolysis as a means of energy rather than the more efficient mitochondrial oxidative phosphorylation [268], such that 2-deoxy-2-[fluorine-18]fluoro-D-glucose (^{18}F-FDG) has been the most commonly used tracer for PET oncologic imaging in the clinic [270]. Moreover, a great number of recent studies evidenced that glutamine metabolism also plays a crucial role in cancer [271], which is involved in regulating energy formation and macromolecular synthesis, as well as maintaining redox homeostasis and cellular signaling in cancer cells [272]. Consequently, ^{18}F-labeled glutamine has also progressively applied in both preclinical and early clinical tumor PET imaging studies [273]. Furthermore, with the development and application of new technologies over the past decades, heterogeneity and plasticity in tumors have been greatly unraveled [274], but also novel metabolic targets and pathways involved in tumor initiation and progression are evolving rapidly [275]. For instance, alteration of reactive oxygen species [276] and acid/base homoeostasis [277] in cancer cells has been well recognized in tumor metabolism.

Moreover, modified levels of oxygen and nutrients of the tumor microenvironment (TME, Figure 1.13) can cause altered metabolic phenotypes of cancer cells [278]. Interestingly, it has also been suggested that metabolites in the TME not only offer energy substrates, but also act as key players in cell-to-cell communication and further affect cancer cellular behavior [279]. In addition, cancer cells and other cells including fibroblasts and immune cells in the TME can exchange metabolites [280]. These metabolites can regulate each other's functions [280]. Finally, a great number of metabolomics based studies have investigated the altered metabolism of lipids and other metabolites such as amino acids participating in tumor initiation and progression [281].
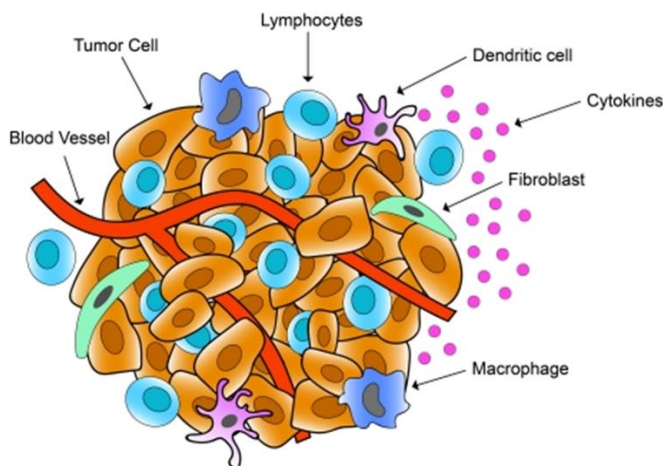
Figure 1.13. Simplified schematic representation of the tumor microenvironment (TME). TME is created by the tumor and is comprised of proliferating tumor cells, the tumor stroma, blood vessels, immune cells (e.g. lymphocytes, dendritic cells, macrophages, rare natural killer cells), fibroblasts, signaling molecules and the extracellular matrix [282]. The figure has been reproduced from *https://www.precisiononcology.ie*.

MALDI-MSI metabolomics in cancer research

Given the importance to spatially unravel the TME from the tumor for tissue metabolomics, MALDI-MSI has presented itself as an invaluable tool to not only spatially differentiate cancer metabolic heterogeneity, but also to facilitate cancer biomarker discovery with diagnostic and prognostic potential [281].

MALDI-MSI metabolomics studies have been extensively performed in cancer research, where untargeted studies focused on the investigation of endogenous metabolites [183] and untargeted studies mostly on the detection of anticancer drugs [283]. Regarding the first, MALDI-MSI has been applied to brain tumor [60, 284-287], breast tumor [172, 181, 286, 288, 289], colonic tumor [78], colorectal carcinoma [100, 290-293], head and neck tumor [294, 295], gastrointestinal stromal tumor [296], urachal tumor [297], oral cancer [298, 299], gastric cancer [73, 300], colon cancer liver metastasis [301], lung cancer [302-308], lymphoma [309], thyroid tumor [310], renal cancer [111, 311-314], bladder cancer [315], ovarian carcinoma [316], prostatic cancer [175, 317], sarcoma [318], adrenocortical carcinoma [180], pheochromocytoma and paraganglioma [174], as well as different multicellular tumor spheroids [182, 319, 320]. For instance, MALDI-MSI has been performed to identify tumor-specific metabolites [294], to discriminate metabolites profiles between cancerous and normal tissues [181, 298], as well as to differentiate between subtle variations but highly similar tumors [291]. Likewise, MALDI-MSI has also been employed to identify metabolites that correlate with cancer grading and prognosis [318]. Additionally, MALDI-MSI together with large-scale tissue microarrays has been increasingly evidenced as powerful biomarker discovery tool [321, 322].

MALDI-MSI has also been widely used to investigate anticancer drugs, including irinotecan [206, 323], paclitaxel [324], Platinum-based metallodrugs (cisplatin and oxaliplatin) [202, 325], afatinib [326], sorafenib [326], erlotinib [326, 327], sunitinib [328, 329], and nanoparticle-formulated drugs [330] amongst others.

In addition, MALDI-MSI has also been applied to image an exogenous hypoxia marker pimonidazole as well as other associated metabolites in breast tumor [331] and to image the anticancer drugs in spheroids or organoids, as recently reviewed by Wang and coworker [332].

However, as mentioned previously, MALDI-MSI remains poorly applied in understanding metabolite dynamics and kinetics. This is the reason why in **chapter 5** of this thesis I explored the use of ^{13}C-labeled L-phenylalanine to understand amino acid anabolic processes in the context of the cancer's tissue morphology MALDI-FTICR-MSI [80].

6. Thesis outline

To summarize, the work described in this thesis fills several gaps of application of MALDI MSI to understand local metabolisms and their dynamics. The latter is enabled by the use of preclinical animal models, including mice (**chapters 2, 3** and **5**) and rats (**chapter 4**). In **chapters 2–4**, untargeted metabolomics was applied on atherosclerosis and wound healing (**chapters 2** and **3**: atherosclerosis; **chapter 4**: abdominal fascia healing) using MALDI-MSI. Moreover, in **chapter 5**, I applied targeted metabolomics on cancer in mouse model using MALDI-MSI together with ^{13}C isotope labeling.

In **chapter 2**, I applied high-spatial-resolution 2D and 3D MALDI-TOF-MSI to identify and verify aortic plaque-specific lipids witch are common to low density lipoprotein receptor deficient (*ldlr$^{-/-}$*) mice and apolipoprotein E deficient (*apoe$^{-/-}$*) mice, the two most widely used animal models for atherosclerosis. In **chapter 3**, I investigated alterations of metabolites in atherosclerosis of *ldlr$^{-/-}$* mice compared to healthy mice with MALDI-FTICR-MSI. In **chapter 4**, I investigated temporal and *in situ* changes of lipids during the normal healing process of abdominal fascia in the first postoperative week using MALDI-TOF-MSI. In **chapter 5**, I studied L-[ring-^{13}C$_6$]-labeled phenylalanine and tyrosine kinetics in a human non-small cell lung carcinoma xenografted mouse model using MALDI-FTICR-MSI. The supplementary materials for **chapters 2–5** can be found in the appendix page. **Chapter 6** discusses the research findings in this thesis regarding their potential economic and societal impact. **Chapter 7** summarizes the major findings of this thesis and places them in perspectives for future research investigations and their potential biological and clinical implications.

Chapter 2

Atheroma-specific lipids in *ldlr*$^{-/-}$ and *apoe*$^{-/-}$ mice using 2D and 3D matrix-assisted laser desorption/ionization mass spectrometry imaging

Jianhua Cao, Pieter Goossens, Marta Martin-Lorenzo, Frédéric Dewez, Britt S. R. Claes, Erik A. L. Biessen, Ron M. A. Heeren, and Benjamin Balluff. J. Am. Soc. Mass Spectrom, 2020. 31(9): p. 1825-1832.

Abstract

Atherosclerosis is the major contributor to cardiovascular diseases. It is a spatially and temporally complex inflammatory disease, in which intravascular accumulation of a plethora of lipids is considered to play a crucial role. To date, both the composition and local distribution of the involved lipids have not been thoroughly mapped yet. Matrix-assisted laser desorption/ionization (MALDI) mass spectrometry imaging (MSI) enables analyzing and visualizing hundreds of lipid molecules within the plaque while preserving each lipid's specific location. In this study, we aim to identify and verify aortic plaque-specific lipids with high spatial-resolution 2D and 3D MALDI-MSI common to high-fat-diet-fed low-density lipoprotein receptor deficient ($ldlr^{-/-}$) mice and chow-fed apolipoprotein E deficient ($apoe^{-/-}$) mice, the two most widely used animal models for atherosclerosis. A total of 11 lipids were found to be significantly and specifically colocalized to the plaques in both mouse models. These were identified and belong to one sphingomyelin (SM), three lysophosphatidic acids (LPA), four lysophosphatidylcholines (LPC), two lysophosphatidylethanolamines (LPE), and one lysophosphatidylinositol (LPI). While these lysolipids and SM 34:0;2 were characteristic of the atherosclerotic aorta plaque itself, LPI 18:0 was mainly localized in the necrotic core of the plaque.

Introduction

Cardiovascular diseases are the leading cause of death globally, and atherosclerosis is the major contributor. It is a chronic lipid-driven inflammatory disease characterized by atherosclerotic plaques formation in the arterial wall [227, 234, 333].

Atherogenesis is initiated by endothelial dysfunction and activation followed by subendothelial lipoprotein accumulation and subsequent recruitment of immune cells. The resulting atheroma plaque consists of a lipid core and is covered by a plaque-stabilizing fibrous cap. Destabilizing factors such as cell death or calcification can result in rupture of this atheroma, thereby exposing the lipid content to the bloodstream, which can for instance lead to myocardial infarction or stroke [227, 234, 333]. Lipid composition, localization, and alteration along the arterial wall are considered to play a crucial role in the progression of atherosclerosis and the stability of the atheroma [96]. However, lipids constitute an extremely heterogeneous and abundant molecular class, which-combined with the spatial complexity of an atheroma-makes their *in situ* investigation extremely difficult.

In this context, mass spectrometry imaging (MSI) enables analyzing and visualizing hundreds of lipid molecules without labeling while each lipid's specific location in *ex vivo* biological tissue specimens is recorded [18]. Specifically, matrix-assisted laser desorption/ionization (MALDI)-MSI with its flexibility in spatial resolution (down to 10 μm) and in molecular classes (metabolites, proteins, lipids, glycans...) is increasingly applied in biomedical research. MALDI-MSI has demonstrated its unique capability of directly accessing a tissue's molecular content in an unlabeled manner in many studies [30], among them several in the field of cardiovascular diseases [334]. In atherosclerotic research, however, MALDI-MSI remains an underexplored technique with only a few studies, which have so far have focused on the optimization of the experimental conditions and data processing [335-337].

Previous studies of early atherosclerosis using MALDI-MSI in apolipoprotein E deficient ($apoe^{-/-}$) mice and in rabbits have already confirmed the presence of cholesterol in lipid-rich areas of the artery [338], and have led to the identification of several lipid classes in the atheroma, respectively [339]. Nevertheless, these studies either suffer from a low number of samples or did not account for the volumetric complexity of atheromas.

In this study, we therefore address both issues using high spatial resolution 2-dimensional (2D) and three-dimensional (3D) MALDI-MSI to identify aortic plaque-specific lipids in two of the most widely studied mouse models for atherosclerosis. In a first phase, we investigate plaque-specific lipids in 15 low-density lipoprotein receptor deficient ($ldlr^{-/-}$) mice and four $apoe^{-/-}$ mice on a two-dimensional level involving several longitudinal replicates. Subsequently, we verify the volumetric plaque specificity of those lipids by 3D MALDI-MSI in an $apoe^{-/-}$ mouse to confirm the universal presence of these lipids along the plaque.

Materials and methods

Animal models

Fifteen *ldlr*$^{-/-}$ male mice and six *apoe*$^{-/-}$ male mice were studied. Both models were on a C57BL/6 background to the 10th generation (Jackson Laboratory, Bar Harbor, ME, U.S.A.) and developed aortic atherosclerotic lesions under specific dietary conditions. Twelve-week-old *ldlr*$^{-/-}$ mice were fed a high-fat diet containing 16% fat and 0.15% cholesterol (AB Diets, Hope Farms, Woerden, The Netherlands) for 16 weeks. Forty-week-old *apoe*$^{-/-}$ mice had been fed a chow diet. All animals were housed under standard environmental conditions with a 12:12-h light-dark cycle. The mice were sacrificed and their aortic roots were fresh-frozen in OCT compound (Shandon, Veldhoven, The Netherlands) and stored at −80 °C until cryo-sectioning. All animal care and experimental procedures were in compliance with the Guidelines of the Maastricht University Animal Ethics Committee and the EU regulations for animal experimentation.

MSI sample preparation

Fifteen *ldlr*$^{-/-}$ and four *apoe*$^{-/-}$ mice aortic roots were sectioned at 7 μm thickness and perpendicular to the direction of blood flow using a cryo-microtome (Leica CM3050 S, Leica, Wetzlar, Germany), thaw mounted onto indium−tin oxide (ITO) coated glass slides (CG-40IN-S115, Delta Technologies, Loveland, CO, U.S.A.), and stored at −80 °C until further analysis. For the *ldlr*$^{-/-}$ and *apoe*$^{-/-}$ mice, five sections were collected per mouse, each separated by 160 and 130 μm, respectively, to obtain a total of 115 tissue sections for a 2D analysis of the atheroma plaque.

For 3D MALDI-MSI of the whole aortic root from one *apoe*$^{-/-}$ mouse, 130 consecutive sections at 10 μm thickness were collected, where odd and even numbered sections were measured in negative and positive polarity, respectively. For posterior lipid identification, an additional *apoe*$^{-/-}$ mouse aortic root was sectioned at 10 μm thickness and thaw mounted on membrane PEN slides (Leica Microsystems, Wetzlar, Germany).

All ITO slides were dried in a vacuum desiccator for 10 min and fiducial markers (Tipp-Ex, BIC, France) were applied to the ITO slide prior to matrix deposition. A 7 mg/mL norharmane matrix solution was prepared in 2:1 chloroform:methanol (v:v) and homogeneously deposited onto the slides using an automated, temperature-controlled spraying system (TM-sprayer, HTX Technologies, Chapel Hill, NC, U.S.A.). Briefly, 15 layers were sprayed at 30 °C with a constant flow rate of 0.12 mL/min and at a speed of 1200 mm/min combined with 30 s drying time between each layer. Samples were measured immediately after matrix application. 2D and 3D MALDI-MSI Analysis. MSI lipid data within a mass range of *m/z* 400−2000 were acquired on a rapifleX MALDI Tissuetyper (Bruker Daltonik, Bremen, Germany) operating in reflector mode with 200 laser shots accumulated per pixel in both ion modes. For the 2D analysis, 115 sections were measured with a pixel size of 15×15 μm^2 (12×12 μm^2 beam scan region) as follows: 55 sections from

11 *ldlr*$^{-/-}$ animals and 20 sections from 4 *ldlr*$^{-/-}$ mice in negative and positive polarity, respectively, and 20 sections from 4 *apoe*$^{-/-}$ animals for each polarity. For the 3D *apoe*$^{-/-}$ analysis, 75 and 55 tissue sections were measured with a pixel size of 20×20 μm^2 (16×16 μm^2 beam scan region) in negative and positive ion mode, respectively. The instrument was calibrated using red phosphorus before the imaging measurement. Data acquisition and visualization were performed using FlexControl 4.0 and FlexImaging 5.0, respectively (both from Bruker Daltonik).

Histological characterization

After MSI measurements, all ITO slides were washed with 70% methanol for 30 s to remove matrix before hematoxylin and eosin (H&E) staining. The samples were dried in a vacuum desiccator for 10 min, followed by rinsing in hematoxylin (Merck, Darmstadt, Germany) for 1 min, 10 min in tap water, 1 min in distilled water, and another 3 min in eosin (Merck, Darmstadt, Germany). Then, all sections were dehydrated in a graded ethanol series (70%, 2 × 96%, 2 × 100%, 2 min each) and finally rinsed for another 2 min in xylene. Coverslips were mounted onto the slides using a Tissue-Tek SCA 4764 Coverslipper (Sakura Finetek, The Netherlands). After air drying overnight at room temperature, the H&E stained slides were scanned using a digital slide scanner (Mirax Desk, Zeiss, Jena, Germany) and coregistered in FlexImaging to the MSI data using the previously applied fiducial markers. Then, an expert in vascular pathology annotated plaque regions digitally in the scanned images.

Data analysis and 3D reconstruction

For an optimal spectral comparison, all data sets were first recalibrated using FlexAnalysis v3.4 (Bruker Daltonik). Recalibration for the negative ion mode data sets was performed in linear correction mode using *m/z* 885.6 as calibrant with a 1000 ppm peak assignment tolerance. Recalibration for the positive ion mode data sets was performed in quadratic mode using *m/z* 496.3, 524.4, 734.6, 758.6, and 782.6 as calibrants with a 500 ppm peak assignment tolerance. All recalibrated MSI data, coregistered H&E images, and plaque annotations were imported for every polarity separately to SCiLS Lab 2020a (Bruker Daltonik) for further analysis.

In SCiLS Lab, every spectrum was normalized to its root mean square value. The average spectra from each data set were exported to mMass 5.5.013 for peak-picking with the following parameters: (1) S/N ≥ 7.0, peak-picking height = 90%; (2) baseline correction precision: 35 for negative ion mode data sets and 5 for positive ion mode data sets with relative offset = 0; (3) Deisotoping: maximum charge = 1, isotope mass tolerance *m/z* = 0.1, isotope intensity tolerance = 70% and isotope mass shift = 0.0.

Matrix-derived peaks were removed via the loading plot of the principal component 2 (on tissue), resulting in 153 and 164 *m/z* species with a ± 200 ppm mass interval for the 2D data sets in positive and negative ionization modes, respectively.

Plaque specificity of *m/z* species was determined using the Pearson correlation coefficient in SCiLS lab with a minimum correlation coefficient of 0.4. 3D reconstruction and visualization of the *apoe*$^{-/-}$ MSI data was accomplished in SCiLS Lab by manually coregistering each pair of consecutive H&E images using prominent morphological features of the tissues as matched reference points.

Lipid identification

Laser capture microdissection (Leica LMD7000, Leica Microsystems, Wetzlar, Germany) was used to accurately isolate the aortic plaques from 10 *apoe*$^{-/-}$ mouse aortic root sections to obtain the identities of the plaque specific *m/z* signals as found by MALDI-MSI. Laser capture microdissection was performed using the following parameters: wavelength = 349 nm, power = 40, aperture = 11, speed = 10, specimen balance = 1, head current = 100%, and pulse frequency = 310 Hz. All plaque tissues were directly collected in an empty centrifuge tube.

The lipids from the collected plaque regions were extracted using 30 µL of matrix solution (7 mg/mL norharmane in 2:1 chloroform:methanol). The supernatant was spotted on an empty ITO slide for subsequent MALDI-MS/MS measurements using a Q-Exactive Hybrid Quadrupole-Orbitrap Mass Spectrometer (Thermo Fisher Scientific, Bremen, Germany) coupled to a MALDI source (Spectroglyph, Kennewick, U.S.A.). MS1 spectra from both mouse models were acquired within the mass range *m/z* 400−1000 in both ion modes with the following settings: mass resolution = 240,000 (@*m/z* 200), laser repetition rate = 1000 Hz, HPF pressure = 7.5 Torr, and velocity = 2 mm/sec. MS2 measurements were performed on supernatant from lipid extraction by using normalized collision energy in a range of 25−30 eV and a ± 0.5 Da isolation window while continuously moving the stage, with 25 scans averaged for each precursor. The online ALEX123 database (http://alex123.info/ALEX123/MS.php) was used for lipid assignments by matching the MS1 values and where available also the MS2 fragments with a mass tolerance of 3 and 5 ppm, respectively.

Result

Plaque-specific Lipids

To identify lipids specifically confined to the plaque, we analyzed atherosclerotic aortic roots from 15 high-fat diet fed *ldlr*$^{-/-}$ mice and four chow-diet fed *apoe*$^{-/-}$ mice using MALDI-MSI in both polarities. In total, 317 *m/z* species were detected in both data sets with a signal-to-noise ≥7. Spatial correlation analyses were used to find plaque colocalized *m/z* species with a Pearson coefficient ≥0.4 between the MSI images and the histology-based annotations of the atheroma plaque regions. This was done separately for the two mouse model data sets and resulted in 33 plaque specific *m/z* species for the *ldlr*$^{-/-}$ mice (Figure 2.1a, Supplementary Table 2.1) and 43 for the *apoe*$^{-/-}$ mice (Figure 2.1a, Supplementary Table 2.2). Representative MSI images of plaque colocalized *m/z* species in *ldlr*$^{-/-}$ mice in negative (n

= 10) and positive (n = 23) ion mode are shown in Supplementary Figures 2.1 and 2.2, respectively. MSI images of plaque-colocalized m/z species in the $apoe^{-/-}$ mice in negative (n = 24) and positive (n = 19) ion modes are shown in the Supplementary Figures 2.3 and 2.4, respectively.
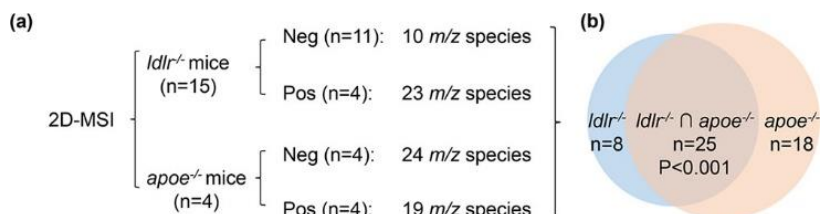
Figure 2.1. Study design and results of common plaque-specific lipids. Two-dimensional (2D) MALDI mass spectrometry imaging (MSI) was performed on aortic roots from 15 $ldlr^{-/-}$ and four $apoe^{-/-}$ mice in positive (Pos) and negative (Neg) ionization modes, which resulted in 33 and 43 m/z species spatially correlated to the plaque for the $ldlr^{-/-}$ and $apoe^{-/-}$ mouse models, respectively (a). The overlap of these plaque-specific m/z species between both mouse models was 25, which was statistically significant (P < 0.001) using a hyper-geometric test (b).

Both mouse models had 25 plaque-specific m/z species in common (Figure 2.1b). All of these, except m/z 496.6, were identified using high-mass resolution MS1 and M2 experiments and belong to 18 lipids, as detailed in Table 2.1. All MS/MS spectra are shown in Supplementary Figures 2.5−2.22. Five m/z species were found to correspond to mixtures of lipids based on MS1 and MS2 levels, leaving 11 unambiguously identified lipids (Table 2.1), comprising 1 sphingomyelin (SM) and 10 lysolipids. Lysolipids correspond to 3 lysophosphatidic acids (LPA), 4 lysophosphatidylcholines (LPC), 2 lysophosphatidylethanolamines (LPE), and 1 lysophosphatidylinositol (LPI).

Table 2.1. Twenty-five plaque-specific m/z species in both, $ldlr^{-/-}$ and $apoe^{-/-}$, mouse models.

Observed m/z by TOF	Pearson correlation coefficient		Observed m/z by Orbitrap	Lipid assignment	MS experiment level for ID	Ion mode	Mass error (in ppm)
	$ldlr^{-/-}$	$apoe^{-/-}$					
409.3	0.47	0.61	409.2366	[LPA 16:0–H]⁻	MS1	NEG	+1.3
459.2	0.50	0.46	459.2476	[LPA 18:1+Na]⁺	MS1	POS	-1.3
463.3	0.41	0.54	463.2839	[LPA 20:1–H]⁻	MS1	NEG	+1.9
464.3	0.44	0.59	464.3142	[LPE O-18:1–H]⁻	MS1	NEG	-1.0
480.3	0.52	0.62	480.3099	[LPE 18:0–H]⁻/ [LPC 16:0–CH₃]⁻	MS2	NEG	+0.6

482.3	0.55	0.50	482.3600	[LPC O-16:0+H]$^+$/ [LPE O-19:0+H]$^+$	MS1	POS	-1.0
487.3	0.47	0.44	487.2790	[LPA 20:1+Na]$^+$	MS1	POS	-1.0
496.3	0.58	0.62	496.3398	[LPC 16:0+H]$^+$	MS2	POS	+0.0
496.6	0.60	0.49	/	/	/	POS	/
506.3	0.43	0.41	506.3257	[LPC 18:1-CH$_3$]$^-$/ [LPE 20:1-H]$^-$	MS1	NEG	+1.0
510.4	0.59	0.55	510.3554	[LPC 17:0+H]$^+$ / [LPE 20:0+H]$^+$	MS1	POS	+0.0
518.3	0.59	0.63	518.3216	[LPC 16:0+Na]$^+$	MS2	POS	-0.2
520.3	0.63	0.63	520.3400	[LPC 18:2+H]$^+$	MS2	POS	+0.4
522.4	0.56	0.59	522.3557	[LPC 18:1+H]$^+$	MS2	POS	+0.6
524.4	0.45	0.52	524.3706	[LPC 18:0+H]+	MS2	POS	-0.9
534.3	0.57	0.57	534.2951	[LPC 16:0+K]$^+$	MS2	POS	-0.9
538.4	0.43	0.53	538.3862	[LPC 19:0+H]$^+$/ [LPE 22:0+H]$^+$	MS1	POS	-1.0
542.4	0.58	0.57	542.3213	[LPC 18:2+Na]$^+$	MS1	POS	-0.8
544.4	0.59	0.57	544.3389	[LPC 18:1+Na]$^+$	MS2	POS	+2.8
546.4	0.56	0.49	546.3540	[LPC 18:0+Na]$^+$	MS2	POS	+1.8
560.3	0.49	0.45	560.3123	[LPC 18:1+K]$^+$	MS2	POS	+0.0
562.3	0.49	0.49	562.3278	[LPC 18:0+K]$^+$	MS2	POS	+0.0
599.3	0.41	0.52	599.3216	[LPI 18:0–H]$^-$	MS2	NEG	+2.4
689.6	0.42	0.53	689.5620	[SM d18:0_16:0-CH$_3$]$^-$	MS2	NEG	+0.7
727.6	0.40	0.44	727.5731	[SM 34:0;2+Na]$^+$	MS2	POS	+1.0

Representative MSI images of plaque co-localized lipids LPA 16:0 and LPC 18:2 in both mouse models in negative and positive ion mode are shown in Figures 2.2 and 2.3, respectively. These images show that the in situ localization and plaque correlation of these common lipids are very similar in both animal models (Supplementary Figures 2.1−2.4). Interestingly, we observed m/z 599.3 (LPI 18:0) to be nonhomogeneously distributed within the plaque. Using annotations of characteristic plaque features, we found LPI 18:0 to be specifically localized in the necrotic core region (Figure 2.4). This was observed consistently in both animal models.
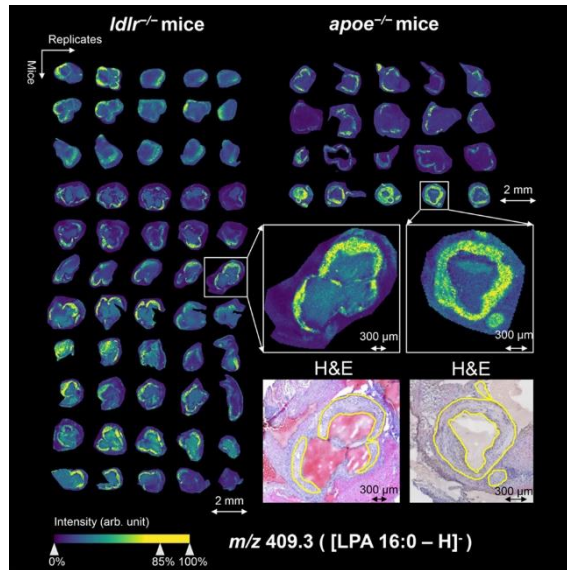
Figure 2.2. Visualization of m/z 409.3 (LPA 16:0) in aortic roots of $ldlr^{-/-}$ mice and $apoe^{-/-}$ mice in negative ion mode. On the left, the MALDI mass spectrometry imaging visualization of LPA 16:0 is shown for 55 different tissue sections of 11 $ldlr^{-/-}$ mice, and on the right for 20 different tissue sections of 4 $apoe^{-/-}$ mice, showing specific plaque localization in all aortas. Magnifications of two representative tissue sections are depicted on the lower right together with their coregistered, hematoxylin and eosin (H&E)-stained images (plaque circumferences are indicated in yellow).
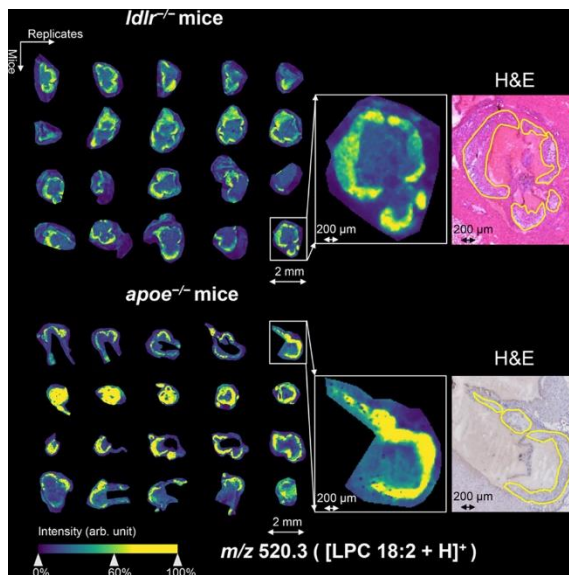
Figure 2.3. Visualization of *m/z* 520.3 (LPC 18:2) in aortic roots of *ldlr*$^{-/-}$ mice and *apoe*$^{-/-}$ mice in positive ion mode (with weak denoising). On the left, the location of LPC 18:2 in 40 different tissue sections of four mice from every mouse model is shown as detected by MALDI mass spectrometry imaging. Magnifications of selected tissue sections and their coregistered, hematoxylin and eosin (H&E)-stained images are shown in the right-hand side (plaque circumferences are indicated in yellow).
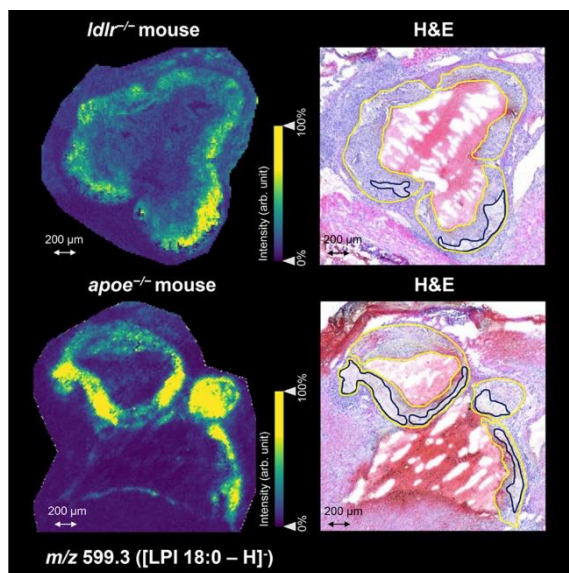
Figure 2.4. Visualization of *m/z* 599.3 (LPI 18:0) in aortic roots of *apoe*$^{-/-}$ and *ldlr*$^{-/-}$ mouse in negative ion mode. On the left, the location of LPI 18:0 is shown as detected by MALDI mass spectrometry imaging in both mouse models. On the right, the coregistered hematoxylin and eosin (H&E)-stained images demonstrate that LPI 18:0 is particularly confined to the necrotic core regions within the plaques (plaque and necrotic core circumferences are indicated in yellow and dark blue, respectively).

Volumetric evaluation of plaque-specific lipids

To investigate the volumetric distribution of the 11 plaque-specific lipids along the plaque's length, 55 and 75 20 μm-spaced tissue sections from an aortic root of one *apoe*$^{-/-}$ mouse were measured by MSI in positive and negative ion mode, respectively. Spatial correlation analysis to plaque annotations across all sections of the 3D MSI data was performed for the 25 *m/z* species belonging to the 11 lipids of interest. Twenty two *m/z* species (Supplementary Table 2.3), which represent 10 unambiguously identified lipids, were found to have a correlation coefficient of at least 0.4 across the whole plaque. This analysis hence confirmed that 10 (LPA 18:1, LPA 20:1, LPE O-18:1, LPE 18:0, LPC 16:0, LPC 18:0, LPC 18:1, LPC 18:2, LPI 18:0, and SM 34:0;2) out of the 11 lipids can be considered plaque-specific in all three dimensions of the plaque. The 3D spatial distributions of selected lipids along the bloodstream direction are shown in longitudinal view in Figure 2.5a, where the signals belonging to *m/z* 480.3 (LPE 18:0/LPC 16:0) and *m/z* 599.3 (LPI 18:0) delineate the plaque and necrotic core areas, respectively. Supplementary Video 2.1 shows the 3D reconstruction of *m/z* 480.3 (LPE 18:0/LPC 16:0) in rotation. Furthermore, the spatial correlation analysis was performed individually for every section of the 3D MSI data set to obtain a more detailed view on the specificity of these lipids for plaque and necrotic core areas along the third dimension. Figure 2.5b shows the variation of the correlation coefficients of *m/z* 480.3 (LPE 18:0/LPC 16:0) to the plaque area and of *m/z* 599.3 (LPI 18:0) to the necrotic core area, and Supplementary Figure 2.23 shows the remaining lipids.
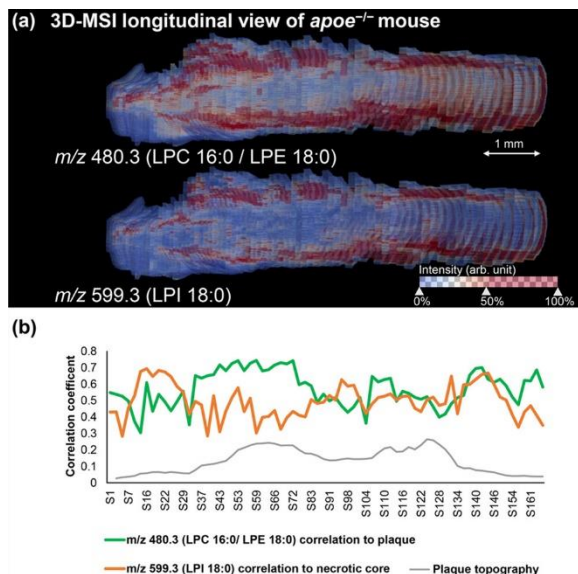
Figure 2.5. Three-dimensional longitudinal visualization of the plaque-specific lipids *m/z* 480.3 (LPE 18:0/LPC 16:0) and *m/z* 599.3 (LPI 18:0) as detected by 3D MALDI mass spectrometry imaging in an aortic root of an *apoe*$^{-/-}$ mouse (a). Spatial correlation analysis was performed for *m/z* 480.3 (LPE 18:0/LPC 16:0) on the annotated plaque area and for *m/z* 599.3 (LPI 18:0) on the annotated necrotic core area, respectively, on a section-by-section basis.

This allows showing the variation of the correlation of two lipids to the respective annotations along the z-direction of the plaque (b). The blood flow direction is from left to right.

Discussion

In this study we aimed to identify aortic plaque-specific lipids by high-spatial-resolution MALDI-MSI and 3D MALDI-MSI in high-fat-diet-fed low-density lipoprotein receptor deficient ($ldlr^{-/-}$) mice and chow-fed apolipoprotein E deficient ($apoe^{-/-}$) mice. These two mouse models are the most-widely investigated mouse models in cardiovascular research. As the pathogenesis and manifestation of atherosclerosis in both models is slightly different [239], identifying common molecular mechanisms harbors the potential to better understand key processes in the development of atherosclerosis.

Previous studies have already used MALDI mass spectrometry imaging to study the lipidic composition of the atheroma plaque in human [336, 337, 340] or $apoe^{-/-}$ mouse model samples [338]. We could confirm the observation of most LPCs (Table 2.1), several ceramide species (Supplementary Table 2.2), cholesteryl esters (CEs), and oxysterols to be localized in the plaque (Supplementary Figures 2.24−2.25), although the latter two did not pass our peak picking thresholds. Our study complements these results by confirming the presence of those lipids also in $ldlr^{-/-}$ mice and adding to that list other plaque-specific lysolipids such as several LPAs, LPEs, and LPIs. Using a higher spatial resolution (15 μm) than previous studies allowed us to spot certain lipid species in subcompartments of the plaque. Furthermore, all lipid identifications are based on high-mass resolution MS1 ($R_{observed}$ ~ 120,000@m/z 800) or MS2 measurements, thereby providing a higher certainty of the molecular identities.

Using an additional 3D approach allowed us to investigate the specificity of the detected lipids along the third dimension of the plaque. That we analyzed the entire plaque can be seen in Figure 2.5b where the plaque's hill-shaped topography is shown on the basis of the size of the annotated plaque areas in each section. This analysis also shows that the lipids' spatial specificity remains stable along the z-direction of the plaque and is independent of the blood flow direction.

Most of our identified lipids are lysophospholipids, including LPA, LPC, LPE, and LPI species, suggesting that in both mouse models the plaque lipid pool is mainly composed of different lysophospholipids. Lysophospholipids are bioactive lipid-derived metabolic intermediates in biodegradation of membrane phospholipids and act as extracellular mediators involved in development and progression of atherosclerosis [341]. LPCs are major plasma lipids that are highly enriched in oxidized low-density lipoprotein (oxLDL), a highly proatherogenic modified lipoprotein [342]. Although a recent MSI study by Diehl *et al*. has shown the presence of LPCs at the highest vulnerable plaque regions in humans [340], to the best of our knowledge, we have shown for the first time that LPC 16:0, LPC 18:0, LPC 18:1, and LPC 18:2 are specifically and exclusively located in the atheroma plaque and not in the rest of the artery in both mouse models. Interestingly, these lipid species have been related

with a higher incidence of cardiovascular diseases in serum and plasma samples [343-345], where serum levels have been related to different grades of calcification in coronary artery disease [346]. Serum LPC 18:2 has also been proposed as myocardial infarction biomarker [347]. This makes an interesting link between highly abundant blood circulating lipids and plaque-specific lipids that should be further studied.

Several LPA species including 16:0, 18:1, and 20:1 were detected in the plaques of both mouse models. The relation of LPAs with atherosclerosis and specifically with the atheroma plaque has been studied earlier by us [348, 349] and others [350] concluding that there is strong evidence that LPAs participate in formation and rupture of the plaque [348, 350]. LPAs have been previously found to accumulate in the central atheroma in human and mouse plaques [351]. Indeed, LPA 16:0 and LPA 18:1 have been detected before in carotid mice plaques [349]. However, LPA 20:1 has not been related before to atherosclerosis, neither has it been specifically located within the atheroma plaque. The presence of both, LPAs and LPCs, has been related with highly vulnerable plaques and poor prognosis [340, 351]. It has been suggested that plaque rupture exposes these lysophospholipids, which in turn activate platelets. This results in an increase of aggregates and thrombogenic potential, leading to a fatal event.

In the present work, we identified specific LPAs (LPA 16:0, 18:1, 20:1) and LPCs (LPC 16:0, 18:0, 18:1, 18:2) in the plaque area. The specific characterization of these LPAs/LPCs is a step forward because there is evidence that the fatty acid composition and the linkage of the fatty acid to the glycerol backbone may affect this platelet activation [352] and subsequently affect the stability of the plaque. LPEs and LPIs in atherosclerosis have been less studied than other lysolipids, which might be attributed to their lower abundance. Different species of LPE have been detected in plasma in association with incident cardiovascular disease but without statistical significance [345]. We have identified and correlated the specific presence of LPE 18:0 and LPE O-18:1 in the atheroma plaque. In this respect, it is also the first time that LPI 18:0 has been found particularly localized in the necrotic core of plaques in both mouse models, but its role in necrosis is presently unknown. However, we can hypothesize that the presence of LPI in the necrotic core is related to poor prognosis. The necrotic core is not only one of the most vulnerable plaque components, but also appears to be the most thrombogenic component. Moreover, high levels of LPI have been related with a poor outcome in acute myocardial infarction [353]. Nevertheless, the specific role of this LPI in necrosis still has to be explored with other techniques.

The high levels of the lysolipids identified here in the plaques can be related with different mechanisms. On the one hand, LPI, LPE, and LPC are generated from their correspondent phospholipid (i.e., phosphatidylinositol, phosphatidylethanolamine, and phosphatidylcholine) [354, 355]. On the other hand, LPA is mainly produced from LPC by autotaxin [350]. In that line, LPA accumulation has been related to an increase of LPC as precursor of LPA [349]. The high abundance of LPC 16:0 and 18:1, LPA 16:0 and 18:1 suggests an intraplaque LPA

production which would be in agreement with previous findings [348, 349]. Besides, the participation of minor lysophospholipids may be also involved in the in situ synthesis [350], and in this sense the presence of LPA 16:0 together with LPC 16:0 and LPA 18:1 together with LPC 18:1 could be related with this lysolipids interchange mechanism. However, more experiments and research on this in situ formation or direct accumulation should be done.

Another lipid class that has been associated with plaque is sphingomyelin (SM) [96, 337, 356]. SMs are a subgroup of sphingolipids, which are formed via derivation of palmitoyl-CoA and Lserine [357]. We detected two SM species (SM 34:0;2 and SM 34:1;2) in both ionization modes of which only SM 34:0;2 was significantly localized in plaques of both mouse models (Supplementary Figure 2.26). Interestingly, no other MSI study has ever reported SM 34:0;2 to be plaque specific. While in our study SM 34:1;2 was only found in plaques of *apoe*$^{-/-}$ mice (correlation coefficient >0.5) and to lower extent in *ldlr*$^{-/-}$ mice (correlation coefficient = 0.35), others have found this lipid in human coronary arteries [337, 356]. In plasma, several studies have found SM levels in human plasma to be indicative of coronary heart diseases [357, 358]. The role of SMs has been investigated in animal models, which showed that atherosclerotic lesions progressed with a SM-rich diet [359].

The use of mouse models limits the certainty by which results can be translated directly to the human disease condition. In this study, we have focused our analysis and discussion on the commonalities of two of the most common and understood mouse models in atherosclerosis. The fact that our results are consistent across the two different models is promising and indicates that they could be extended to the study of human plaque and plasma samples.

Conclusion

2D and 3D MALDI mass spectrometry imaging was used to comprehensively investigate the lipid profile of murine atherosclerotic plaque tissue, in two distinct mouse models using technical and biological replicates. The study identified 11 plaque-specific lipids present in both atherosclerotic mouse models. All the results presented in this study suggest that lysolipids and sphingomyelins are integral constituents of the plaque in atherosclerosis. More specifically, LPI 18:0 was concentrated in the necrotic core of plaques. These novel results unravel the molecular complexity of the atherosclerotic plaque enhancing not only our understanding of plaque composition but also the identification of potential plaque lipid species related with plaque stability.

Chapter 3

Metabolic alterations of atherosclerosis in LDLR-deficient mice using matrix-assisted laser desorption/ionization mass spectrometry imaging

Jianhua Cao*, Marta Martin-Lorenzo*, Kim van Kuijk, Marion J. Gijbels, Britt S. R. Claes, Ron M.A. Heeren, Judith Sluimer, Gloria Alvarez-Llamas, Benjamin Balluff (In preparation)

Chapter 4

Abdominal fascial healing in the first postoperative week: a MALDI-TOF mass spectrometry imaging to investigate lipids in rats

Hong Liu *, **Jianhua Cao** *, Benjamin Balluff, Audrey C.H.M. Jongen, Marion J. Gijbels, Jarno Melenhorst, Ron M.A. Heeren, Nicole D. Bouvy. Journal of Mass Spectrometry and Advances in the Clinical Lab, 2021. 20: p. 35-41.

Abstract

Failure of fascial healing in the abdominal wall can result in incisional hernia, which is one of the most common complications after laparotomy. Understanding the molecular healing process of abdominal fascia may provide lipid markers of incisional hernia or therapeutic targets that allow prevention or treatment of incisional hernias. This study aims to investigate temporal and in situ changes of lipids during the normal healing process of abdominal fascia in the first postoperative week. Open hemicolectomy was performed in a total of 35 Wistar rats. The midline fascia was closed identically for all rats using a single continuous suturing technique. These animals were sacrificed with equal numbers (n = 5) at each of 7-time points (6, 12, 24, 48, 72, 120, and 168h). The local and temporal changes of lipids were examined with mass spectrometry imaging and correlated to histologically scored changes during healing using hematoxylin and eosin staining. Two phosphatidylcholine lipid species (PC O-38:5 and PC 38:4) and one phosphatidylethanolamine lipid (PE O-16:1_20:4) were found to significantly correlate with temporal changes of inflammation. A phosphatidylcholine (PC 32:0) and a monosialodihexosylganglioside (GM3 34:1;2) were found to correlate with fibroblast cell growth. In summary, glycerophospholipids and gangliosides are strongly involved in the normal healing process of abdominal fascia and their locally fluctuating concentrations are considered as potential lipid markers and therapeutic targets of fascial healing.

Introduction

Incisional hernia (IH) is one of the most common complications after laparotomy, caused by failed healing of abdominal fascia [398-400]. The incidence of IH following laparotomy is around 13% within two postoperative years [401] and related costs are estimated at billions of Euros for Europe alone [402, 403]. Despite the significant importance of normal fascial healing in preventing IH, few studies have illustrated the temporal healing process, especially on the molecular level, in the early post-surgery period.

Generally, cellular and molecular events proceed sequentially with four stages: haemostasis, inflammation, proliferation, and remodelling. Despite wound healing of virtually all soft tissues passing through these stages, cells and molecules in fascial healing differ from other specific tissues [404]. Previous studies have illustrated that the healing rate of abdominal fascial incisions varies from skin wounds [405-407]. Controversy exists with regard to the healing rate between these two injured tissues. Lemonnier *et al*. have reported that fascial fibroblasts in culture have longer cell-doubling times, larger cell volume, and higher glucose requirements, compared to dermis fibroblasts [407]. European Hernia Society guidelines recommend the use of slowly absorbable sutures for the closure of abdominal fascial incision versus rapidly absorbable sutures because of the high risk of incisional hernia occurrence when using rapidly absorbable sutures [408, 409]. In contrast, sutures supporting skin wounds can be removed within one to two weeks postsurgery. However, Michael and Dubay have concluded that abdominal fascial incisions regain tensile strength faster than the cutaneous wound in a rat model [405, 406].

Lipids, acting as signalling molecules, as well as structural components of cell membranes, play a critical role in cell structure and function [410, 411]. Lipid mediators can affect the cellular biology related to wound healing. For example, diacylglycerol is essential for cellular processed during wound healing [412]. Lysophosphatidic acid (LPA) enhances the reepithelialisation in the early healing stages of the ear skin in a mouse model [413]. Arachidonic acid (AA) promotes skin wound healing in in vitro experiments [414], and eicosanoids derived from arachidonic acid may modulate inflammatory reactions during the healing process [415].

Analysis of lipid profiles during wound healing has benefited from recent developments in mass spectrometry [416]. Matrix-assisted laser desorption/ionization-time of flight (MALDI-TOF) mass spectrometry imaging (MSI) can analyze and localize lipids directly from their native tissues and enables label-free visualization of lipid spatial distribution [417, 418]. Compared to commonly used methods of lipid analysis, like thin-layer chromatography or high-performance liquid chromatography, MALDI-TOF MSI for lipid analysis is less time-consuming while conserving the spatial distribution of molecules [419]. Furthermore, compared to electrospray ionization, MALDI is more sensitive and less affected by impurities [419]. A previous study has employed MALDI-TOF MSI to identify lipids in the skin wound healing process [420].

This study aims to investigate temporal lipid changes correlated with cellular changes during normal fascial healing in the first postoperative week in rats. Rat models have been chosen in this study to mimic human healing as they are genetically similar to humans [421] and it is ethically impossible to isolate functionally healed fascia from patients.

Materials and methods

Animal experiment

A total of 35 adult male Wistar rats (n = 35), weighing 250–300 g, were obtained from Harlan UK Ltd (Biscester, UK). The animal experiment was approved by the Dutch Central Committee (2014–120), complying with the Dutch Animal Experimental Act. Two animals were housed in one Macro cage (EU type IV, 1800 cm2) filled with hygiene animal bedding with enrichments of cardboard and wooden blocks, fitted with a 12-hour light-night circle and maintained at 25 °C. Animals were permitted to access food (10 mm Sniff rat/mouse sterilized food compressed into pellets) and drink (acidified water) ad libitum. Surgeries were performed in a standard operation room in a randomized manner starting the morning of each operation day. All animals were healthy and did not receive any medication or treatments prior to the experiment. Following at least one week of acclimatization, animals were anesthetized with 2% isoflurane (IsoFlo®, zoeris) and disinfected with 2% iodine solution. Buprenorphine 0.05 mg/kg was administered to all animals prior to the surgical procedures. A midline incision around 5 cm was made on the abdominal skin and then, separately, a 5 cm midline incision was made on the fascia until the peritoneal cavity. After ascending colon resection and anastomosis, the fascia was closed continuously with Vicryl TM 4–0 suture (Ethicon Inc; Johnson&Johnson, Somerville, NJ). Buprenorphine 0.05 mg/kg was subcutaneously applied to all animals for pain relief every 8 to 12 h until no signs of pain were observed. The welfare of all animal was evaluated using a 12 item welfare sheet, including activity, behavior, gait, posture, physical condition, fur/skin, hydration, breathing, faeces/urine, surgical wound, edema, and necrosis. At each of seven time points (6, 12, 24, 48, 72, 120, and 168 h), five animals were sacrificed by cardiac puncture with complete blood draw under anaesthesia. Buprenorphine 0.05 mg/kg was subcutaneously administered to all animals half an hour prior to sacrifice. All animals received the identical surgical procedure. Samples from rats, including fascial incision, sutures and surrounding muscle, were immediately snap frozen with liquid nitrogen and stored at −80 °C until measurement.

Sample preparation

A cryo-microtome (Leica CM 1860 UV, Leica Biosystems, Wetzlar, GE) was pre-equilibrated to −20 °C more than half an hour before cutting. Samples were sectioned at 10 µm thickness and thaw mounted on pre-cooled Indium Tin Oxide coated (ITO) slides. Slides were dried in desiccator for 15 min prior to matrix application.

Twelve layers of 7 mg/ml norharmane matrix solution (2: 1 chloroform/methanol (v: v)) were applied to the tissue sections using a HTX TM-sprayer (HTX Technologies, Chapel Hill, NC)

at a 30 °C nozzle temperature and 0.120 mL/min flow rate. Norharmane and chloroform were obtained from Sigma Aldrich (Zwijndrecht, the Netherlands). Methanol was obtained from Biosolve BV (Valkenswaard, the Netherlands).

MSI data acquisition

All sections were measured with Bruker Rapiflex MALDI-TOF/TOF Tissuetyper (Bruker Daltonik GmbH, Bremen, Germany) in reflector mode, in both ionization modes scanning a mass range of m/z 400–2000 at pixel size of 50 µm × 50 µm. First, tissue sections were analysed using a 20 µm × 20 µm scan pixel area with a 50 µm × 50 µm spacing in the negative ionization mode without offset, and subsequently, measured in the positive ionization mode with an offset of 20 µm × 20 µm, using the same spacing. Red phosphorus spots were pipetted on each individual slide to calibrate the instrument. Calibration was conducted prior to each analysis.

Two consecutive sections from a 120-hour sample with sufficiently different cell types were chosen to perform high spatial resolution (10 µm) mass spectrometry imaging experiments in both ionization modes, separately, using the same matrix application and MSI instrument as mentioned above. The scan area measured 8 µm × 8 µm per pixel.

MALDI-MS/MS lipid identification was performed on selected consecutive sections from the 120-hour group using a Q-Exactive Hybrid Quadrupole-Orbitrap Mass Spectrometer (Thermo Fisher Scientific, Bremen, Germany) coupled to a MALDI source (Spectro-glyph, Kennewick, USA). MS1 spectra in both ionization modes were acquired at a mass range of *m/z* 400–2000 with 550 ms of injection time. MS2 data of seven masses was acquired at 120,000 mass resolution while moving the stage continuously, with 30 scans averaged for each precursor. The normalized collision energy ranged from 20 to 30 eV with an isolation window of ± 0.7 Da. The matching of MS1 values and MS2 fragments (when available) for lipid assignments was conducted with the online ALEX123 database (http://alex123.info/ALEX123/MS.php), using a mass tolerance of 3 ppm and 5 ppm, respectively.

Histological staining after MSI

All measured tissue sections were stained with haematoxylin and eosin (H&E) and mounted with coverslips. After air-drying overnight, digital H&E image was recorded using a Mirax digital slide scanner (Zeiss, Jana, Germany). The inflammatory score and fibroblast score were determined by an experienced pathologist of Maastricht University (M.G.) without knowledge conditions to which the tissues were subjected. The microscopically assessed inflammation and fibroblast scores were described using a 0–5 scale (0, not present; 1, slightly present; 2, more than slightly present; 3, moderately present; 4, more than moderately present; 5, abundantly present). The inflammation scores refer to the total amount of granulocytes and macrophages. The histological scores were tested with linear regression or generalized linear model, when applicable. Statistical analysis of histological scores was

conducted using IBM SPSS Statistics for Windows (version 25.0, Armonk, NY, USA, IBM Corp.).

MSI data processing

Recalibrations for both the negative and positive ionization mode datasets were performed using FlexAnalysis v3.4 (Bruker Daltonik GmbH, Bremen, Germany) in linear correction mode using m/z 885.6 and m/z 782.6 as calibrants, respectively. H&E images were co-registered with the MSI data using FlexImaging 4.1 software (Bruker Daltonik GmbH, Bremen, Germany), and connective tissues in the fascial incision and adjacent partial muscles were annotated with histological structure. After recalibration, co-registration, and annotation, all data were imported into the SCiLS Lab 2019b (SCiLS GmbH, Bremen, Germany) and root mean square normalized.

The average spectra from each dataset was exported to mMass 5.5.0 for peak-picking with the following parameters: (1) signal-to-noise (S/N) ratio of 7.0, peak-picking height of 75 and 90 for positive and negative ionization mode, respectively; (2) baseline correction precision of 35 for both positive and negative ionization mode with relative offset at 0; (3) Deisotoping: maximum charge of 1, isotope mass tolerance of 0.1 *m/z*, isotope intensity tolerance of 70%, and isotope mass shift of 0.0. Linear regression analysis (P value threshold = 0.05) was performed in R (v3.5) to model the relationship between the intensity of any *m/z* species and the healing time. P-values were corrected for multiple testing using the Benjamini-Hochberg method.

Pearson correlation analysis (threshold ≥ 0.4) among different annotated cell regions (typical clusters of smooth muscle cells, granulocytes and macrophages, and fibroblasts) in 10 µm high spatial resolution MSI datasets were conducted using the significant masses we found in the linear regression analysis to obtain *m/z* species co-localised to inflammation and fibroblast regions.

Results

Animal experiment

No complications, including dehiscence of the fascial incision and skin wound, anastomotic leakage, and wound infection, were identified after surgery in 34 out of 35 rats. One rat from the 120-hour group developed ileus, which potentially can affect normal fascial healing negatively because of increased abdominal pressure, and was subsequently excluded from further MSI and histological analysis.

Linear regression analysis for 50 µm spatial resolution MSI data

Representative MSI and H&E images are displayed in Figure 4.1. A total of 33 MSI negative mode MSI datasets and 31 MSI positive mode datasets were included for MSI data analysis. Three samples were excluded from further MSI data analysis, including one sample from the 168-hour group in both negative and positive ionization MSI data, one from the 48-hour

group and one from the 72-hour group in positive ionization mode due to sample contamination. On average, 174 and 176 of the *m/z* species were detected after peak picking in negative and positive ionization modes, respectively. A total of 18 and 35 of the *m/z* species were identified using linear regression analysis to identify consistent trends over time (P value threshold = 0.05) in negative and positive ionization modes, respectively (Supplementary Figure 4.1). Representative *m/z* values identified with a temporal increase and decrease are presented in Figure 4.2. The identification of these *m/z* species are shown in Supplementary Table 4.1.
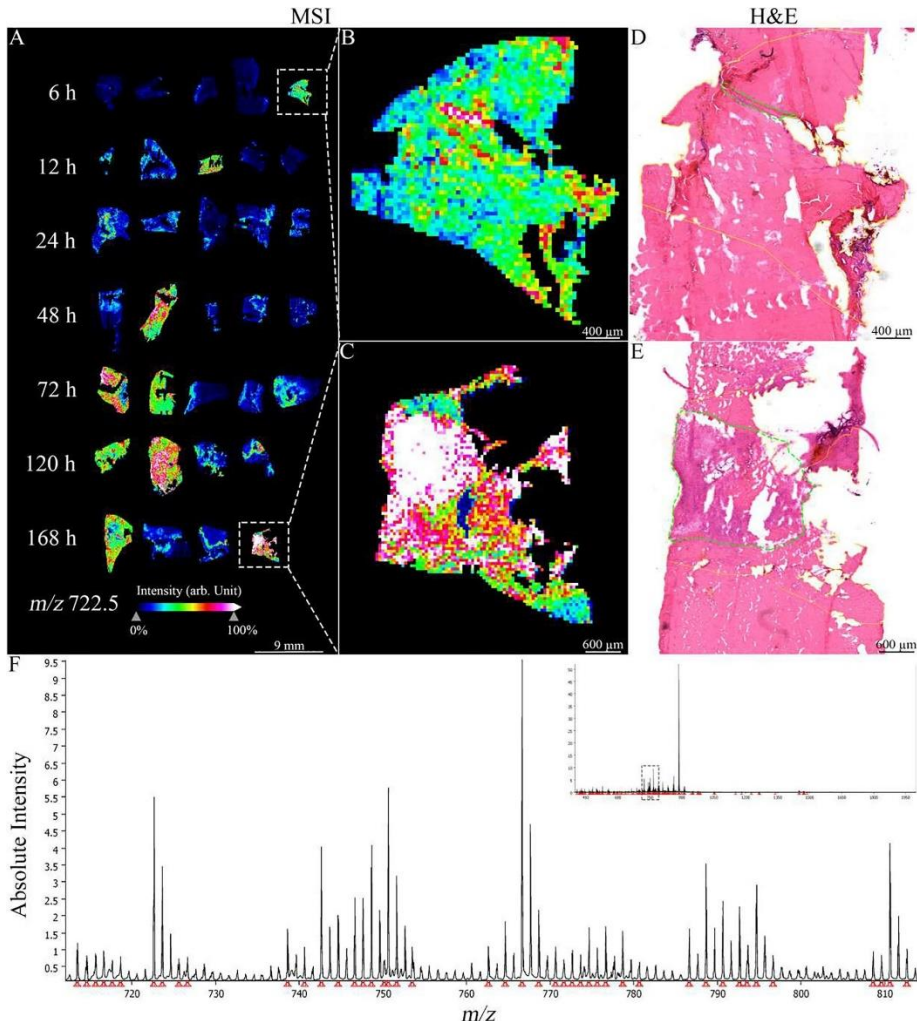
Figure 4.1. Representative MSI and H&E images.Visualization of *m/z* 722.5 (PE O-16:1_20:4) at different time points in negative ionization mode (A). Magnifications of two representative tissue sections from 6-hour (B) and 168-hour group (C). Co-registered, hematoxylin and eosin stained (H&E) images with yellow lines representing MALDI-TOF scanned regions and green dashed lines representing regions of fascial incision (D and E). Average spectra in negative ion mode and magnification at mass range *m/z* 700–810 (F).
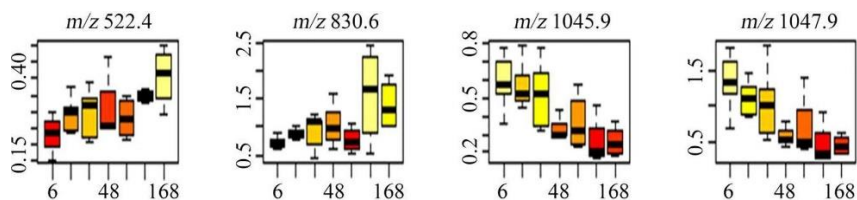
Figure 4.2. Representative *m/z* values identified with a temporal increase and decrease. The x-axis represents time in hours, and the y-axis represents the relative intensity of the *m/z* species.

Statistical analysis of histological score data

The inflammation scores and the fibroblast score increased significantly over time using linear regression (slope, 0.017, P < 0.001) and generalized linear model (P < 0.001), respectively (Figure 4.3).
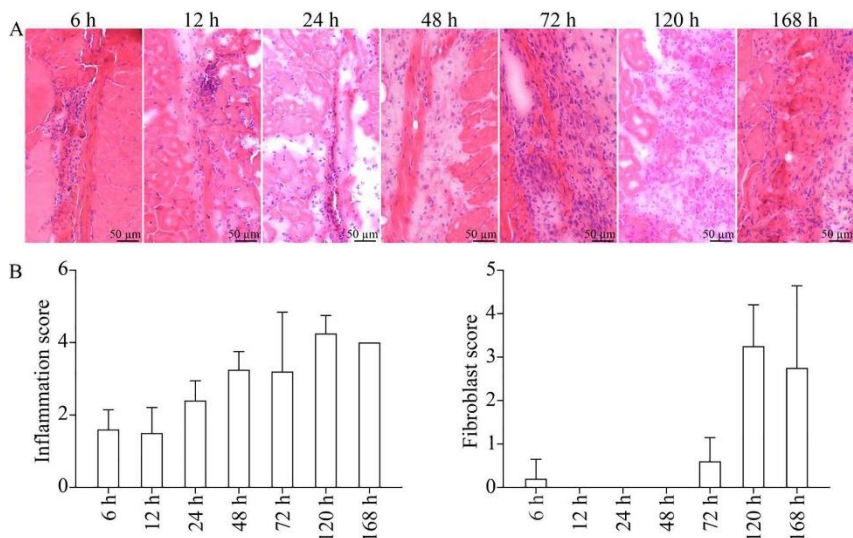
Figure 4.3. A, representative H&E images at each time point. B, inflammation and fibroblast scores at each time point. Bar plot, mean ± standard deviation.

Correlation coefficient analysis based on 10 μm MSI data

A total of eight out of 53 of the *m/z* species were found to correlate with inflammation scores or fibroblast cells with a correlation coefficient of at least 0.4. All of those eight m/z signals, except *m/z* 838.7, were identified using high-mass resolution MS1 and MS2 experiments, leaving five unambiguously identified lipids, comprising three PC lipid species (PC 32:0, PC O-38:5 and PC 38:4), one PE lipid (PE O-16:1_20:4) and one sphingolipid (GM3 34:1;2). Table 4.1 and Table 4.2 show the lipid identifications in detail. All MS/MS spectra are shown in Supplementary Figures 4.3 and 4.4. Two PC lipid species (PC O-38:5 and PC 38:4) and a PE lipid (PE O-16:1_20:4) were correlated with inflammation scores. PC 32:0 and GM3 34:1;2 were found to correlate with fibroblast cells. Representative MSI images of PE O-

16:1_20:4 and PC O-38:5 in negative and positive ionization mode are shown in Figure 4.4. MSI images of the other three lipids are shown in Supplementary Figure 4.2.
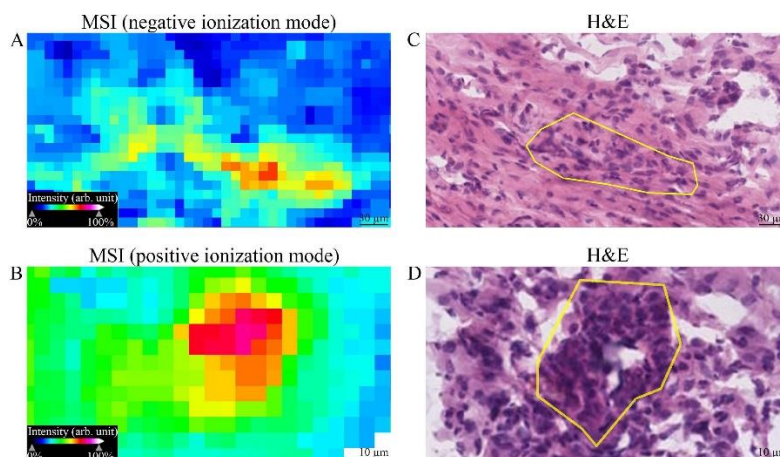
Figure 4.4. Representative MSI images of [PE O-16:1_20:4-H]⁻ (A) and [PC O-38:5 + H]⁺ (B) with weak denoising at 10 µm × 10 µm spatial resolution in negative and positive ionization mode, respectively. Magnification of these tissue sections, and their co-registered hematoxylin and eosin stained (H&E) images, are shown in C and D. Representative inflammation regions are indicated in yellow.

Table 4.1. Four *m/z* species were correlated to temporal changes of the inflammation.

Observed *m/z* by TOF	Pearson correlation coefficient	Observed *m/z* by Orbitrap	Lipid assignment	MS experiment level for ID	Ion mode	Mass error (in ppm)
722.5	0.57	722.5146	[PE O-36:5-H]⁻	MS2	NEG	+2.2
794.7	0.66	794.6037	[PC O-38:5+H]⁺	MS2	POS	-2.7
832.6	0.46	832.5811	[PC 38:4+Na]⁺	MS2	POS	-1.9
838.7	0.46	/	/	/	POS	/

Table 4.2. Four *m/z* species were correlated to temporal changes of the fibroblasts.

Observed *m/z* by TOF	Pearson correlation coefficient	Observed *m/z* by Orbitrap	Lipid assignment	MS experiment level for ID	Ion mode	Mass error (in ppm)
734.6	0.80	734.5685	[PC 32:0+H]⁺	MS2	POS	-1.3
756.6	0.81	756.5505	[PC 32:0+Na]⁺	MS2	POS	-1.2
772.6	0.75	772.5236	[PC 32:0+K]⁺	MS2	POS	-2.2
1151.7	0.45	1151.7059	[GM3 34:1;2-H]⁻	MS2	NEG	+0.0

Discussion

Molecular changes in abdominal fascia caused by surgical injury are essential for fascial regeneration [422, 423]. Due to very limited comparability within previously published animal models mimicking incisional hernia in patients [424], revealing the molecular changes in normal fascial healing over time could provide a better understanding of IH. This study illustrates the temporal changes of lipids correlated to inflammatory response and fibroblast growth in acutely injured fascia. These lipids are potential lipid markers of IH in further animal IH models, or therapeutic targets to promote fascial healing and prevent IH.

Virtually all wound healing passes through similar healing stages [425]. In skin wound healing, the inflammatory response begins within a few hours after an acute injury, and the proliferative stage occurs from 4 to 21 days [426]. In our study, focused on fascial healing, the inflammation score increased over time and fibroblast proliferation started to increase at the middle of the first postoperative week. This indicates that the healing stages of inflammation and proliferation in the early fascial healing are comparable to skin wound healing stages. At the molecular level, several studies have revealed growth factors [427, 428], chemokines [429], cytokines [428, 430], and various phospholipid membrane-derived lipid mediators that are involved in the skin wound healing process, including LPA [431], sphingolipids [432], and eicosanoids [433]. Still, much remains unknown about the molecular mechanism of fascial healing. It is reported that an abdominal fascial incision heals separately from the adjacent skin wound [262]. Dubay *et al.* have demonstrated that abdominal fascial fibroblasts have a significant increase in cell proliferation compared to dermis fibroblasts in a seven-day cell culture [406]. Swarming-like collective cell migration of fibroblasts is exclusive and requires N-cadherin upregulation in fascia, which is lacking in upper skin wound healing [434]. Therefore, the underlying molecules activated during inflammation and proliferation stages during fascial healing should be different from skin wound healing.

The important role of lipids in initiating an acute inflammatory response is widely acknowledged [435]. PCs are one of the most abundant biological components in cell membrane, belonging to a class of phospholipids with choline as a head group [436, 437]. PE can be converted to PC through PE methyltransferases and is involved in the biosynthesis of PC [438, 439]. PC and PE, as two major phospholipids, are key players in cell survival and development. Abnormal variation of PC, PE, or the PC/PE ratio can influence the energy metabolism of organelles, and is linked to various pathological progressions [440]. In our study, the two PC lipid species (PC O-38:5 and PC 38:4) and PE O-16:1_20:4 increased significantly during the first postoperative week, in parallel with an increase in the inflammation score during the normal fascial healing. The correlation coefficients of these lipid species that correlate with inflammation scores exceeded 0.4, suggesting that these lipids are indicators of the inflammatory response in fascial healing. Furthermore, previous evidence has shown that exogenous PC treatments can promote mucosal healing in ulcerative

colitis in patients [441, 442] and may promote surgical wound healing [443]. PCs can be isolated from natural sources or obtained using synthetic or semi-synthetic methods and have excellent biocompatibility [444]. PCs correlated to the inflammatory response in our findings could be applied directly to promote fascial healing in the early postoperative period, although further studies are needed.

Fibroblasts contribute significantly to wound healing, creating extracellular matrix components and contracting the wound [445]. Lipid signaling can affect fibroblast proliferation [446, 447]. The plasma membrane of fibroblasts contains micrometer-scale patches enriched with sphingolipids that can metabolise to signalling molecules regulating cell survival and proliferation [448, 449]. Prostaglandin F2α can stimulate fibroblast proliferation via the prostaglandin receptor, separately from growth factor-beta [450]. In our study, PC 32:0 and GM3 34:1;2 were linked to temporal changes of the fibroblasts, indicating that these two lipids could be fibroblast biomarkers in fascial healing. Additionally, a study has demonstrated that proliferating fibroblasts prefer exogenous lipids as the source of membrane lipids rather than de novo synthesis [451]. GM3 analogues can be synthesized conveniently from commercially available substances [452]. Application of PC 32:0 or GM3 34:1;2 could be a novel strategy to promote fibroblast growth in fascial incision, although further research is needed. It should be noted that GM3, belonging to gangliosides, is involved in mediating growth factor signalling in human skin. GM3 is observed to be a driver of impaired wound healing, and depletion of GM3 can result in improved wound healing in diabetic mice [453, 454]. However, in our studies, GM3 34:1;2 increased over time, positively linked to an increase in fibroblasts. This could be explained by tissue-specific involved molecules that differ between fascial healing and skin wound healing.

Animal models have intrinsic limitations. However, a previous study has demonstrated the molecular comparability between rats and humans regarding healing and scarring using a gene expression comparison [421]. Furthermore, regarding an IH model, histological results between rats and humans are comparable [455]. Therefore, it is possible that the present results could be translated to humans, however further in vivo human confirmation and validation would be necessary.

Conclusion

In summary, five lipids, including PE O-16:1_20:4, PC O-38:5, PC 38:4, PC 32:0, and GM3 34:1;2, were found to be significantly involved in fascial healing and have the potential to be lipid markers and/or therapeutic targets for the prevention of IH in patients, although further studies evaluating the functional effect of these lipids in fascial healing are needed.

Chapter 5

Mass spectrometry imaging of L-[ring-^{13}C$_6$]-labelled phenylalanine and tyrosine kinetics in non-small cell lung carcinoma

Jianhua Cao, Benjamin Balluff, Martijn Arts, Ludwig J. Dubois, Luc J. C. van Loon,Tilman M. Hackeng, Hans M. H. van Eijk, Gert Eijkel1, Lara R. Heij, Zita Soons, Steven W. M. Olde Damink, Ron M. A. Heeren. Cancer Metab, 2021. 9(1): p. 26.

Abstract

Metabolic reprogramming is a common phenomenon in tumorigenesis and tumor progression. Amino acids are important mediators in cancer metabolism, and their kinetics in tumor tissue are far from being understood completely. Mass spectrometry imaging is capable to spatiotemporally trace important endogenous metabolites in biological tissue specimens. In this research, we studied L-[ring-$^{13}C_6$]-labeled phenylalanine and tyrosine kinetics in a human non-small cell lung carcinoma (NSCLC) xenografted mouse model using matrix-assisted laser desorption/ionization Fourier-transform ion cyclotron resonance mass spectrometry imaging (MALDI-FTICR-MSI). We investigated the L-[ring-$^{13}C_6$]-Phenylalanine ($^{13}C_6$-Phe) and L-[ring-$^{13}C_6$]-Tyrosine ($^{13}C_6$-Tyr) kinetics at 10 min (n = 4), 30 min (n = 3), and 60 min (n = 4) after tracer injection and sham-treated group (n = 3) at 10 min in mouse-xenograft lung tumor tissues by MALDI-FTICR-MSI. The dynamic changes in the spatial distributions of 19 out of 20 standard amino acids are observed in the tumor tissue. The highest abundance of $^{13}C_6$-Phe was detected in tumor tissue at 10 min after tracer injection and decreased progressively over time. The overall enrichment of $^{13}C_6$-Tyr showed a delayed temporal trend compared to $^{13}C_6$-Phe in tumor caused by the Phe-to-Tyr conversion process. Specifically, $^{13}C_6$-Phe and $^{13}C_6$-Tyr showed higher abundances in viable tumor regions compared to non-viable regions. We demonstrated the spatiotemporal intra-tumoral distribution of the essential aromatic amino acid $^{13}C_6$-Phe and its de-novo synthesized metabolite $^{13}C_6$-Tyr by MALDI-FTICR-MSI. Our results explore for the first time local phenylalanine metabolism in the context of cancer tissue morphology. This opens a new way to understand amino acid metabolism within the tumor and its microenvironment.

Introduction

Cancer cells are known to exhibit unusual metabolic activity to sustain their proliferation [456]. A well-known example is the non-essential amino acid glutamine, which is associated with neoplastic proliferation [457]. It is also known that phenylalanine consumption correlates with the growth of tumor cell lines and negative patient outcomes [458-467]. Plasma phenylalanine concentrations are elevated in patients with cancer [467]. Phenylalanine is an indispensable amino acid and phenylalanine flux in the body is entirely derived from the diet and cellular protein turnover. It is also needed to synthesize the amino acid tyrosine (Tyr) by the phenylalanine hydroxylase enzyme mainly in the liver and kidney [468]. Isotopically labeled phenylalanine has been used in tracer studies as a measure of protein synthesis [469, 470] and liver function [81, 471]. Phenylalanine metabolism, however, in relation to the morphology of cancer tissue has not been explored yet.

The molecular and cellular heterogeneity in a tumor plays a crucial role in cancer treatment efficacy and outcome [472, 473]. Current strategies to personalize treatment response use genomics data [474] which is not able to reflect the dynamics of metabolic processes in the context of the spatial intratumor heterogeneity. Mass spectrometry imaging (MSI) enables the in situ visualization of metabolites in biological tissue specimens. Adding isotopically labeled versions of target compounds allows the quantitative study of spatiotemporal metabolic dynamics in these tissues [81]. Multi-isotope imaging mass spectrometry (MIMS) has been applied to study the heterogeneity of glucose and glutamine utilization in murine tumors recently [475]. However, matrix-assisted laser desorption/ionization (MALDI), a softer ionization technique without suffering from extensive fragmentation and complexity of interpretation of mass spectra, is increasingly applied in biomedical research [18]. We have recently used this method to track the hepatocellular incorporation of L-[ring-$^{13}C_6$]-Phenylalanine ($^{13}C_6$-Phe) and its metabolite L-[ring-$^{13}C_6$]-Tyrosine ($^{13}C_6$-Tyr) [81].

In this study, we used our previously developed MALDI-MSI method of $^{13}C_6$-Phe [81] to construct spatial and dynamic metabolic flux maps in relation with spatial tumor heterogeneity in a human non-small cell lung carcinoma xenograft model.

Materials and methods

Animal experiments

A total of 14 adult female immune-compromised Crl:NU-Foxn1nu nu/nu nude mice (Charles River, Den Bosch, The Netherlands) were used. Human NCI-H460 non-small cell lung carcinoma (NSCLC) cells suspended in matrigel (BD Biosciences, Breda, The Netherlands) were injected subcutaneously into the flank region of each mouse. Tumor volume was monitored 3 times per week using a Vernier caliper. All animals had unrestricted access to food and water before injection. They received a regular chow diet, which contains 12% fat, 27% protein, and 61% carbohydrate based on calories. Eleven mice were injected with $^{13}C_6$-Phe (Cambridge Isotope Laboratories, Andover, MA, USA) at a dose of 1.0 micromole/g

body weight, and 3 additional mice were injected with normal saline into the lateral tail vein when the tumors reached 1000 mm^3. The tracer-infused mice were subsequently sacrificed at 10 min (n = 4), 30 min (n = 3), and 60 min (n = 4) after injection, and sham-treated mice (n = 3) were sacrificed after 10 min. Tumors were rapidly dissected, snap-frozen with liquid nitrogen, and stored at −80 °C until cryo-sectioning. All experimental procedures were approved by the Animal Ethical Committee of the Maastricht University.

Tissue sectioning

Tumor tissues were sectioned at 10 μm using a cryotome (Leica, Rijswijk, The Netherlands) at −20 °C, thaw-mounted onto indium−tin oxide coated glass slides (CG-40IN-S115, Delta Technologies, Loveland, CO, USA), and stored at −80 °C until further measurement.

On-tissue derivatization and matrix application

P-N,N,N-trimethylamonioanilyl N-hydroxysuccinimidylcarbamate iodide (TAHS) on-tissue derivatization was applied to tissue sections prior to matrix application as described by Arts *et al.* [81] with slight modifications: fresh frozen tissue sections were dried in a vacuum desiccator for 15 min. Subsequently, a TAHS solution of 1.25 mg/mL in acetonitrile was sprayed onto the sections using an automated, temperature-controlled spraying system (TM-sprayer, HTX Technologies, Chapel Hill, NC, USA). Six layers were sprayed at 55 °C with a constant flow rate of 0.1 mL/min and at a speed of 1200 mm/min. Next, all tumor sections were incubated at 55 °C in a humid environment (methanol to water = 1:1, v/v) for 24 h.

A 30 mg/mL 2,5-dihydroxybenzoic acid (DHB, Sigma-Aldrich, St. Louis, MO, USA) matrix solution in methanol/water (7:3, v/v) containing 0.2% trifluoroacetic acid was applied in six layers with the HTX sprayer at 85 °C with a fixed flow rate of 0.1 mL/min, followed by immediate mass spectrometry imaging measurements.

Mass spectrometry imaging experiments

High mass resolution (R = 1.5E^5 at *m/z* 200) matrix-assisted laser desorption/ionization Fourier-transform ion cyclotron resonance mass spectrometry imaging (MALDI-FTICR-MSI) experiments were performed with a Solarix 9.4 T (Bruker Daltonics, Bremen, Germany). MSI data were acquired within a mass range of *m/z* 100–1200 (1E$_6$ data points) in positive ionization mode and in magnitude mode with a 75-μm spatial raster width. The laser operated at a laser power of 18% and a frequency of 2000 Hz with 50 shots accumulated per pixel. Data acquisition was controlled using ftmsControl and FlexImaging 4.1 (Bruker Daltonik, Bremen, Germany).

LC-MS and GC-C-IRMS measurements

The enrichment of free amino acids ($^{13}C_6$-Phe and $^{13}C_6$-Tyr) and protein-bound $^{13}C_6$-Phe were measured in tumor tissue homogenates with liquid chromatography–mass spectrometry (LC-MS) [476] and gas chromatography combustion isotope ratio mass spectrometry (GC-C-

IRMS) [477] using the same protocols as described by Van *et al.* and Arts *et al.*, respectively to complement and validate the MSI data.

Histological staining

After MSI measurement, all tissue sections were washed with 70% ethanol for 30 s to remove the matrix prior to hematoxylin and eosin staining (H&E). The samples were rehydrated in MilliQ water, followed by 3 min in hematoxylin (Merck, Darmstadt, Germany), 1 min in distilled water, and 30 s in eosin (Merck, Darmstadt, Germany). Then, all sections were dehydrated in a graded ethanol series and followed by clearance for 2 min in xylene. Coverslips were mounted onto the slides with Entellan mounting medium (Merck, Darmstadt, Germany), and all sections were air-dried overnight at room temperature. The H&E stained slides were scanned using a digital slide scanner (Mirax Desk, Zeiss, Jena, Germany) and a pathologist annotated viable tumor and non-viable tumor regions digitally in the scanned images. Next, the digitalized H&E images were manually co-registered to the MSI data using FlexImaging 4.1 (Bruker Daltonics, Bremen, Germany).

Data analysis

The tracer-to-tracee ratio (TTR) and the molar percentage excess (MPE) values of $^{13}C_6$-Phe and $^{13}C_6$-Tyr, and ratios of MPE (Tyr) to MPE (Phe) were calculated for every pixel individually using a custom MATLAB script (MATLAB R2014b, Mathworks, Natick, MA, USA) as described by Arts *et al.* [81]. This resulted in tabular ASCII files that can be imported for heatmap reconstructions in FlexImaging 4.1 (Bruker Daltonics, Bremen, Germany).

In parallel, all MSI data, their co-registered H&E images combined with the tumor annotations, were imported to SCiLS Lab 2020a (Bruker Daltonics). There, the peak interval width was set to 5 mDa and each pixel was normalized to its root mean square value. The average intensity ("maximum mean value") data of annotated regions were exported.

Metabolite identification

The human metabolome database (www.hmdb.ca) was used for assignment of identities to *m/z* values with a maximum mass tolerance of 2 ppm. Underivatized molecules were identified assuming single protonation (M = *m/z* - H$^+$), while derivatized molecules ([M + TAHS]$^+$) were identified based on subtracting the monoisotopic mass value of TAHS to obtain the neutral molecular weight (M = *m/z* - 177.1022394).

Results

We performed MALDI-FTICR-MSI analysis of mouse-xenograft lung tumor tissues 10 min (n = 4), 30 min (n = 3), and 60 min (n = 4) after tracer injection and after 10 min in a sham group (n = 3) to study $^{13}C_6$-Phe and $^{13}C_6$-Tyr kinetics (Figure 5.1).
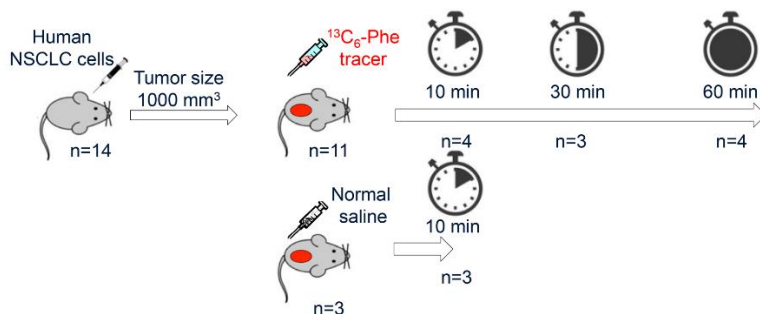
Figure 5.1. Eleven mice were injected with ring-$^{13}C_6$-Phe and three additional mice were injected with normal saline into the lateral tail vein when the tumors reached $1000 \, mm^3$. The tracer-infused mice were subsequently sacrificed at 10 min (n = 4), 30 min (n = 3), and 60 min (n = 4) after injection, and sham-treated mice were sacrificed after 10 min.

Standard amino acids

Nineteen out of 20 standard amino acids were detected in all tumor sections and $^{13}C_6$-Phe and $^{13}C_6$-Tyr were exclusively detected in tracer-injected mice samples. MSI images of labeled and unlabeled amino acids in a representative tumor tissue at 30 min after $^{13}C_6$-Phe injection are shown in Figure 5.2. All amino acids exhibit heterogeneous distributions, which correlate with the different morphological components of the tumor (mainly viable tumor and non-viable tumor). Most of unlabeled amino acids as well as $^{13}C_6$-Phe and $^{13}C_6$-Tyr showed similar spatial distributions with a higher abundance in viable tumor compared to the non-viable regions in the core of the tumor.
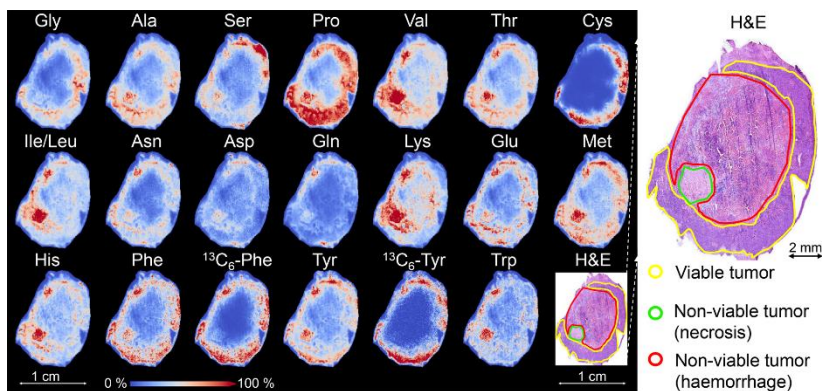
Figure 5.2. Distributions of 19 detected standard amino acids in a representative mouse-xenograft lung tumor tissue at 30 min after $^{13}C_6$-Phe injection. All pixels were normalized to their root mean square value. The co-registered, hematoxylin and eosin stained (H&E) image shows the different histomorphological components of the tissue: viable tumor (yellow), non-viable tumor fraction (necrosis, green), and non-viable tumor region (hemorrhage, red).

$^{13}C_6$-labeled Phe and Tyr

TTR and MPE values were used to assess the spatial enrichment of both $^{13}C_6$-Phe and $^{13}C_6$-Tyr in the tumor samples. The visualizations of TTR (Phe) and TTR (Tyr) across all tumor

sections are shown in Figure 5.3a and c, respectively. A differentiated quantitative analysis of TTR (Phe) and TTR (Tyr) in the annotated viable tumor and non-viable tumor fractions at every time point are shown in Figure 5.3b and d, respectively. MPE (Phe), MPE (Tyr), ratio of MPE (Tyr) to MPE (Phe) in representative tumor tissues at 10, 30, and 60 min after tracer injection and at 10 min of control group are shown in Figure 5.4. MPE values of Phe and Tyr in plasma samples from the same mice over the same time course were measured by GC-C-IRMS and are shown in Supplementary Figure 5.1.
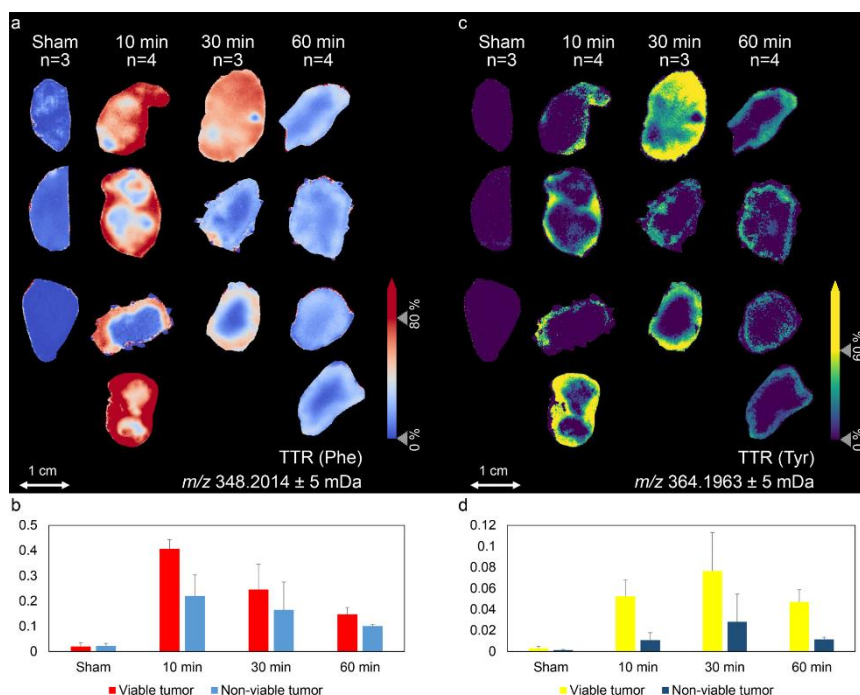
Figure 5.3. Distributions of $^{13}C_6$-Phe (a) and $^{13}C_6$-Tyr (c) in mouse-xenograft lung tumor tissues (n_{total} = 11) at 10, 30, and 60 min after tracer injection and at 10 min of control group (n = 3). Tracer-to-tracee (TTR) images for phenylalanine (a) and tyrosine (c) were calculated by normalizing the labeled amino acid signals to the intensities of their respective unlabeled versions. TTR values of Phe (b) and Tyr (d) were then differentiated annotated viable tumor and non-viable tumor regions for every time point.

The highest enrichment for $^{13}C_6$-Phe was detected at 10 min after bolus injection followed by a decreasing trend over time. The overall enrichment of $^{13}C_6$-Tyr was substantially lower than $^{13}C_6$-Phe, and it had a delayed temporal trend compared with $^{13}C_6$-Phe with its peak at 30 min. Additional experiments on plasma of the same mice show that both, $^{13}C_6$-Phe and $^{13}C_6$-Tyr, reached their highest level at 10 min after bolus injection followed by a decreasing trend over time (Supplementary Figure 5.1).

The MSI enrichments of $^{13}C_6$-Phe and $^{13}C_6$-Tyr were further complemented by LC-MS data acquired from homogenized tumor tissues, which showed a similar trend over time as the spatially convolved MSI data (Figure 5.5a and b). Furthermore, the incorporation of $^{13}C_6$-Phe

into proteins in tumor tissue homogenates was investigated with GC-C-IRMS. The highest protein bounded $^{13}C_6$-Phe was detected at 30 min and decreasing over time (Figure 5.5c).
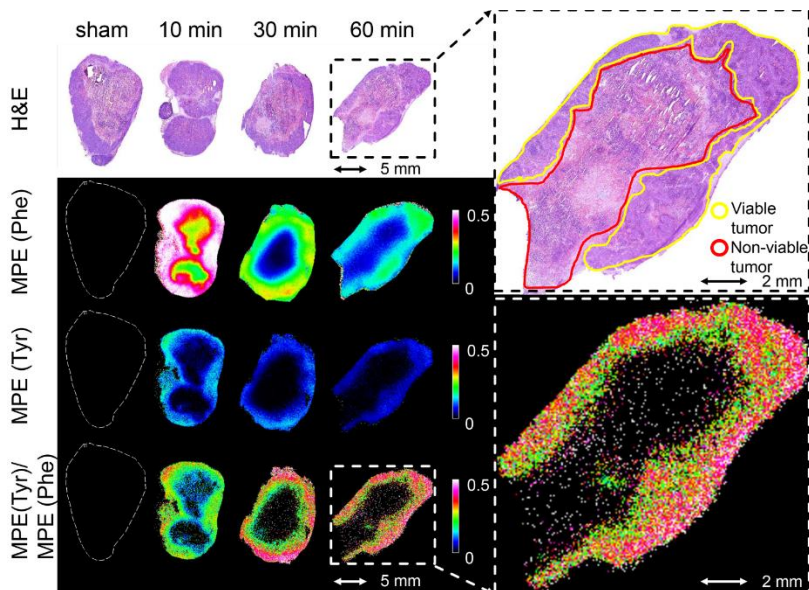
Figure 5.4. Visualizations of the molar percentage excess (MPE) for $^{13}C_6$-Phe and $^{13}C_6$-Tyr and the ratio of MPE (Tyr) to MPE (Phe) in representative tumor tissues at 10, 30, and 60 min after tracer injection and at 10 min of sham group. Their co-registered, hematoxylin and eosin stained (H&E) images are shown on the top. A magnification of the ratio of MPE (Tyr) to MPE (Phe) in one representative tissue section at 60 min and its co-registered H&E image is shown on the right.
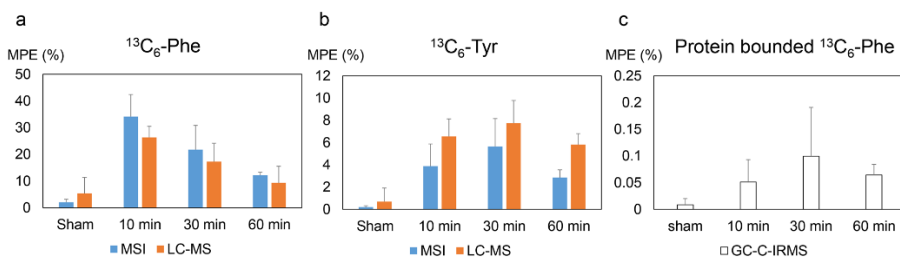
Figure 5.5. Overall enrichment of tissue free $^{13}C_6$-Phe (a) and $^{13}C_6$-Tyr (b) by MSI (blue) and LC-MS (orange), and $^{13}C_6$-Phe protein enrichments (c) in homogenized tumor tissues by GC-C-IRMS. Enrichment is shown as mean MPE $\pm$ SE (%)

Discussion

In this study, we used MALDI-FTICR mass spectrometry imaging (MSI) to study $^{13}C_6$-Phe and $^{13}C_6$-Tyr kinetics in mouse-xenograft lung tumor tissues at four different time points after injection. The use of MSI allowed us to detect all unlabeled and labeled amino acids simultaneously.

All observed amino acids exhibit heterogeneous distributions, which correlate with the different morphological components of the tumor (Figure 5.2). For example, branched-chain amino acids (leucine, isoleucine, and valine) are most pronounced in the necrotic region, and all amino acids are much less abundant in the hemorrhagic region. This indicates the necessity to investigate amino acid kinetics in a spatially differentiated fashion using imaging technologies.

Looking at the labeled amino acids of interest, $^{13}C_6$-Phe and $^{13}C_6$-Tyr were found exclusively localized in the viable tumor region in contrast to their non-labeled equivalents, which are additionally present in necrotic regions.

When calculating the TTR and MPE values for both labeled amino acids for viable and non-viable tumor regions, the highest enrichments for $^{13}C_6$-Phe and $^{13}C_6$-Tyr were detected at 10 min and at 30 min after bolus injection, respectively, followed by a decreasing trend over time. Additional experiments on plasma of the same mice show that both, $^{13}C_6$-Phe and $^{13}C_6$-Tyr, reached their highest level at 10 min after bolus injection followed by a decreasing trend over time (Supplementary Figure 5.1). This together with the observation that the highest enrichment for $^{13}C_6$-Tyr in the tumor was delayed indicates that $^{13}C_6$-Tyr was subsequently transported to the tumor tissue after a Phe-to-Tyr conversion process, which is assumed to predominantly occur in the liver [468]. Moreover, viable and non-viable tumor fractions showed similar enrichment trends over time, but the viable tumor exhibited greater enrichment of both labeled amino acids than non-viable tumor at every time point (Figure 5.3). This might be related to the higher metabolic activity of viable tumor cells and their higher perfusion over non-viable tumor tissue. Interestingly, the ratio of MPE (Tyr) to MPE (Phe), representing the Phe-to-Tyr turnover (in the tumor or elsewhere in the organism) was significantly higher in the outer rim of the viable tumor region (Figure 5.4). This is a reflection of the intra-tumor heterogeneity within the viable tumor fraction, which might be attributed to spatial variation in perfusion, vascularization, cell growth, viability, or differences in metabolic activity [478].

These MSI enrichments of $^{13}C_6$-Phe and $^{13}C_6$-Tyr were further complemented by LC-MS and GC-C-IRMS data acquired from homogenized tumor tissues. The LC-MS data showed a similar trend over time as the spatially convolved MSI data, and thereby validated the accuracy of the MSI approach (Figure 5.5a and b). Interestingly, the GC-C-IRMS data indicated a delayed incorporation of $^{13}C_6$-Phe in the tumor protein synthesis as compared to the unbound labeled amino acids (Figure 5.5), which might correlate with a lower clearance rate of $^{13}C_6$-Phe in the tumor as compared to the liver where both $^{13}C_6$-Phe and $^{13}C_6$-Tyr were already cleared at 30 min and 60 min post-inoculation [81]. MALDI-MSI showed that clearance of both amino acids in the tumor was delayed compared to the liver, consequently delaying the incorporation of $^{13}C_6$-Phe into the proteins synthetized in the tumor (Figure 5.5c). Based on this, we can hypothesize that the incorporation of $^{13}C_6$-Phe in the tumor protein synthesis presents a different kinetic compared to the liver progressive incorporation from 10

to 60 min. Nevertheless, while the liver tissue is fully viable and reasonably homogeneous, the heterogeneous tumor tissues were composed of both viable and non-viable parts. Only the viable tumor cells contribute to metabolic activities and so to protein synthesis in the tumor. Therefore, as the tumor tissue homogenates do not benefit from an estimation of the proportion of viable and non-viable parts, the protein incorporation results from homogenates should be interpreted with caution.

This again underlines the necessity to study kinetics in a spatially resolved manner. In that sense, this study demonstrates the usefulness of MSI to investigate spatial $^{13}C_6$-Phe and $^{13}C_6$-Tyr kinetics in tumor and also reflects inter-organ amino acid shifts. The translation to human samples will offer new insights in diagnostic molecular markers and tumor treatment.

Conclusions

In this work, we demonstrated for the first time the spatiotemporal intra-tumoral distribution of the aromatic amino acid L-phenylalanine and its derivative L-tyrosine by MSI in tumor tissue. Furthermore, we showed the distribution of these molecular targets in relation to the tumor morphology, allowing us to monitor altered local amino acid metabolism in tumor cells and their microenvironment. Our approach can enhance our understanding on inter-organ amino acid metabolism and provide further insights to improve and develop novel strategies for cancer therapy.

Chapter 6

Impact

In this thesis, MALDI mass spectrometry imaging (MSI) has been applied to study the local metabolism of atherosclerosis, abdominal fascia healing, and non-small cell lung carcinoma in several different animal models. It is important to realize not only the underlying scientific impact, but also other non-academic benefits such as societal and economic relevance, arising from this scientific research. In the following sections, I will briefly discuss aspects of the impact of the studies described in this thesis.

Scientific impact

In **chapter 2**, I systematically investigated lipids in atherosclerotic plaques formed in the two most widely used atherosclerotic mouse models using MALDI-MSI. Since the differences between these two models are poorly understood and well-standardized comparative studies are scarce, the systemic characterization of atherosclerotic lipids in these two models could have a significant impact on preclinical atherosclerosis research. Fellow researchers and research firms can benefit from this published work for selecting mouse models for their future atherosclerotic studies. Moreover, one aorta root was imaged comprehensively by 3D-MALDI-MSI to investigate the volumetric distribution of the plaque-specific lipids along the plaque's length. Expanding 2D-MSI to a three-dimensional rendered volume enables a closer representation of the native 3D biological structure and yields new insights of the molecular complexity and heterogeneity of biological systems, and thereby demonstrates its potential value for clinical 3D imaging application.

Following the same line, in **chapter 3**, I combined non-targeted MALDI-MSI metabolomics of mouse aortic tissue with targeted metabolomics of human plasma using SRM-LC-MS/MS. Combining the plasma, which represents the systemic state of the organism with the local metabolism of the disease, offers a more comprehensive, holistic strategy to understand atherosclerosis mechanisms. Moreover, this novel integration workflow not only strengthens MALDI-MSI as a discovery tool but also widely complements the mechanistic study already performed by MSI towards a novel tool for diagnosis, because clinicians routinely assess an individual's overall health status by measuring certain metabolites in biofluids. Additionally, the investigation of the individual's metabolic conditions in both tissue and plasma has a profound effect upon precision or personalized medical initiatives.

In **chapter 4**, the local lipids alterations of fascial healing revealed by MSI were correlated to histologically (H&E) scored changes captured by microscopic imaging. This correlative study required a close cooperation among surgeons, MSI researchers, and pathologists, leading to a better understanding of molecular and cellular changes during acute fascia healing, as well as novel therapeutic targets that allow prevention or treatment of incisional hernias.

In the last chapter of this thesis (**chapter 5**), using stable isotope (^{13}C) labeling and MALDI-MSI revealed the spatiotemporal intra-tumoral distribution of the essential aromatic amino acid phenylalanine and its de novo synthesized metabolite tyrosine. It is important to mention

that this study is based on a previous study [81] where the same mice were used but which focused on the liver. Moreover, the plasma data from the same mice provided the additional value of inter-organ metabolism ($^{13}C_6$-Tyrosine was subsequently transported to the tumor tissue after a hepatic Phe-to-Tyr conversion). **Chapter 5** hence gives evidence for the potential of studies that involve different organs together with plasma from the same individual to not only obtain a better understanding of the systemic nature of diseases, but also for improving animal welfare by achieving the highest research value by using as much material from a subject as possible. It is important to mention the widespread international 3R-concept (Replacement, Reduction, Refinement) for studies involving the use of animals [479] which aims at minimizing the number of animals while maximizing animal welfare and quality of research. Therefore, the preclinical studies conducted in the current thesis point out the noteworthiness to give a more comprehensive and valuable answer to a scientific question with a limited number of animals.

Socio-economic relevance

My PhD research projects mainly focused on atherosclerosis, cancer and wound healing. Among them, atherosclerosis and cancer are the two main dominant causes of deaths all over the world [480]. Patients with atherosclerosis and cancer are strongly affected both physically and mentally. Along with illnesses, patients and their families, caregivers and the social security system are also suffering economically from long-standing treatment expenses. Also wound healing and its care constitute another major source of total healthcare budget [481]. There are many health consequences of failed wound healing, such as infection, septicaemia, osteomyelitis, chronic morbidity or even mortality [482]. Moreover, there is a pronounced demand for wound care products in the wound-dressing markets.

Metabolomics-based preclinical studies on these diseases in this thesis could point to potential new treatments, which might merit further translational studies in humans, as well as greatly save the screening time and funding needed in clinical trials. Moreover, it might indirectly alleviate economic burden for patients and society, as well as improve quality of life for patients in the long run. For instance, in **chapter 2**, several specific lysolipids were found exclusively localized in the atherosclerotic aorta plaque. Diagnostics could benefit from this study for targeting these lipids using nuclear medicine and molecular contrast agents. Likewise, the metabolic alterations induced by high cholesterol and high fat diet observed in the **chapter 3** could inspire fitness enthusiasts, nutritionists, food industry and medical doctors. For example, a healthy diet plan with less cholesterol and fat could be strongly recommended for fitness enthusiasts, clients of nutritionists, as well as patients and their caregivers. Additionally, food manufacturers and marketers could provide healthier food products for public health and help customers make health choices. In similar fashion, the findings from **chapter 4** might bring a big value for wound-dressing markets. Similarly, the amino acids metabolism research in **chapter 5** might have a great impact for targeted delivery of therapeutics in cancer.

More broadly speaking, the strategies developed in this thesis could also be applied to other health conditions such as current coronavirus disease 19. Coronavirus patients show varying levels of severity in lung tissues and MSI-based local metabolomics could be used to identify specific metabolic signatures, and thus predict the consequence of the disease with a higher level of certainty. A subsequent successful application of potential metabolomics-based markers could dramatically reduce the test cost (e.g. point-of-care testing) and assist clinicians in prognosis evaluation. Likewise, similar approaches could also apply to other different settings or fields. For example, toxicology, which shows great interest for many pharmaceutical companies, MSI could aid in assessing the metabolic effects of potential drug candidates before clinical trials. In addition, the metabolomics-based strategies can also be used for examination of phenotypic changes in genetically modified products for public consumption in agriculture and food field. Moreover, it might also confer a powerful tool to investigate metabolomics alterations induced by global issues such as environmental pollution, and mental health problems.

Lastly, across my PhD projects, I mainly worked with MALDI-MSI instruments from Bruker Daltonics (Bremen, Germany). In the meantime, I was also responsible for the maintenance of one of Bruker Daltonics' flagship MALDI-MSI instruments (rapiflex) in the lab. Thus I had the privilege of working with Bruker Daltonics for trouble shooting, as well as giving feedbacks to Bruker Daltonics in order to improve their instrumental performance. This extraordinary experience allowed me to improve my knowledge and insight from both a scientific researcher's perspective as well as from a commercial viewpoint.

Chapter 7

General discussion & Outlook

Over the last decade, MALDI-MSI has been the most widely applied MSI modality for the untargeted molecular imaging of endogenous and exogenous molecules such as proteins, peptides, glycans, metabolites and drugs in biomedical research. It is a valuable and powerful tool for the investigation of molecular processes underlying diseases on a spatial level. The work in this thesis demonstrated how MALDI-MSI can be applied to in situ metabolomics studies in several different preclinical disease models of atherosclerosis, cancer and wound healing. However, MALDI-MSI on a metabolomics level also faces multiple challenges that need overcome to fully exploit its potential in future studies.

7.1 Challenges and opportunities in sample preparation

Tissue preservation

Fresh frozen samples are typically used for metabolite studies [65], which is also true for all of the studies in this thesis. However, most of the collected tissue samples by researchers and clinicians around the world is archived as formalin-fixed and paraffin embedded (FFPE) material for its long-term preservation and histological examination [65, 483]. Buck *et al*. have recently shown that a large fraction of the metabolites in FFPE tissues are chemically and spatially conserved and are suitable for MSI analysis [483]. Consequently, MALDI-MSI metabolomics studies using FFPE tissues are currently on a rising trend [484, 485]. In parallel, new preservation compounds are being developed that bridge the necessities in biomedical research with established clinical workflows. Such an example is PaxGene, which has already been used in MSI studies for the investigation of proteins, peptides and metabolites [486] and shows good compatibility with the requirements from clinical practice [487]. The further investigation of such alternatives for tissue preservation also carries huge potential for the broadness and depth of molecular information that can be extracted from preserved tissues using MSI.

Derivatization of metabolites

However, irrespective of the tissue preservation, the detectability of some metabolites still presents a challenge due to their low ionization efficiency, the level of background interferences caused by the MALDI matrix, the lack of chromatographic separation, and resulting ion suppression effects, combined with low abundances of these metabolites [488]. To increase ionization efficiency of molecules, derivatization can be used [489]. Therefore, in **chapter 5**, I used on-tissue TAHS derivatization for improving the ionization efficiency of the target amino acids in the mouse tumor samples [490]. The specificity for detecting targeted amino acids in MALDI-MSI has been dramatically improved by on-tissue TAHS derivatization. However, for optimal on-tissue TAHS derivatization and to prevent side-reactions of TAHS with the hydroxyl group attached to the phenol group of Tyr, samples have to be incubated at 55 °C for 24 hours in a humid environment [491]. The whole process is time-consuming, and it is limited to temperature-insensitive molecules and tissues. For example, I could not apply on-tissue TAHS derivatization to OCT embedded aortic tissues in **chapter 3** since OCT can melt at higher temperatures, leading to the contamination of the

tissue. Moreover, slight delocalizations can be observed at a higher spatial resolution, such as 25 μm [491]. Thus, the chosen derivatization method should be compatible with the scale of achievable MSI spatial resolution and type of embedding [221]. Furthermore, the development of effective matrices for MALDI but with reduced matrix background, as well as better derivatization strategies that are less time-consuming and compatible with high spatial resolution MSI are highly required. This can increase the throughput especially for previously undetectable compounds or molecules not yet investigated by MSI and will allow obtaining valuable molecular profiles from single cells.

3-dimensional mass spectrometry imaging

To date, most of the MALDI-MSI studies are performed at the 2D level. It has pushed its frontiers to three spatial dimensions in the past decade for investigating the volumetric distribution of molecules across the sample structure [103, 492]. In **chapter 2**, 3D-MALDI-MSI was used to verify the volumetric distribution of plaque-specific lipids in an aortic root of one $apoe^{-/-}$ mouse to confirm the general presence of these lipids along the plaque. This 3D-MSI analysis shows that the lipids' spatial specificity remains stable along the z-direction of the plaque and is independent of the blood flow direction. While 3D-MSI is able to provide additional contextual information on the molecular distributions in the biological tissue [103], it is important to note that the sample preparation for 3D-MSI faces more challenges compared to 2D-MSI. Several practical considerations need to be highlighted for a successful 3D-MSI study, especially for tiny tissues such as mouse aorta encountered in **chapter 2**. These crucial aspects include careful sectioning to maintain the sample's integrity and consistency in the sample's spatial orientation, fully randomizing the sections and samples across the different slides and within the same slide, as well as carefully and gently performing the staining for all sections since every section is unique and therefore not replaceable. In addition to sample preparation, 3D-MSI data processing and analysis remains challenging, as recently reviewed by Vos *et al.* [103]. This includes image registration, volumetric reconstruction, the application of stereologic approaches, 3-dimensional annotation, and spatial statistics. With respect to the first, overlaying 3D-MSI data with other 3D imaging techniques such as magnetic resonance imaging will lead to new challenges in the biomedical field in the future but also carries huge potential as recently reviewed by Maynard and Hart for pharmaceutical studies [493].

7.2 Stable isotope labeling in MALDI-MSI to trace metabolic changes

While MALDI-MSI dramatically increases the specificity of metabolites detection [221], it is, due to its invasiveness, limited to providing a single and static snapshot of highly dynamic systems in which molecules are constantly synthesized and consumed [81]. Using stable isotope labeling of compounds such as lipids [123, 494], amino acids [490, 491, 495] and glucose [496, 497] in MALDI-MSI combined with longitudinal animal studies allows tracing metabolic processes in which the labeled molecules are involved in a time-resolved manner. This is achieved by detecting the mass-shifted signals containing the isotopic tracer or the

products of its metabolic conversion, and thus adds an extra dimension to the understanding of both normal metabolic processes and pathological processes [221]. MALDI-MSI has been used to map the uptake and metabolism of stable isotope labeled nutrients and other compounds in endophytic bacterium [495], radish plants [498], cultured hippocampal neurons [499], mouse lungs [494], mouse spleen [500], mouse liver [491], mouse brain [497, 501], non-small cell lung carcinoma in mice [490], atherosclerotic mouse aorta [123], acute myocardial ischaemic mouse heart [497], and normal bovine lenses [496].

In **chapter 5**, I studied L-[ring-$^{13}C_6$]-labeled phenylalanine and tyrosine kinetics in a human non-small cell lung carcinoma xenografted mouse model using MALDI-FTICR-MSI. This approach also harbors huge potential for my work on atherosclerosis, which is reported in **chapters 2** and **3**. In continuation of the results reported in **chapter 2**, I investigated the presence and detectability of the discovered plaque-specific lipids in mice plasma using regular MALDI-MS profiling. Interestingly, despite the complexity of plasma samples, most of plaque-specific lipids were detectable in both normal diet and high-fat diet *ldlr*$^{-/-}$ mice plasma without further chromatographic separation or purification of the samples, thereby suggesting their potential as atherosclerotic markers in a minimally-invasive fluid. For the measurement, 0.5µL plasma from every mouse was spotted on a conductive glass slide and later the matrix norharmane was applied by sublimation. However, the quantification and thereby the validation these plaque-specific lipids in plasma failed due a strong "coffee-ring" effect, which led to a bad reproducibility. This can be seen in Figure 7.1 which shows the plasma-matrix spots belonging to representative 4 plaque-specific *m/z* species as measured by MALDI-TOF-MSI in negative ionization mode in 8-week high-fat-diet (HFD) *ldlr*$^{-/-}$ mice (n=14), 16-week HFD *ldlr*$^{-/-}$ mice (n=12), and 16-week chow-diet (ND) *ldlr*$^{-/-}$ mice (n=14). While the results suffer from a huge variation, their detectability still makes an interesting link between highly abundant blood circulating lipids and plaque-specific lipids, which should be further pursued. For instance, it would be very interesting to incorporate stable isotope of these plaque-specific lipids into the diet of the mice, and trace these molecules from their ingestion over their travel through the blood stream to the incorporation into the atheroma. It has to be noted that the similar approach has already been successfully applied by Castro-Perez *et al.* to investigate the incorporation of an orally dosed (2,2,3,4,4,6-d6)-cholesterol over 3 weeks into atherosclerotic aorta plaques in a apolipoprotein E-knock-out mouse model [223]. It showed dietary d6-free cholesterol is heterogeneously distributed within the plaque while the relative intensity is much lower compared to the unlabeled free cholesterol [223]. This work demonstrated the possibility to spatially trace isotopically labeled lipids with MALDI-MSI to characterize dietary lipid accumulation and localization within the atheroma. As I observed in **chapter 2**, not only cholesterol, but also certain lysolipids and sphingomyelins are integral constituents of the plaque in atherosclerosis. Tracing these by the labeled approach would be very interesting as well as other plaque-specific lipids besides cholesterol, such as lysophospholipids, which have also been reported by other MSI studies [223, 336, 502]. This will enable a better understanding of the

pathogenesis of atherosclerotic plaque and a novel strategy for management of cardiovascular diseases.
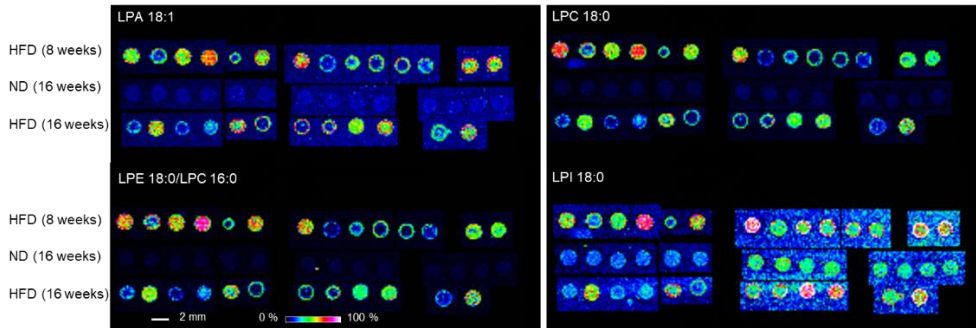
Figure 7.1. Visualization of representative four *m/z* species in spotted plasma of 8-week HFD *ldlr*$^{-/-}$ mice (n=14), 16-week HFD *ldlr*$^{-/-}$ mice (n=12) and 16-week ND *ldlr*$^{-/-}$ mice (n=14) by MALDI-TOF-MSI in negative ionization mode. These 4 *m/z* species correspond to plaque specific lipids that I have previously identified in **chapter 2**.

In the light of tracing the dynamics of targeted endogenous molecules, the isotope labeling together with MALDI-MSI could also be extended to other different diseases (e.g. neurological disorders and cardiovascular conditions) and in different living biological systems ranging from human and animals to cultured cells or organoids. For instance, imbalances in the levels of tryptophan and its metabolites (e.g. kynurenines) have been implicated in Alzheimer's disease, cancer, malaria and neoplasia among many others [503]. Consequently, isotope labeling of tryptophan together with MALDI-MSI could be applied to study *in situ* metabolism of tryptophan in the aforementioned diseases. Likewise, labeling of carboxyl-containing metabolites such as bile acids [504] and fatty acids [505] or their precursors could be used to investigate metabolic disorders including chronic kidney disease among others [506]. The presented approach could also be employed in a healthy biological system to spatially map general metabolic processes such as citrate cycle, nucleotide metabolism, and glycan biosynthesis and metabolism on a microscopic level, which has so far never been done in a systematic fashion.

Furthermore, with recent developments addressing some instrument-related limitations in MALDI-MSI will broaden the applications of stable isotopes in MALDI imaging [221]. One example is, MALDI-2 [507], a post-ionization technique that utilizes a second tunable wavelength laser to initiate a secondary ionization process in the desorbed gas plume caused by the original MALDI laser. It has been shown that this can significantly improve the sensitivity and ionization efficiency of numerous classes of molecules including drugs and lipids [221, 508]. Moreover, trapped ion mobility spectrometry (TIMS) [509] is a high-performance gas phase separation technique that has also been recently incorporated into MALDI-MSI instruments. This additional layer of separation for molecules according to their cross-section area has the potential to overcome the challenges of molecular complexity associated with tissue imaging and assisting with molecular identification at a rate compatible

with the acquisition rate of imaging experiments [509]. This approach could be extremely powerful for isotope labeling in MALDI-MSI studies due to separate the label from an isobaric and therefore confounding compound.

7.3 Local and systemic metabolomics

Systemic nature of diseases

In all studies reported of my thesis, I studied the local metabolism of diseases by mainly focusing on one primarily affected organ (aorta, fascia, and tumor) and the metabolites involved in the disease. However, many of these diseases, such as atherosclerosis and cancer, can be considered systemic diseases. Taking atherosclerosis (**chapters 2** and **3**) as an example, several organ systems including the vascular system, the endocrine system, adipose tissue, the liver, the gastrointestinal tract and the kidneys were found to be involved in the pathogenesis of atherosclerosis [510], as reviewed by Ramsey *et al.* [510]. For instance, Kleemann *et al.* illustrated that high doses of dietary cholesterol result in hepatic inflammatory response, which contribute to early atherosclerotic lesion formation [511]. Additionally, renal insufficiency is a recognized risk factor for cardiovascular disease (CVD) [512]. Following the same context, Karlsson *et al.* suggested alteration of the gut metagenome is associated with symptomatic atherosclerosis [513]. Moreover, intestinal microflora metabolism of the dietary lipid phosphatidylcholine (PC) has been linked to predict CVD risk in humans [390]. The dietary PC lipids are metabolized to choline in the small intestine, and then the resulting choline produces trimethylamine (TMA) in the large intestine. TMA later diffuses into the bloodstream and converts into trimethylamine N-oxide (TMAO) in the liver (Figure 7.2) [390]. TMAO has been observed to be strongly related with atherosclerosis [390, 514]. Furthermore, Koeth *et al.* demonstrated intestinal microbiota metabolism of dietary L-carnitine also produces TMAO and promotes atherosclerosis in mice [395]. The link between the gut microbiome, the diet, and cardiovascular diseases has been a hot topic over the past few years [515]. In that line, there are many other metabolites (especially uremic toxin) involved in atherosclerosis [515] and most of them have not been studied with respect to the different involved organs (inter-organ metabolism). Integration of information from different sources and technologies could aid in understanding those systemic diseases and their spatial, inter-organ involvedness.
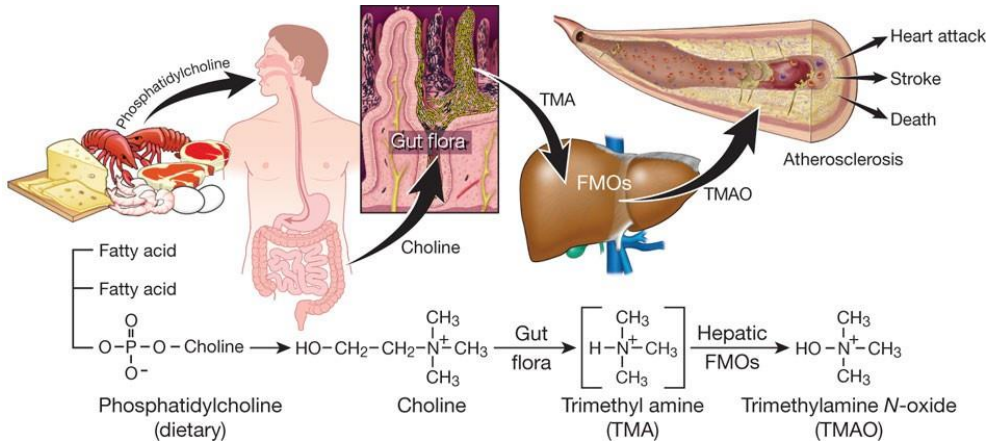
Figure 7.2. Schematic intestinal microflora metabolism of the dietary phosphatidylcholine (PC) linked with atherosclerosis. The dietary lipids PC are metabolized to choline in the small intestine, and then the resulting choline produces trimethylamine (TMA) in the large intestine. TMA later diffuses into the bloodstream and converted into trimethylamine N-oxide (TMAO) in the liver. This image has been reproduced from [516].

Dynamic nature of diseases

Although the underlying cause of a disease is often of a systemic nature, the disease's progression is also dynamic such as atherogenesis (Figure 7.3) as previously described in **chapter 1**. It would be very interesting to extend the studies done in atherosclerosis over time as I have observed already in similar experiments in **chapter 4** (fascia wound healing) and **chapter 5** (tumor). However, MSI is invasive and therefore it is difficult to study dynamic changes over time continuously. *In vivo* imaging techniques are therefore needed to complement the molecular information by MSI in order to be able to capture the different steps in atherogenesis (Figure 7.3a) [517].
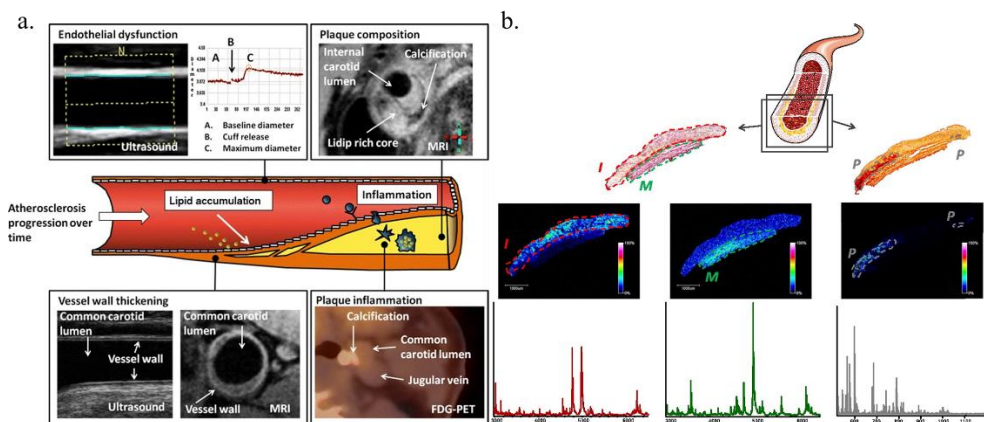
Figure 7.3. Multiple imaging modalities addressing different processes in atherosclerosis (3a). Ultrasound can be used to measure artery endothelial function (3a, upper left) as well as vessel wall thickness (3a, lower left). MRI is able to obtain plaque composition (3a, upper right and lower middle). FDG-PET can evaluate plaque inflammation

(3a, lower right) while CT scan can visualize plaque calcification. Additionally, MSI as an ex vivo imaging technique can be applied to define specific molecular patterns in atherosclerotic tissue (3b, I, M, and P refer to intima, media and plaque, respectively). The figure 3a has been reproduced from [517] and the figure 3b has been reproduced from [242].

Integration of MSI with other imaging modalities

In other fields of research than presented here, it has been shown that MSI can also be integrated with other complementary imaging technologies, such as microscopy [518], Raman spectroscopy, optical molecular imaging (fluorescence imaging and bioluminescence imaging), MRI [519] and Positron emission tomography (PET), to take advantage of the different strengths of the techniques [520]. For example, M. Abdelmoula *et al.* aligned 3D MSI to MRI data non-linearly using a new computational approach [519]. Additionally, the sensitivity of fluorescence was combined with the specificity of MALDI-MSI to investigate the spatial distribution of the anti-angiogenic drug sunitinib (to treat liver cancer) and its metabolites after hepatic transarterial administration *in situ* [329]. MALDI-MSI was also able to corroborate the *in vivo* imaging MRI signals and enabled *in situ* quantification of a collagen-targeted MRI contrast agent (Gadofluorine M) in a mouse model of myocardial infarction [521]. Moreover, MALDI-MSI has also been used for mapping commonly employed PET ligands raclopride (a D2 dopamine antagonist) and SCH 23390 (a D1 dopamine antagonist) in rat brain tissue sections [522]. Even though these are not metabolomics based studies, they still demonstrate enormous potential of *ex vivo* MSI combined with other *in vivo* noninvasive imaging modalities for future *in situ* metabolomics and other omics studies.

For example, ultrasound allows assessing the geometry of vessel walls (thickness) and plaques (size and volume) as well as the risk for rupture of the plaques [523]. Magnetic Resonance Imaging (MRI) can characterize plaque composition (e.g. lipid rich core, fibrosis, calcification, and intraplaque haemorrhage deposits) and define arterial thrombus age [524]. ^{18}F-fluordeoxyglucose positron emission tomography (^{18}F-FDG-PET) is able to track changes in plaque inflammation over time [525]. Therefore, a combination of MSI (Figure 7.3b) with other *in vivo* techniques (Figure 7.3a) is necessary to offer new insights underlying the dynamics of disease progression.

So far, Lohofer and coworkers have used MSI to visualize the localization and quantify the MRI probe Gadofluorine P in plaque tissue *ex vivo* with high spatial resolution and thus adds novel and more target specific information to molecular MR imaging of atherosclerosis [526]. Another example for the integration of MSI data with images from other optical modalities has recently been given by Iskander-Rizk *et al*., who used MALDI-MSI as reference for the less-invasive catheter-based photoacoustic imaging of lipids in human carotid endarterectomy samples [527].

In this context, integration of MSI with other imaging technologies could also be employed in my research in this thesis. For instance, ^{18}F-FDG-PET could be incorporated with 3D-MSI

data in **chapter 2** to provide information on the local inflammation status at a 3D level, which could be correlated with specific lipid compositions of the plaque. Ultrasound can be used for the work presented in **chapter 3** to measure the artery's endothelial function and vessel wall thickness for both control and atherosclerotic mice which might replenish the biological information for correlation with the metabolic alterations observed in aorta by MSI. In addition, fluorescence imaging could be applied to monitor different activities such as inflammation and cellular metabolic state to better determine the actual phase of wound healing in **chapter 4**, which might be valuable to link them with *in situ* lipids changes observed by MSI. In **chapter 5**, MRI could be employed to provide information on the tumor's vascular structure to better understand the heterogeneous distributions of the different amino acids in the tumor.

To sum up, the few aforementioned examples and the many from other research fields show that multimodal imaging will open new doors for numerous biomedical research and pharmaceutical applications and yield important new insights into different biological and pathophysiological processes as well as create new opportunities for disease detection and treatment [528].

Integration of MSI with other omics technologies

As hybrid technology, MSI cannot only be integrated with other imaging modalities but also with data from other molecular omics modalities (DNA mutations, mRNA sequencing and protein abundances). For example, Capolupo *et al.* recently integrated MALDI-MSI lipidomics data with single-cell mRNA sequencing to investigate the metabolic and transcriptional heterogeneity of individual dermal human fibroblasts [529]. Combination of postmortem MALDI-MSI and genetic analysis revealed that very long-chain acyl-CoA dehydrogenase deficiency may have accounted for a case of infant death with liver steatosis [530]. Ščupáková *et al.* correlated lipid features by MALDI-MSI with gene expression data in nonalcoholic fatty liver disease [531]. In another example, Kazdal *et al.* combined MALDI-MSI proteomic analysis with genetic mutations data in a single pulmonary adenocarcinoma tissue section [532]. Xie *et al.* applied MALDI-MSI combined with LC-MS/MS-based metabolomics to investigate an environmental pollutant (Bisphenol S) induced proliferation of 3D breast cancer cell spheroids [533]. Taken together, complementation and integration of MSI features with other omics data permits obtaining a more comprehensive understanding of many diseases as well as identification of new diagnostic and prognostic biomarkers.

Likewise, along with lipidomics and metabolomics, the other omics including genomics, transcriptomics, and proteomics, play crucial roles in unravelling and understanding complex molecular mechanisms in atherosclerosis, cancer, and wound healing, among others. Therefore, integration of multi-omics approaches could also be applied to these fields of research. For instance, different plasma lipid species were found to be regulated by genetic mechanisms in different way in cardiovascular disease [534, 535]. Integrating genomics with

lipidomics could hence potentially identify genetic variants associated with different lipid species (e.g. lysolipids in **chapters 2** and **3**) participating in atherosclerosis. Similarly, a variety of proteins such as lipoproteins are also key players in atherogenesis. Therefore, the combination of proteomics and metabolomics at cellular level could illuminate the related proteome responsible for the metabolome's alteration in atherosclerosis [536]. Unsurprisingly, not just lipids, alteration of gene signatures [537] as well as proteins [538] (e.g. inflammatory mediators, cytokines, among others) have also been observed across the different phases of wound healing. Correspondingly, similar multi-omics approaches could also be used to investigate wound healing in **chapter 4.** Moreover, in cancer research, it is well recognized that genetic [539] and transcription factors [540] hugely influence the cancer's metabolic pathways [541] such as aerobic glycolysis, lipogenesis, amino acid metabolism and tricarboxylic acid cycle. In this regard, integrating genetic or transcriptomic information with metabolomics on a spatial level may open an avenue for a better understanding of cancer metabolism in **chapter 5**.

Spatial omics

An intermediate way to the integration of MSI with *in vivo* imaging or with other non-imaging omics techniques is *spatial omics*. Since, GC-MS and LC-MS offer the broadest coverage of metabolites (often over 10,000 features for untargeted metabolomics) [515], recently MALDI-MSI has been used to guide a laser microdissection system (LMD) to microdissect tissue areas as defined by the MSI data. The dissected material was then submitted to follow-up proteomic analysis by high-performance liquid chromatography-mass spectrometry (HPLC-MS) on the same MS instrument (timsTOF fleX, Bruker Daltonik, Bremen, Germany) [542]. This approach enables broader molecule coverage without losing the spatial molecular information highlighted by MALDI-MSI on the exact same tissue section. The same approach could be applied for the studies (**chapters 2–5**) in this thesis. For example, in **chapter 3**, I observed spatially altered metabolites in the different regions in the aorta tissue. However, the metabolites that I could unambiguously identified were limited, which might relate to the size of the mouse aorta as well as to ion suppression effects both leading to not sufficiently intense signals. Another example is **chapter 5**, where I observed that all detected amino acids exhibited heterogeneous distributions in the tumor. Therefore, MSI could provide the spatial segmentation maps to highlight these distinct areas for a subsequent dissection by the LMD for follow-up untargeted or targeted extract-based metabolomics or other types of omics analysis.

To conclude, I envision that MSI together with other different imaging modalities and other non-imaging omics technologies is likely to provide new insights into many disease mechanisms.

7.4 Translational science: from animal to human

Animal models have been a fundamental tool in the preclinical studies for many years [543]. Rodents, usually mice and rats, have been the most commonly used animals in biomedical research for a variety of reasons, including their manageable small size, generally mild-tempered and docile, ease of housing and maintenance, short reproductive cycle and lifespan, abundant genetic resources and similarities to the human anatomy, physiology, and genetic setup [544]. Moreover, larger size animals such as rats and pigs are the preferred models for studies involving surgical procedures. This is due to the fact that surgery is generally easier and causes less tissue damage in a larger animals [545]. In this thesis, mice were used in **chapter 2** (atherosclerosis), **chapter 3** (atherosclerosis), and **chapter 5** (cancer). In **chapter 4** (abdominal fascial healing), rats were used due to the performance of a surgical open hemicolectomy.

Even though laboratory rats and mice serve as the preferred animal models for biomedical research due to the advantages mentioned earlier, they cannot sufficiently reflect human disorders owing to several limitations in some aspects (e.g. immunology differences among others) [546]. For instance, in atherosclerosis, lesions prefer to present in coronary arteries in humans compared to the aorta and carotids in rodents [547]. Moreover, the commonly used atherosclerotic mouse models do not reflect the instability and rupture of lesions as seen in humans [548]. In oncology, the xenograft animal models offer many advantages, such as the reduction of inter-subject variability while producing a realistic heterogeneity of tumor cells [549]. However, xenograft animal models are unable to fully mimic the complex tumor microenvironment in humans, partially owing to these animals are usually immune-compromised and cannot induce the same immune responses as human [549]. Therefore, translational studies from animal models to human are indispensable in both oncological and cardiovascular diseases.

Atherosclerotic plaque-specific markers in human tissues

In **chapter 2**, we aimed to identify common plaque-specific lipids in $ldlr^{-/-}$ mice and $apoe^{-/-}$ mice, the two most widely used animal models for atherosclerosis research, by MALDI-MSI. This study identified ten lysolipids and one sphingomyelin as integral constituents of the plaque in both $ldlr^{-/-}$ and $apoe^{-/-}$ mouse models. These novel results help to unravel the molecular complexity of atherosclerotic plaques. The fact that our results are consistent across the two different models is promising and indicates that they could be extended to the study of human plaque and plasma samples. Moreover, it is important to note that during my PhD, I also analyzed one fresh frozen human carotid plaque sample with the same method as described in **chapter 2**. I detected and verified all 11 plaque specific lipids in human carotid plaque (Figure 7.4). I also observed that human plaque is far more complex than a typical mouse plaque and that some lipids showed distinct spatial distributions within the plaque as compared to the mouse samples. This shows again the necessity to perform translational studies in human samples to investigate their validity and potential as biomarkers.
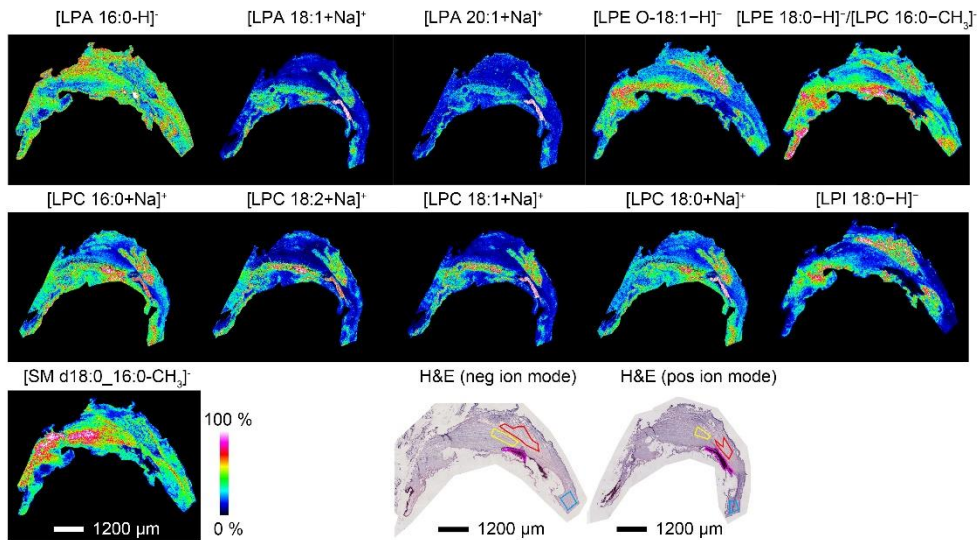
Figure 7.4. Visualization of 11 (6 in negative ion mode and 5 in positive ion mode) plaque-specific lipids from *ldlr*$^{-/-}$ mice and *apoe*$^{-/-}$ mice in a human carotid plaque. Their coregistered, hematoxylin and eosin stained (H&E) images are shown at the bottom (necrotic core region, fibrous region, macrocalcification region and intimal xanthoma containing foam cells region are indicated in red, yellow, pink and blue, respectively).

Furthermore, even though the pathologic development of atherosclerotic lesions in *ldlr*$^{-/-}$ and *apoe*$^{-/-}$ mouse models is similar to the human as described in **chapter 1** [550], there are still some distinct differences compared to human atherosclerosis. The primary site for clinically significant atherosclerotic disease in humans is the coronary arteries, with progression to atherothrombotic events leading potentially to a myocardial infarction [551]. However, lesions in mice mainly develop in the aorta and carotids regions where disturbed blood flow occurs [550]. Moreover, the mouse models rarely show evidence of lesion rupture [550], while around 3/4 of heart attacks in humans result from plaque rupture followed by thrombosis [550]. In addition, most of atherosclerotic mouse models were performed on a single genetic background C57BL/6J (**chapter 2** and **chapter 3**), which limits to fully represent the genetics of human atherosclerosis [550]. Because of these reasons, it is necessary to translate my findings from the animal models to human studies, especially since there is the potential to derive from these studies novel diagnostic or therapeutic biomarkers for this global health problem.

From understanding fascia wound healing in a rat model to improve clinical wound care in humans

Fascial wound healing is a dynamic and complex biological process interfered by a multitude of local and systemic factors, such as oxygenation, invasive infection, age, sex, stress, nutrition, smoking and a variety of diseases (e.g. atherosclerosis, obesity) [552]. Failure of laparotomy fascia healing can cause incisional hernias, which is one of the major complications after open abdominal surgery and significantly affect overall life quality of

patients [553]. Despite the fact that acute wounds generally go through the normal stages of the healing process namely hemostasis, inflammation, proliferation, and remodeling [249], the underlying cellular and molecular interactions of fascia wound healing are still poorly understood. Moreover, developing effective wound healing agents and therapeutic approaches to wound management remains a scientific challenge for medical societies [554]. Since it is ethically and practically impossible to isolate functionally healed fascia from patients, animal models such as rats are extensively used in wound healing studies. They also offer the advantage of an accelerated wound healing process in days compared to weeks in humans. Furthermore, Occleston *et al.* demonstrated that the gene expression identified across all key stages of the healing and scarring process is comparable between rat and man [421]. This is the reason why in **chapter 4**, rats were chosen to model human normal abdominal fascial healing. The study demonstrates the temporal changes of lipids correlated to inflammatory response and fibroblast growth in acutely injured fascia.

However, it is important to note that there are numerous dissimilarities when comparing rats to humans. For instance, the rodents' skin anatomy and physiology is significantly different from that in humans [555, 556]. For instance, rodents have the ability to produce endogenously vitamin C in the liver which is vital for the whole healing process [556], while for humans this is not the case. Therefore, these differences must be taken into account for a better translation to the human condition and for improving clinical wound care.

Local phenylalanine metabolism in human samples

Following the same argumentation for my work reported in **chapter 5**, this study demonstrates the usefulness of MSI to investigate spatial kinetics of Phe and Tyr in a mouse-xenograft model of non-small cell lung carcinoma. In this study, the MSI data from the tumor was integrated with the data from the live and the plasma [491] collected from the same mice. Therefore, this study also reflects inter-organ amino acid metabolism. However, it has been reported that the kidney is also contributing to the production of Tyrosine from Phenylalanine [557], it would be interesting to also apply MSI to kidney tissue from the same mice to get the full view on inter-organ amino acid metabolism in this study or to perform whole body MSI [558]. Following the same line, integrating MSI with *in vivo* techniques such as MRI or micro-PET could facilitate the extension of the results to dynamics of inter-organ metabolism.

With respect to the mouse model used in this study, it is noteworthy to bear in mind that mouse Phenylalanine hydroxylase (PAH) exhibits multiple potentially significant differences to human PAH despite profound resemblance between them, as presented by Ledley *et al.* [559]. In addition, it is known that preclinical cancer models show limitations for representing the real human tumor microenvironment [560]. Moreover, tumor cells in mice are limited in space to grow compared to a human and are therefore limited to produce the variety of genetic mutations and subpopulations found in humans [560]. Nevertheless, the translation of the results to humans can deepen the knowledge on metabolic events driving oncogenesis, as well as offer new options in tumor treatment. With respect to the latter, the

isotopic labeling approach of **chapter 5** could be applied to cancer patients to assess the effectiveness of chemotherapy based on the incorporation of ^{13}C-Phe in biopsies from patients. This way might be faster and cheaper than the three months required by the RECIST response evaluation criteria [561] or the computed tomography scans done in clinics.

Outlook

In summary, the work in this thesis demonstrates that MALDI-MSI is a valuable tool for *in situ* metabolomics of biological tissue specimens encountered in many preclinical studies. Advances in sample preparation and MS instrumentation to increase sensitivity, spatial resolution, mass resolution, and the molecular coverage of metabolites, together with the integration of MSI with other imaging modalities and other omics techniques, will bring MALDI-MSI metabolomics research to the next level and allow a deeper understanding of complexity of biological and pathological processes at a single cell scale. While animal models offer many advantages for preclinical research, they cannot perfectly model the human condition, which makes the translation of the research results from the preclinical studies to the human necessary. In the same context, multicenter preclinical studies together with clinically well-recognized extraction-based MS techniques (e.g. LC-MS) to evaluate the robustness and reproducibility of MSI data could improve the translatability of preclinical studies.

Chapter 8

Summary

MALDI mass spectrometry imaging is an attractive technique for *in situ* visualization of metabolites directly on tissues, which is essential for a better understanding of complex mechanisms underlying heterogeneous diseases. The work presented in this thesis focuses on the investigation of the local metabolism in atherosclerosis, wound healing and cancer in animal models using metabolomics-based MALDI mass spectrometry imaging.

In **chapter 2**, I applied high-spatial-resolution 2D and 3D MALDI-TOF-MSI to identify and verify aortic plaque-specific lipids in two of the most widely used animal models for atherosclerosis, including high fat diet-fed low density lipoprotein receptor deficient ($ldlr^{-/-}$) mice and chow-fed apolipoprotein E deficient ($apoe^{-/-}$) mice. In a first phase, I investigated plaque-specific lipids in $ldlr^{-/-}$ mice and $apoe^{-/-}$ mice on a two-dimensional level involving several replicates. Subsequently, I verified the volumetric plaque specificity of those lipids by 3D-MALDI-MSI in an $apoe^{-/-}$ mouse to confirm the universal presence of these lipids along the plaque. All the results presented in this study suggest that lysolipids and sphingomyelins are integral constituents of the plaque in both atherosclerotic mouse models. More specifically, LPI 18:0 was concentrated in the necrotic core of plaques. These novel results are helping to unravel the molecular complexity of the atherosclerotic plaque thereby enhancing not only our understanding of the plaque's composition but also the identification of potential lipid species related to the plaque's stability.

In **chapter 3**, I performed untargeted MALDI-FTICR-MSI metabolomic analysis on atherosclerotic aortic tissues from high fat diet compared to normal diet $ldlr^{-/-}$ mice to characterize metabolic alterations associated with an earlier stage of atherosclerosis (compared to **Chapter 2**) while locating them within the aortic structure. For metabolites of interest, additional targeted LC-MS/MS in selected reaction monitoring mode was performed in human plasma in order to evaluate the potential of the tissue findings as atherosclerotic plasma markers. This study indicates an altered lipid metabolism occurring in atherosclerosis, which affects both, the aorta as well as the adjacent heart tissue. Moreover, it demonstrates that the combination of untargeted *in situ* metabolomics of atherosclerotic aortic tissue with complementary targeted metabolomics of plasma offers a holistic strategy to better understand systemic and local metabolic processes involved in the onset and progression of atherosclerosis and to discover novel minimally-invasive markers with diagnostic potential.

In **chapter 4**, I studied temporal and *in situ* lipids alterations during the normal healing process of abdominal fascia in rats during the first postoperative week using MALDI-TOF-MSI. Later, the observed lipids alterations were correlated with histologically scored changes (inflammation and fibroblast scores) based on hematoxylin and eosin staining. Glycerophospholipids and gangliosides were found significantly involved in the normal healing process of abdominal fascia and their locally fluctuating concentrations are considered as potential lipid markers and/or therapeutic targets for the prevention of incisional hernia in patients.

And finally in **chapter 5**, I investigated L-[ring-^{13}C$_6$]-labeled phenylalanine and tyrosine kinetics in a human non-small cell lung carcinoma xenografted mouse model using MALDI-FTICR-MSI. Using MSI of tumor tissue and MS of plasma, I was able to study the local and systemic phenylalanine metabolism in the tumor itself and its near environment and systemically in the blood levels. Moreover, this study together with the results from a previous study focusing on liver enabled to understand inter-organ amino acid metabolism and shifting effects. The translation to human samples will offer new insights in diagnostic molecular markers and develop novel strategies for cancer therapy.

In summary, all studies in this thesis highlight the importance to study the metabolism of diseases locally in the tissue of origin. Mass spectrometry imaging facilitates in the form of a spatial metabolomics approach. In addition, both non-targeted and targeted metabolomics-based MALDI-MSI studies provide not only new biomarkers for clinical trials but also novel insights into metabolic mechanism of diseases that complement morphological observations in the diseased tissues.

Chapter 9

Samenvatting

MALDI-beeldvorming massa spectrometrie is een aantrekkelijke techniek, geschikt voor de *in situ* visualisatie van metabolieten in weefsels. Metabolische visualisatie is essentieel voor onderzoek naar complexe mechanismen die ten grondslag liggen aan heterogene ziekten. Het onderzoekt, beschreven dit manuscript, focust zich op de lokale metabolisme van atherosclerose, wondheling en kanker in diermodellen met behulp van MALDI-beeldvorming massa spectrometrie.

In **hoofdstuk 2** heb ik hoge ruimtelijke resolutie 2D en 3D MALDI-TOF-MSI toegepast om aortaplaque specifieke lipiden te identificeren en te verifiëren. Hiervoor werden twee van de meest onderzochte atherosclerose diermodellen gebruikt, waaronder muizen met een deficiënte lage-dichtheid lipoproteïne receptor (*ldlr*$^{-/-}$) die een vetrijk dieet ondergingen. Daarnaast ook apolipoproteine E (*apoe*$^{-/-}$) deficiënte muizen die een normaal (chow-fed) dieet ontvingen. Tijdens de eerste fase werden plaque-specifieke lipiden onderzocht in *ldlr*$^{-/-}$ en *apoe*$^{-/-}$ muizen op een tweedimensionaal niveau in replica's. Vervolgens heb ik de plaquespecificiteit van die lipiden geverifieerd met 3D-MALDI-MSI in een *apoe*$^{-/-}$ muis om de aanwezigheid van de lipiden rondom de plaques te bevestigen. De resultaten die in deze studie worden gepresenteerd, suggereren dat lysolipiden en shingomyelines zich in de plaque beide atherosclerotische muismodellen bevinden. Deze nieuwe resultaten helpen de moleculaire complexiteit van de atherosclerotische plaque te ontrafelen, waardoor niet alleen onze kennis van de plaque samenstelling wordt verbeterd, maar ook de identificatie van potentiële lipidensoorten die verband houden met de stabiliteit van de plaque.

In **hoofdstuk 3** heb ik ongerichte MALDI-FTICR-MSI metabolische analyses uitgevoerd op atherosclerotische aortaweefsels van *ldlr*$^{-/-}$ muizen met een vetrijk dieet in vergelijking met een normaal dieet. Deze metingen werden uitgevoerd om metabolische veranderingen, geassocieerd met atherosclerose, te karakteriseren en ze binnen de aortastructuur te lokaliseren. Aanvullende werd gerichte LC-MS/MS uitgevoerd voor specifieke metabolieten in humane plasma door middel van 'selected reaction monitoring'. Deze analyse werd uitgevoerd om de mogelijkheid van de weefselbevindingen als atherosclerotische plasmamarkers te evalueren. Deze studie toont aan dat de combinatie van ongericht in situ metabolisch onderzoek aan atherosclerotisch aortaweefsel, door middel van gericht metabolisch onderzoek een holistische strategie biedt om systemische en lokale metabole processen, betrokken bij de progressie van atherosclerose in een vroeg stadium, beter te begrijpen en om nieuwe minimaal-invasieve markers met diagnostisch potentieel te ontdekken.

In **hoofdstuk 4** heb ik tijdelijke en *in situ* lipidenveranderingen bestudeerd tijdens het normale genezingsproces van abdominale fascia bij ratten in de eerste postoperatieve week. Dit onderzoek werd uitgevoerd met behulp van MALDI-TOF-MSI. Later werden de waargenomen lipidenveranderingen gecorreleerd met histologische veranderingen (ontstekingen en fibroblastscores) op basis van hematoxyline- en eosine-kleuring. Glycerofosfolipiden en gangliosiden bleken significant betrokken te zijn bij het normale

genezingsproces van abdominale fascia. Hun lokaal fluctuerende concentraties worden beschouwd als potentiële lipidenmarkers en/of therapeutische indicatoren voor de preventie van incisionele hernia bij patiënten.

Tot slot, in **hoofdstuk 5**, heb ik de kinetiek van L-[ring-^{13}C$_6$] -gelabelde fenylalanine en thyroxine onderzocht in een humaan, niet-kleincellig longcarcinoom xenogetransplanteerd, muismodel met behulp van MALDI-FTICR-MSI. Door middel van de MSI-analyses van tumorweefsel en MS-analyse van plasma kon ik het lokale en systemische fenylalaninemetabolisme in de tumor, de nabije omgeving en in de bloedspiegels bestuderen. Bovendien maakte deze studie, samen met de resultaten van een eerdere studie gericht op de lever, het mogelijk om het aminozuurmetabolisme tussen organen en verschuivende effecten in kaart te brengen. De vertaling naar menselijke samples zal nieuwe inzichten bieden in diagnostische moleculaire markers en strategieën voor kankertherapie ontwikkelen.

Samengevat, zowel niet-gerichte als gerichte op metabolisch gebaseerde MALDI-MSI-onderzoeken bieden nieuwe bio-markers voor klinische onderzoeken. Daarnaast biedt dit inzichten in het metabole mechanisme van ziekten die een aanvulling vormen op morfologische waarnemingen in de ziekteweefsels.

Appendices

The supplementary materials of **Chapters 2–5** can be found through the respective links or QR codes below:

Chapter 2

https://pubs.acs.org/doi/10.1021/jasms.0c00070?goto=supporting-info

Chapter 3:

https://www.dropbox.com/sh/xb8fecwvl1li33f/AAA1KO4Ca18wQi3VGZ1mdNtua?dl=0

Chapter 4:

https://www.sciencedirect.com/science/article/pii/S2667145X21000110?via%3Dihub#s0090

Chapter 5:

https://cancerandmetabolism.biomedcentral.com/articles/10.1186/s40170-021-00262-9#Sec16

References

References

1. DeBerardinis, R.J. and C.B. Thompson, *Cellular metabolism and disease: what do metabolic outliers teach us?* Cell, 2012. **148**(6): p. 1132-44.

2. Dunn, W.B., et al., *Systems level studies of mammalian metabolomes: the roles of mass spectrometry and nuclear magnetic resonance spectroscopy.* Chem Soc Rev, 2011. **40**(1): p. 387-426.

3. DeBerardinis, R.J. and C.B. Thompson, *Cellular Metabolism and Disease: What Do Metabolic Outliers Teach Us?* Cell, 2012. **148**(6): p. 1132-1144.

4. Wishart, D.S., *Metabolomics for Investigating Physiological and Pathophysiological Processes.* Physiol Rev, 2019. **99**(4): p. 1819-1875.

5. Berry, K.A., et al., *MALDI imaging of lipid biochemistry in tissues by mass spectrometry.* Chem Rev, 2011. **111**(10): p. 6491-512.

6. Wu, G., *Amino acids: metabolism, functions, and nutrition.* Amino Acids, 2009. **37**(1): p. 1-17.

7. Dalangin, R., A. Kim, and R.E. Campbell, *The Role of Amino Acids in Neurotransmission and Fluorescent Tools for Their Detection.* Int J Mol Sci, 2020. **21**(17).

8. Broer, S. and A. Broer, *Amino acid homeostasis and signalling in mammalian cells and organisms.* Biochem J, 2017. **474**(12): p. 1935-1963.

9. Zenobi, R., *Single-cell metabolomics: analytical and biological perspectives.* Science, 2013. **342**(6163): p. 1243259.

10. Zeki, O.C., et al., *Integration of GC-MS and LC-MS for untargeted metabolomics profiling.* J Pharm Biomed Anal, 2020. **190**: p. 113509.

11. Newgard, C.B., *Metabolomics and Metabolic Diseases: Where Do We Stand?* Cell Metab, 2017. **25**(1): p. 43-56.

12. Nelson, R.H., *Hyperlipidemia as a risk factor for cardiovascular disease.* Prim Care, 2013. **40**(1): p. 195-211.

13. Pavlova, N.N. and C.B. Thompson, *The Emerging Hallmarks of Cancer Metabolism.* Cell Metab, 2016. **23**(1): p. 27-47.

14. Wishart, D.S., et al., *HMDB: a knowledgebase for the human metabolome.* Nucleic Acids Res, 2009. **37**(Database issue): p. D603-10.

15. Wishart, D.S., et al., *HMDB 4.0: the human metabolome database for 2018.* Nucleic Acids Res, 2018. **46**(D1): p. D608-D617.

16. Lei, Z., D.V. Huhman, and L.W. Sumner, *Mass spectrometry strategies in metabolomics.* J Biol Chem, 2011. **286**(29): p. 25435-42.

17. McLafferty, F.W., *A century of progress in molecular mass spectrometry.* Annu Rev Anal Chem (Palo Alto Calif), 2011. **4**: p. 1-22.

18. Chughtai, K. and R.M. Heeren, *Mass spectrometric imaging for biomedical tissue analysis.* Chem Rev, 2010. **110**(5): p. 3237-77.

19. Zheng, W., et al., *Ceramides and other bioactive sphingolipid backbones in health and disease: lipidomic analysis, metabolism and roles in membrane structure, dynamics, signaling and autophagy.* Biochim Biophys Acta, 2006. **1758**(12): p. 1864-84.

20. Timp, W. and G. Timp, *Beyond mass spectrometry, the next step in proteomics.* Sci Adv, 2020. **6**(2): p. eaax8978.

21. Gupta, R.K. and J. Kuznicki, *Biological and Medical Importance of Cellular Heterogeneity Deciphered by Single-Cell RNA Sequencing.* Cells, 2020. **9**(8).

22. Junker, J.P. and A. van Oudenaarden, *Every cell is special: genome-wide studies add a new dimension to single-cell biology.* Cell, 2014. **157**(1): p. 8-11.

23. Taylor, M.J., J.K. Lukowski, and C.R. Anderton, *Spatially Resolved Mass Spectrometry at the Single Cell: Recent Innovations in Proteomics and Metabolomics.* Journal of the American Society for Mass Spectrometry, 2021. **32**(4): p. 872-894.

24.   Galler, K., et al., *Making a big thing of a small cell--recent advances in single cell analysis.* Analyst, 2014. **139**(6): p. 1237-73.

25.   van Meer, G., D.R. Voelker, and G.W. Feigenson, *Membrane lipids: where they are and how they behave.* Nature Reviews Molecular Cell Biology, 2008. **9**(2): p. 112-124.

26.   Almendro, V., A. Marusyk, and K. Polyak, *Cellular Heterogeneity and Molecular Evolution in Cancer.* Annual Review of Pathology: Mechanisms of Disease, Vol 8, 2013. **8**: p. 277-302.

27.   Emmert-Buck, M.R., et al., *Laser capture microdissection.* Science, 1996. **274**(5289): p. 998-1001.

28.   Pichler, B.J., H.F. Wehrl, and M.S. Judenhofer, *Latest advances in molecular imaging instrumentation.* J Nucl Med, 2008. **49 Suppl 2**: p. 5S-23S.

29.   Miura, D., Y. Fujimura, and H. Wariishi, *In situ metabolomic mass spectrometry imaging: recent advances and difficulties.* J Proteomics, 2012. **75**(16): p. 5052-5060.

30.   Vaysse, P.M., et al., *Mass spectrometry imaging for clinical research - latest developments, applications, and current limitations.* Analyst, 2017. **142**(15): p. 2690-2712.

31.   Addie, R.D., et al., *Current State and Future Challenges of Mass Spectrometry Imaging for Clinical Research.* Anal Chem, 2015. **87**(13): p. 6426-33.

32.   Heeren, R.M.A., *Getting the picture: The coming of age of imaging MS.* International Journal of Mass Spectrometry, 2015. **377**: p. 672-680.

33.   Caprioli, R.M., T.B. Farmer, and J. Gile, *Molecular imaging of biological samples: localization of peptides and proteins using MALDI-TOF MS.* Anal Chem, 1997. **69**(23): p. 4751-60.

34.   Takats, Z., et al., *Electrosonic spray ionization. A gentle technique for generating folded proteins and protein complexes in the gas phase and for studying ion - Molecule reactions at atmospheric pressure.* Analytical Chemistry, 2004. **76**(14): p. 4050-4058.

35.   Buchberger, A.R., et al., *Mass Spectrometry Imaging: A Review of Emerging Advancements and Future Insights.* Anal Chem, 2018. **90**(1): p. 240-265.

36.   Sodhi, R.N.S., *Time-of-flight secondary ion mass spectrometry (TOF-SIMS): versatility in chemical and imaging surface analysis.* Analyst, 2004. **129**(6): p. 483-487.

37.   Nunez, J., et al., *NanoSIMS for biological applications: Current practices and analyses.* Biointerphases, 2018. **13**(3).

38.   Nygren, H. and P. Malmberg, *High resolution imaging by organic secondary ion mass spectrometry.* Trends Biotechnol, 2007. **25**(11): p. 499-504.

39.   McDonnell, L.A., et al., *Subcellular imaging mass spectrometry of brain tissue.* J Mass Spectrom, 2005. **40**(2): p. 160-8.

40.   Wiseman, J.M., et al., *Tissue imaging at atmospheric pressure using desorption electrospray ionization (DESI) mass spectrometry.* Angewandte Chemie-International Edition, 2006. **45**(43): p. 7188-7192.

41.   Wiseman, J.M., et al., *Desorption electrospray ionization mass spectrometry: Imaging drugs and metabolites in tissues.* Proceedings of the National Academy of Sciences of the United States of America, 2008. **105**(47): p. 18120-18125.

42.   Parrot, D., et al., *Imaging the Unimaginable: Desorption Electrospray Ionization - Imaging Mass Spectrometry (DESI-IMS) in Natural Product Research.* Planta Medica, 2018. **84**(9-10).

43.   Wu, C.P., et al., *Mass spectrometry imaging under ambient conditions.* Mass Spectrometry Reviews, 2013. **32**(3): p. 218-243.

44.   Balluff, B., et al., *MALDI imaging mass spectrometry for direct tissue analysis: technological advancements and recent applications.* Histochem Cell Biol, 2011. **136**(3): p. 227-44.

45.   Scupakova, K., et al., *Morphometric Cell Classification for Single-Cell MALDI-Mass Spectrometry Imaging.* Angewandte Chemie-International Edition, 2020. **59**(40): p. 17447-17450.

46.   Fenselau, C. and P.A. Demirev, *Characterization of intact microorganisms by MALDI mass spectrometry.* Mass Spectrom Rev, 2001. **20**(4): p. 157-71.

47.   Cao, J., et al., *Atheroma-Specific Lipids in ldlr(-/-) and apoe(-/-) Mice Using 2D and 3D Matrix-Assisted Laser Desorption/Ionization Mass Spectrometry Imaging.* J Am Soc Mass Spectrom, 2020. **31**(9): p. 1825-1832.

48.   Sturtevant, D., Y.J. Lee, and K.D. Chapman, *Matrix assisted laser desorption/ionization-mass spectrometry imaging (MALDI-MSI) for direct visualization of plant metabolites in situ.* Curr Opin Biotechnol, 2016. **37**: p. 53-60.

49.   Nakamura, J., et al., *Spatially resolved metabolic distribution for unraveling the physiological change and responses in tomato fruit using matrix-assisted laser desorption/ionization-mass spectrometry imaging (MALDI-MSI).* Anal Bioanal Chem, 2017. **409**(6): p. 1697-1706.

50.   Stephens, W.E., B. Serin, and W.E. Meyerhof, *A Method for Measuring Effective Contact e.m.f. between a Metal and a Semi-conductor.* Physical Review, 1946. **69**(1-2): p. 42-43.

51.   Wiley, W.C. and I.H. McLaren, *Time-of-flight mass spectrometer with improved resolution (Reprinted from Review of Scientific Instruments vol 26, pg 1150, 1995).* Journal of Mass Spectrometry, 1997. **32**(1): p. 4-11.

52.   Mamyrin, B.A., *Time-of-flight mass spectrometry (concepts, achievements, and prospects).* International Journal of Mass Spectrometry, 2001. **206**(3): p. 251-266.

53.   Kovtoun, S.V., R.D. English, and R.J. Cotter, *Mass correlated acceleration in a reflectron MALDI TOF mass spectrometer: an approach for enhanced resolution over a broad mass range.* J Am Soc Mass Spectrom, 2002. **13**(2): p. 135-43.

54.   Mendis, L., *Distribution of Lipids in the Human Brain and their Differential Expression in Alzheimer's Disease: A Matrix-Assisted Laser Desorption/Ionisation-Imaging Mass Spectrometry (MALDI-IMS) Study.* 2016.

55.   Sage, E., *New concept of mass spectrometer based on arrays of resonating nanostructures.* 2013.

56.   Marshall, A.G., C.L. Hendrickson, and G.S. Jackson, *Fourier transform ion cyclotron resonance mass spectrometry: a primer.* Mass Spectrom Rev, 1998. **17**(1): p. 1-35.

57.   Bowman, A.P., et al., *Ultra-High Mass Resolving Power, Mass Accuracy, and Dynamic Range MALDI Mass Spectrometry Imaging by 21-T FT-ICR MS.* Anal Chem, 2020. **92**(4): p. 3133-3142.

58.   Heeren, R.M., et al., *A mini-review of mass spectrometry using high-performance FTICR-MS methods.* Anal Bioanal Chem, 2004. **378**(4): p. 1048-58.

59.   Han, J., et al., *Towards high-throughput metabolomics using ultrahigh-field Fourier transform ion cyclotron resonance mass spectrometry.* Metabolomics, 2008. **4**(2): p. 128-140.

60.   Dilillo, M., et al., *Ultra-High Mass Resolution MALDI Imaging Mass Spectrometry of Proteins and Metabolites in a Mouse Model of Glioblastoma.* Sci Rep, 2017. **7**(1): p. 603.

61.   Sun, N., et al., *Pharmacokinetic and pharmacometabolomic study of pirfenidone in normal mouse tissues using high mass resolution MALDI-FTICR-mass spectrometry imaging.* Histochemistry and Cell Biology, 2016. **145**(2): p. 201-211.

62.   Scupakova, K., et al., *Cellular resolution in clinical MALDI mass spectrometry imaging: the latest advancements and current challenges.* Clinical Chemistry and Laboratory Medicine, 2020. **58**(6): p. 914-929.

63.   Ly, A., et al., *Site-to-Site Reproducibility and Spatial Resolution in MALDI-MSI of Peptides from Formalin-Fixed Paraffin-Embedded Samples.* Proteomics Clinical Applications, 2019. **13**(1).

64.   Drake, R.R., et al., *MALDI Mass Spectrometry Imaging of N-Linked Glycans in Cancer Tissues.* Applications of Mass Spectrometry Imaging to Cancer, 2017. **134**: p. 85-116.

65.   Ly, A., et al., *High-mass-resolution MALDI mass spectrometry imaging of metabolites from formalin-fixed paraffin-embedded tissue.* Nat Protoc, 2016. **11**(8): p. 1428-43.

66.   Saito, T., et al., *MALDI-TOF mass spectrometry imaging for N-glycans on FFPE tissue sections of mouse NASH liver through Sialic acid Benzylamidation.* Glycoconjugate Journal, 2021. **38**(2): p. 167-175.

67. Casadonte, R. and R.M. Caprioli, *Proteomic analysis of formalin-fixed paraffin-embedded tissue by MALDI imaging mass spectrometry.* Nature Protocols, 2011. **6**(11): p. 1695-1709.

68. Hermann, J., et al., *Sample preparation of formalin-fixed paraffin-embedded tissue sections for MALDI-mass spectrometry imaging (vol 412, pg 1263, 2020).* Analytical and Bioanalytical Chemistry, 2021. **413**(11): p. 3141-3141.

69. Vos, D.R.N., et al., *Class-specific depletion of lipid ion signals in tissues upon formalin fixation.* International Journal of Mass Spectrometry, 2019. **446**.

70. Hankin, J.A., R.M. Barkley, and R.C. Murphy, *Sublimation as a method of matrix application for mass spectrometric imaging.* Journal of the American Society for Mass Spectrometry, 2007. **18**(9): p. 1646-1652.

71. Potocnik, N.O., et al., *Use of advantageous, volatile matrices enabled by next-generation high-speed matrix-assisted laser desorption/ionization time-of-flight imaging employing a scanning laser beam.* Rapid Communications in Mass Spectrometry, 2015. **29**(23): p. 2195-2203.

72. Zavalin, A., et al., *Tissue protein imaging at 1 mum laser spot diameter for high spatial resolution and high imaging speed using transmission geometry MALDI TOF MS.* Anal Bioanal Chem, 2015. **407**(8): p. 2337-42.

73. Smith, A., et al., *Matrix-Assisted Laser Desorption/Ionisation Mass Spectrometry Imaging in the Study of Gastric Cancer: A Mini Review.* Int J Mol Sci, 2017. **18**(12).

74. Veerasammy, K., et al., *Sample Preparation for Metabolic Profiling using MALDI Mass Spectrometry Imaging.* J Vis Exp, 2020(166).

75. Mulder, I.A., et al., *Funnel-freezing versus heat-stabilization for the visualization of metabolites by mass spectrometry imaging in a mouse stroke model.* Proteomics, 2016. **16**(11-12): p. 1652-9.

76. Harkin, C., et al., *On-tissue chemical derivatization in mass spectrometry imaging.* Mass Spectrometry Reviews, 2021.

77. Zhou, Q., A. Fulop, and C. Hopf, *Recent developments of novel matrices and on-tissue chemical derivatization reagents for MALDI-MSI.* Anal Bioanal Chem, 2021. **413**(10): p. 2599-2617.

78. Toue, S., et al., *Microscopic imaging mass spectrometry assisted by on-tissue chemical derivatization for visualizing multiple amino acids in human colon cancer xenografts.* Proteomics, 2014. **14**(7-8): p. 810-9.

79. Esteve, C., et al., *Mass spectrometry imaging of amino neurotransmitters: a comparison of derivatization methods and application in mouse brain tissue.* Metabolomics, 2016. **12**: p. 30.

80. Cao, J., et al., *Mass spectrometry imaging of L-[ring-(13)C6]-labeled phenylalanine and tyrosine kinetics in non-small cell lung carcinoma.* Cancer Metab, 2021. **9**(1): p. 26.

81. Arts, M., et al., *Detection of Localized Hepatocellular Amino Acid Kinetics by using Mass Spectrometry Imaging of Stable Isotopes.* Angew Chem Int Ed Engl, 2017. **56**(25): p. 7146-7150.

82. Gemperline, E., S. Rawson, and L. Li, *Optimization and comparison of multiple MALDI matrix application methods for small molecule mass spectrometric imaging.* Anal Chem, 2014. **86**(20): p. 10030-5.

83. Huizing, L.R.S., et al., *Development and evaluation of matrix application techniques for high throughput mass spectrometry imaging of tissues in the clinic.* Clinical Mass Spectrometry, 2019. **12**: p. 7-15.

84. Kompauer, M., S. Heiles, and B. Spengler, *Atmospheric pressure MALDI mass spectrometry imaging of tissues and cells at 1.4-mu m lateral resolution.* Nature Methods, 2017. **14**(1): p. 90-96.

85. Gemperline, E., S. Rawson, and L.J. Li, *Optimization and Comparison of Multiple MALDI Matrix Application Methods for Small Molecule Mass Spectrometric Imaging.* Analytical Chemistry, 2014. **86**(20): p. 10030-10035.

86. Pulfer, M. and R.C. Murphy, *Electrospray mass spectrometry of phospholipids.* Mass Spectrom Rev, 2003. **22**(5): p. 332-64.

87.   Woods, A.S. and S.N. Jackson, *Brain tissue lipidomics: direct probing using matrix-assisted laser desorption/ionization mass spectrometry.* AAPS J, 2006. **8**(2): p. E391-5.

88.   Scott, A.J., et al., *Norharmane matrix enhances detection of endotoxin by MALDI-MS for simultaneous profiling of pathogen, host and vector systems.* Pathogens and Disease, 2016. **74**(8).

89.   Paine, M.R.L., et al., *Three-Dimensional Mass Spectrometry Imaging Identifies Lipid Markers of Medulloblastoma Metastasis.* Scientific Reports, 2019. **9**.

90.   Yang, H., et al., *Streamlined Analysis of Cardiolipins in Prokaryotic and Eukaryotic Samples Using a Norharmane Matrix by MALDI-MSI.* Journal of the American Society for Mass Spectrometry, 2020. **31**(12): p. 2495-2502.

91.   Genangeli, M., et al., *MALDI-Mass Spectrometry Imaging to Investigate Lipid and Bile Acid Modifications Caused by Lentil Extract Used as a Potential Hypocholesterolemic Treatment.* Journal of the American Society for Mass Spectrometry, 2019. **30**(10): p. 2041-2050.

92.   Vermillion-Salsbury, R.L. and D.M. Hercules, *9-aminoacridine as a matrix for negative mode matrix-assisted laser desorption/ionization.* Rapid Communications in Mass Spectrometry, 2002. **16**(16): p. 1575-1581.

93.   Schober, Y., et al., *Single cell matrix-assisted laser desorption/ionization mass spectrometry imaging.* Anal Chem, 2012. **84**(15): p. 6293-7.

94.   Miura, D., et al., *Ultrahighly sensitive in situ metabolomic imaging for visualizing spatiotemporal metabolic behaviors.* Anal Chem, 2010. **82**(23): p. 9789-96.

95.   Sugiura, Y., et al., *Visualization of in vivo metabolic flows reveals accelerated utilization of glucose and lactate in penumbra of ischemic heart.* Sci Rep, 2016. **6**: p. 32361.

96.   Martin-Lorenzo, M., et al., *Molecular anatomy of ascending aorta in atherosclerosis by MS Imaging: Specific lipid and protein patterns reflect pathology.* J Proteomics, 2015. **126**: p. 245-51.

97.   Enthaler, B., et al., *MALDI imaging in human skin tissue sections: focus on various matrices and enzymes.* Anal Bioanal Chem, 2013. **405**(4): p. 1159-70.

98.   Eveque-Mourroux, M.R., et al., *Spatially resolved endogenous improved metabolite detection in human osteoarthritis cartilage by matrix assisted laser desorption ionization mass spectrometry imaging.* Analyst, 2019. **144**(20): p. 5953-5958.

99.   Aichler, M., et al., *N-acyl Taurines and Acylcarnitines Cause an Imbalance in Insulin Synthesis and Secretion Provoking beta Cell Dysfunction in Type 2 Diabetes.* Cell Metab, 2017. **25**(6): p. 1334-1347 e4.

100.   Wang, J., et al., *MALDI-TOF MS imaging of metabolites with a N-(1-naphthyl) ethylenediamine dihydrochloride matrix and its application to colorectal cancer liver metastasis.* Anal Chem, 2015. **87**(1): p. 422-30.

101.   Astigarraga, E., et al., *Profiling and Imaging of Lipids on Brain and Liver Tissue by Matrix-Assisted Laser Desorption/Ionization Mass Spectrometry Using 2-Mercaptobenzothiazole as a Matrix.* Analytical Chemistry, 2008. **80**(23): p. 9105-9114.

102.   Korte, A.R. and Y.J. Lee, *MALDI-MS analysis and imaging of small molecule metabolites with 1,5-diaminonaphthalene (DAN).* Journal of Mass Spectrometry, 2014. **49**(8): p. 737-741.

103.   Vos, D.R.N., et al., *Experimental and Data Analysis Considerations for Three-Dimensional Mass Spectrometry Imaging in Biomedical Research.* Mol Imaging Biol, 2021. **23**(2): p. 149-159.

104.   Prade, V.M., et al., *De novo discovery of metabolic heterogeneity with immunophenotype-guided imaging mass spectrometry.* Molecular Metabolism, 2020. **36**.

105.   Wang, J.H., J. Byun, and S. Pennathur, *Analytical approaches to metabolomics and applications to systems biology.* Semin Nephrol, 2010. **30**(5): p. 500-11.

106.   Norris, J.L. and R.M. Caprioli, *Imaging mass spectrometry: a new tool for pathology in a molecular age.* Proteomics Clin Appl, 2013. **7**(11-12): p. 733-8.

107. Harayama, T. and H. Riezman, *Understanding the diversity of membrane lipid composition.* Nat Rev Mol Cell Biol, 2018. **19**(5): p. 281-296.

108. Jain, M., et al., *A systematic survey of lipids across mouse tissues.* Am J Physiol Endocrinol Metab, 2014. **306**(8): p. E854-68.

109. Hu, T. and J.L. Zhang, *Mass-spectrometry-based lipidomics.* J Sep Sci, 2018. **41**(1): p. 351-372.

110. Muro, E., G.E. Atilla-Gokcumen, and U.S. Eggert, *Lipids in cell biology: how can we understand them better?* Molecular Biology of the Cell, 2014. **25**(12): p. 1819-1823.

111. Jones, E.E., et al., *MALDI imaging mass spectrometry profiling of proteins and lipids in clear cell renal cell carcinoma.* Proteomics, 2014. **14**(7-8): p. 924-35.

112. Wang, S.J., et al., *Matrix-assisted laser desorption/ionization mass spectrometry imaging of cell cultures for the lipidomic analysis of potential lipid markers in human breast cancer invasion.* Rapid Communications in Mass Spectrometry, 2016. **30**(4): p. 533-542.

113. Ide, Y., et al., *Human Breast Cancer Tissues Contain Abundant Phosphatidylcholine(36:1) with High Stearoyl-CoA Desaturase-1 Expression.* Plos One, 2013. **8**(4).

114. Pinzariu, O., B. Georgescu, and C.E. Georgescu, *Metabolomics - A Promising Approach to Pituitary Adenomas.* Frontiers in Endocrinology, 2019. **9**.

115. Sugihara, Y., et al., *Endogenous expression mapping of malignant melanoma by mass spectrometry imaging.* Clinical and Translational Medicine, 2018. **7**.

116. Lou, S., et al., *Prognostic Metabolite Biomarkers for Soft Tissue Sarcomas Discovered by Mass Spectrometry Imaging.* Journal of the American Society for Mass Spectrometry, 2017. **28**(2): p. 376-383.

117. Kaya, I., et al., *Multimodal MALDI Imaging Mass Spectrometry Reveals Spatially Correlated Lipid and Protein Changes in Mouse Heart with Acute Myocardial Infarction.* J Am Soc Mass Spectrom, 2020. **31**(10): p. 2133-2142.

118. Shimizu, Y., et al., *Imaging of lysophosphatidylcholine in an induced pluripotent stem cell-derived endothelial cell network.* Regen Ther, 2020. **14**: p. 299-305.

119. Shi, Y.T., et al., *Mass Spectrometric Imaging Reveals Temporal and Spatial Dynamics of Bioactive Lipids in Arteries Undergoing Restenosis.* Journal of Proteome Research, 2019. **18**(4): p. 1669-1678.

120. Van Nuffel, S., et al., *Multimodal Imaging Mass Spectrometry to Identify Markers of Pulmonary Arterial Hypertension in Human Lung Tissue Using MALDI-ToF, ToF-SIMS, and Hybrid SIMS.* Analytical Chemistry, 2020. **92**(17): p. 12079-12087.

121. Angel, P.M., et al., *MALDI Imaging Mass Spectrometry as a Lipidomic Approach to Heart Valve Research.* J Heart Valve Dis, 2016. **25**(2): p. 240-252.

122. Visscher, M., et al., *Data Processing Pipeline for Lipid Profiling of Carotid Atherosclerotic Plaque with Mass Spectrometry Imaging.* Journal of the American Society for Mass Spectrometry, 2019. **30**(9): p. 1790-1800.

123. Castro-Perez, J., et al., *In vivo isotopically labeled atherosclerotic aorta plaques in ApoE KO mice and molecular profiling by matrix-assisted laser desorption/ionization mass spectrometric imaging.* Rapid Communications in Mass Spectrometry, 2014. **28**(22): p. 2471-2479.

124. Tuthill, B.F., 2nd, et al., *Tissue-specific analysis of lipid species in Drosophila during overnutrition by UHPLC-MS/MS and MALDI-MSI.* J Lipid Res, 2020. **61**(3): p. 275-290.

125. Fernandez-Vega, A., et al., *Optimization of a MALDI-Imaging protocol for studying adipose tissue-associated disorders.* Talanta, 2020. **219**: p. 121184.

126. Grove, K.J., et al., *Diabetic nephropathy induces alterations in the glomerular and tubule lipid profiles.* Journal of Lipid Research, 2014. **55**(7): p. 1375-1385.

127. Berry, K.A.Z., et al., *Spatial organization of lipids in the human retina and optic nerve by MALDI imaging mass spectrometry.* Journal of Lipid Research, 2014. **55**(3): p. 504-515.

128.   Anderson, D.M.G., et al., *High Resolution MALDI Imaging Mass Spectrometry of Retinal Tissue Lipids.* Journal of the American Society for Mass Spectrometry, 2014. **25**(8): p. 1394-1403.

129.   Anderson, D.M.G., et al., *Bis(monoacylglycero) phosphate lipids in the retinal pigment epithelium implicate lysosomal/endosomal dysfunction in a model of Stargardt disease and human retinas.* Scientific Reports, 2017. **7**.

130.   Sun, N., et al., *High-resolution metabolite imaging of light and dark treated retina using MALDI- FTICR mass spectrometry.* Proteomics, 2014. **14**(7-8): p. 913-923.

131.   Scupakova, K., et al., *Spatial Systems Lipidomics Reveals Nonalcoholic Fatty Liver Disease Heterogeneity.* Analytical Chemistry, 2018. **90**(8): p. 5130-5138.

132.   Alamri, H., et al., *Mapping the triglyceride distribution in NAFLD human liver by MALDI imaging mass spectrometry reveals molecular differences in micro and macro steatosis.* Analytical and Bioanalytical Chemistry, 2019. **411**(4): p. 885-894.

133.   Wattacheril, J., et al., *Differential Intrahepatic Phospholipid Zonation in Simple Steatosis and Nonalcoholic Steatohepatitis.* Plos One, 2013. **8**(2).

134.   Flinders, B., et al., *Cross-Species Molecular Imaging of Bile Salts and Lipids in Liver: Identification of Molecular Structural Markers in Health and Disease.* Analytical Chemistry, 2018. **90**(20): p. 11835-11846.

135.   Eveque-Mourroux, M.R., et al., *Heterogeneity of Lipid and Protein Cartilage Profiles Associated with Human Osteoarthritis with or without Type 2 Diabetes Mellitus.* Journal of Proteome Research, 2021. **20**(5): p. 2973-2982.

136.   Rocha, B., et al., *MALDI mass spectrometry imaging in rheumatic diseases.* Biochimica Et Biophysica Acta-Proteins and Proteomics, 2017. **1865**(7): p. 784-794.

137.   Ruh, H., et al., *MALDI imaging MS reveals candidate lipid markers of polycystic kidney disease.* J Lipid Res, 2013. **54**(10): p. 2785-94.

138.   Noh, S.A., et al., *Alterations in Lipid Profile of the Aging Kidney Identified by MALDI Imaging Mass Spectrometry.* J Proteome Res, 2019. **18**(7): p. 2803-2812.

139.   van Smaalen, T.C., et al., *Rapid Identification of Ischemic Injury in Renal Tissue by Mass-Spectrometry Imaging.* Analytical Chemistry, 2019. **91**(5): p. 3575-3581.

140.   Zhao, C., et al., *MALDI-MS Imaging Reveals Asymmetric Spatial Distribution of Lipid Metabolites from Bisphenol S-Induced Nephrotoxicity.* Analytical Chemistry, 2018. **90**(5): p. 3196-3204.

141.   Moreno-Gordaliza, E., et al., *Lipid imaging for visualizing cilastatin amelioration of cisplatin-induced nephrotoxicity.* J Lipid Res, 2018. **59**(9): p. 1561-1574.

142.   de la Monte, S.M., et al., *Imaging mass spectrometry of frontal white matter lipid changes in human alcoholics.* Alcohol, 2018. **67**: p. 51-63.

143.   Tobias, F., M.T. Olson, and S.M. Cologna, *Mass spectrometry imaging of lipids: untargeted consensus spectra reveal spatial distributions in Niemann-Pick disease type C1.* Journal of Lipid Research, 2018. **59**(12): p. 2446-2455.

144.   Tobias, F., K.C. Pathmasiri, and S.M. Cologna, *Mass spectrometry imaging reveals ganglioside and ceramide localization patterns during cerebellar degeneration in the Npc1(-/-) mouse model.* Analytical and Bioanalytical Chemistry, 2019. **411**(22): p. 5659-5668.

145.   Liang, X.P., et al., *Three-Dimensional Imaging of Whole-Body Zebrafish Revealed Lipid Disorders Associated with Niemann-Pick Disease Type C1.* Analytical Chemistry, 2021. **93**(23): p. 8178-8187.

146.   Kaya, I., et al., *Novel Trimodal MALDI Imaging Mass Spectrometry (IMS3) at 10 mum Reveals Spatial Lipid and Peptide Correlates Implicated in Abeta Plaque Pathology in Alzheimer's Disease.* ACS Chem Neurosci, 2017. **8**(12): p. 2778-2790.

147.   Kaya, I., et al., *Delineating Amyloid Plaque Associated Neuronal Sphingolipids in Transgenic Alzheimer's Disease Mice (tgArcSwe) Using MALDI Imaging Mass Spectrometry.* Acs Chemical Neuroscience, 2017. **8**(2): p. 347-355.

148.   Kaya, I., et al., *Spatial Lipidomics Reveals Region and Long Chain Base Specific Accumulations of Monosialogangliosides in Amyloid Plaques in Familial Alzheimer's Disease Mice (5xFAD) Brain.* Acs Chemical Neuroscience, 2020. **11**(1): p. 14-24.

149.   Kaya, I., et al., *Shedding Light on the Molecular Pathology of Amyloid Plaques in Transgenic Alzheimer's Disease Mice Using Multimodal MALDI Imaging Mass Spectrometry.* Acs Chemical Neuroscience, 2018. **9**(7): p. 1802-1817.

150.   O'Rourke, M.B., et al., *Higher Mass Accuracy MALDI-TOF/TOF Lipid Imaging of Human Brain Tissue in Alzheimer's Disease.* Curr Protoc Mol Biol, 2019. **126**(1): p. e86.

151.   Kaya, I., et al., *Brain region-specific amyloid plaque-associated myelin lipid loss, APOE deposition and disruption of the myelin sheath in familial Alzheimer's disease mice.* J Neurochem, 2020. **154**(1): p. 84-98.

152.   Nunez, K., et al., *Cigarette Smoke-Induced Alterations in Frontal White Matter Lipid Profiles Demonstrated by MALDI-Imaging Mass Spectrometry: Relevance to Alzheimer's Disease.* Journal of Alzheimers Disease, 2016. **51**(1): p. 151-163.

153.   Caughlin, S., et al., *Membrane-lipid homeostasis in a prodromal rat model of Alzheimer's disease: Characteristic profiles in ganglioside distributions during aging detected using MALDI imaging mass spectrometry.* Biochimica Et Biophysica Acta-General Subjects, 2018. **1862**(6): p. 1327-1338.

154.   Hong, J.H., et al., *Global changes of phospholipids identified by MALDI imaging mass spectrometry in a mouse model of Alzheimer's disease.* Journal of Lipid Research, 2016. **57**(1): p. 36-45.

155.   de San Roman, E.G., et al., *Imaging mass spectrometry (IMS) of cortical lipids from preclinical to severe stages of Alzheimer's disease.* Biochimica Et Biophysica Acta-Biomembranes, 2017. **1859**(9): p. 1604-1614.

156.   Michno, W., et al., *Multimodal Chemical Imaging of Amyloid Plaque Polymorphism Reveals Abeta Aggregation Dependent Anionic Lipid Accumulations and Metabolism.* Anal Chem, 2018. **90**(13): p. 8130-8138.

157.   Tong, M., et al., *Altered temporal lobe white matter lipid ion profiles in an experimental model of sporadic Alzheimer's disease.* Mol Cell Neurosci, 2017. **82**: p. 23-34.

158.   Fridjonsdottir, E., et al., *Mass spectrometry imaging identifies abnormally elevated brain L-DOPA levels and extrastriatal monoaminergic dysregulation in L-DOPA-induced dyskinesia.* Science Advances, 2021. **7**(2).

159.   Hunter, M., et al., *An imaging mass spectrometry atlas of lipids in the human neurologically normal and Huntington's disease caudate nucleus.* J Neurochem, 2021. **157**(6): p. 2158-2172.

160.   Hunter, M., et al., *Subventricular zone lipidomic architecture loss in Huntington's disease.* Journal of Neurochemistry, 2018. **146**(5): p. 613-630.

161.   Maganti, R.J., et al., *Defining Changes in the Spatial Distribution and Composition of Brain Lipids in the Shiverer and Cuprizone Mouse Models of Myelin Disease.* J Histochem Cytochem, 2019. **67**(3): p. 203-219.

162.   Zhu, T., et al., *Anti-ischemia/reperfusion injury effects of notoginsenoside R1 on small molecule metabolism in rat brain after ischemic stroke as visualized by MALDI-MS imaging.* Biomedicine & Pharmacotherapy, 2020. **129**.

163.   de Macedo, C.S., et al., *MALDI imaging reveals lipid changes in the skin of leprosy patients before and after multidrug therapy (MDT).* Journal of Mass Spectrometry, 2015. **50**(12): p. 1374-1385.

164.   Goto-Inoue, N., et al., *Visualization of dynamic change in contraction-induced lipid composition in mouse skeletal muscle by matrix-assisted laser desorption/ionization imaging mass spectrometry.* Anal Bioanal Chem, 2012. **403**(7): p. 1863-71.

165.   Park, E.S., et al., *Phosphatidylcholine Alteration Identified Using MALDI Imaging MS in HBV-Infected Mouse Livers and Virus-Mediated Regeneration Defects.* Plos One, 2014. **9**(8).

166.   Ferreira, M.S., et al., *Mass spectrometry imaging: a new vision in differentiating Schistosoma mansoni strains.* Journal of Mass Spectrometry, 2014. **49**(1): p. 86-92.

167. Tans, R., et al., *Spatially Resolved Immunometabolism to Understand Infectious Disease Progression.* Frontiers in Microbiology, 2021. **12**(2406).

168. Liu, H., et al., *Mass Spectrometry Imaging of Kidney Tissue Sections of Rat Subjected to Unilateral Ureteral Obstruction.* Sci Rep, 2017. **7**: p. 41954.

169. Neumann, E.K., et al., *Spatial Metabolomics of the Human Kidney using MALDI Trapped Ion Mobility Imaging Mass Spectrometry.* Anal Chem, 2020. **92**(19): p. 13084-13091.

170. Sun, C., et al., *Acetone immersion enhanced MALDI-MS imaging of small molecule metabolites in biological tissues.* J Pharm Biomed Anal, 2019. **176**: p. 112797.

171. Zahraei, A., et al., *Mapping glucose metabolites in the normal bovine lens: Evaluation and optimisation of a matrix-assisted laser desorption/ionisation imaging mass spectrometry method.* J Mass Spectrom, 2020. **56**(4): p. e4666.

172. Dekker, T.J., et al., *Towards imaging metabolic pathways in tissues.* Anal Bioanal Chem, 2015. **407**(8): p. 2167-76.

173. Sun, N., et al., *High-Resolution Tissue Mass Spectrometry Imaging Reveals a Refined Functional Anatomy of the Human Adult Adrenal Gland.* Endocrinology, 2018. **159**(3): p. 1511-1524.

174. Murakami, M., et al., *Mass spectrometry imaging identifies metabolic patterns associated with malignant potential in pheochromocytoma and paraganglioma.* Eur J Endocrinol, 2021. **185**(1): p. 179-191.

175. Andersen, M.K., et al., *Spatial differentiation of metabolism in prostate cancer tissue by MALDI-TOF MSI.* Cancer Metab, 2021. **9**(1): p. 9.

176. Cheng, X., et al., *Dynamic Alterations of Brain Injury, Functional Recovery, and Metabolites Profile after Cerebral Ischemia/Reperfusion in Rats Contributes to Potential Biomarkers.* J Mol Neurosci, 2020. **70**(5): p. 667-676.

177. Esteve, C., et al., *Mass spectrometry imaging shows major derangements in neurogranin and in purine metabolism in the triple-knockout 3xTg Alzheimer mouse model.* Biochim Biophys Acta Proteins Proteom, 2017. **1865**(7): p. 747-754.

178. Pinzariu, O., B. Georgescu, and C.E. Georgescu, *Metabolomics-A Promising Approach to Pituitary Adenomas.* Front Endocrinol (Lausanne), 2018. **9**: p. 814.

179. Ucal, Y., et al., *Clinical applications of MALDI imaging technologies in cancer and neurodegenerative diseases.* Biochim Biophys Acta Proteins Proteom, 2017. **1865**(7): p. 795-816.

180. Sun, N., et al., *Prognostic Relevance of Steroid Sulfation in Adrenocortical Carcinoma Revealed by Molecular Phenotyping Using High-Resolution Mass Spectrometry Imaging.* Clin Chem, 2019. **65**(10): p. 1276-1286.

181. Torata, N., et al., *Visualizing Energy Charge in Breast Carcinoma Tissues by MALDI Mass-spectrometry Imaging Profiles of Low-molecular-weight Metabolites.* Anticancer Res, 2018. **38**(7): p. 4267-4272.

182. Zang, Q., et al., *Spatially resolved metabolomics combined with multicellular tumor spheroids to discover cancer tissue relevant metabolic signatures.* Anal Chim Acta, 2021. **1155**: p. 338342.

183. Buck, A., et al., *In Situ Metabolomics in Cancer by Mass Spectrometry Imaging.* Adv Cancer Res, 2017. **134**: p. 117-132.

184. Enomoto, Y., et al., *Mass Spectrometric Imaging of GABA in the Drosophila melanogaster Adult Head.* Anal Sci, 2018. **34**(9): p. 1055-1059.

185. Yang, H., et al., *Organic washes of tissue sections for comprehensive analysis of small molecule metabolites by MALDI MS imaging of rat brain following status epilepticus.* Metabolomics, 2018. **14**(4): p. 50.

186. Rocha, B., et al., *Integrative Metabolic Pathway Analysis Reveals Novel Therapeutic Targets in Osteoarthritis.* Mol Cell Proteomics, 2020. **19**(4): p. 574-588.

187. Andrews, W.T., et al., *In situ metabolite and lipid analysis of GluN2D(-/-) and wild-type mice after ischemic stroke using MALDI MSI.* Anal Bioanal Chem, 2020. **412**(24): p. 6275-6285.

188. Karlsson, O. and J. Hanrieder, *Imaging mass spectrometry in drug development and toxicology.* Arch Toxicol, 2017. **91**(6): p. 2283-2294.

189. Sezgin, S., et al., *Spatio-temporal visualization of the distribution of acetaminophen as well as its metabolites and adducts in mouse livers by MALDI MSI.* Arch Toxicol, 2018. **92**(9): p. 2963-2977.

190. Chen, B., et al., *Combining MALDI mass spectrometry imaging and droplet-base surface sampling analysis for tissue distribution, metabolite profiling, and relative quantification of cyclic peptide melanotan II.* Anal Chim Acta, 2020. **1125**: p. 279-287.

191. Wang, T., et al., *A novel binary matrix consisting of graphene oxide and caffeic acid for the analysis of scutellarin and its metabolites in mouse kidney by MALDI imaging.* Analyst, 2021. **146**(1): p. 289-295.

192. Tian, F., et al., *Effects of Thymoquinone on Small-Molecule Metabolites in a Rat Model of Cerebral Ischemia Reperfusion Injury Assessed using MALDI-MSI.* Metabolites, 2020. **10**(1).

193. Lv, R., et al., *Spatial-temporal profiling of antibiotic metabolites using graphite dots-assisted laser desorption ionization mass spectrometry.* Talanta, 2020. **220**: p. 121371.

194. Barre, F.P.Y., et al., *Enhanced Sensitivity Using MALDI Imaging Coupled with Laser Postionization (MALDI-2) for Pharmaceutical Research.* Anal Chem, 2019. **91**(16): p. 10840-10848.

195. Torok, S., et al., *Localization of sunitinib, its metabolites and its target receptors in tumour-bearing mice: a MALDI-MS imaging study.* Br J Pharmacol, 2015. **172**(4): p. 1148-63.

196. Tang, W., et al., *Quantitative MALDI Imaging of Spatial Distributions and Dynamic Changes of Tetrandrine in Multiple Organs of Rats.* Theranostics, 2019. **9**(4): p. 932-944.

197. Nguyen, H.N., et al., *Novel in situ visualisation of rat intestinal absorption of polyphenols via matrix-assisted laser desorption/ionisation mass spectrometry imaging.* Sci Rep, 2019. **9**(1): p. 3166.

198. Kallback, P., et al., *Cross-validated Matrix-Assisted Laser Desorption/Ionization Mass Spectrometry Imaging Quantitation Protocol for a Pharmaceutical Drug and Its Drug-Target Effects in the Brain Using Time-of-Flight and Fourier Transform Ion Cyclotron Resonance Analyzers.* Anal Chem, 2020. **92**(21): p. 14676-14684.

199. Grove, K.J., et al., *Application of Imaging Mass Spectrometry to Assess Ocular Drug Transit.* SLAS Discov, 2017. **22**(10): p. 1239-1245.

200. Grove, K.J., S. Hoque, and P.J. Rudewicz, *Investigation of amodiaquine localization in liver lobules using matrix-assisted laser desorption/ionization imaging mass spectrometry.* Rapid Commun Mass Spectrom, 2019. **33**(3): p. 252-258.

201. Xu, J., et al., *Function of complement factor H and imaging of small molecules by MALDI-MSI in a methamphetamine behavioral sensitization model.* Behav Brain Res, 2019. **364**: p. 233-244.

202. Liu, X. and A.B. Hummon, *Chemical Imaging of Platinum-Based Drugs and their Metabolites.* Sci Rep, 2016. **6**: p. 38507.

203. Blanc, L., et al., *Visualization of Mycobacterial Biomarkers and Tuberculosis Drugs in Infected Tissue by MALDI-MS Imaging.* Anal Chem, 2018. **90**(10): p. 6275-6282.

204. Yokoi, H., et al., *Development of a detection method for antisense oligonucleotides in mouse kidneys by matrix-assisted laser desorption/ionization imaging mass spectrometry.* Rapid Commun Mass Spectrom, 2018. **32**(23): p. 1984-1990.

205. Nakashima, Y. and M. Setou, *Distribution of Antisense Oligonucleotides in Rat Eyeballs Using MALDI Imaging Mass Spectrometry.* Mass Spectrom (Tokyo), 2018. **7**(1): p. A0070.

206. Liu, X., et al., *MALDI Mass Spectrometry Imaging for Evaluation of Therapeutics in Colorectal Tumor Organoids.* J Am Soc Mass Spectrom, 2018. **29**(3): p. 516-526.

207. Kampa, J.M., et al., *Mass spectrometry imaging reveals lipid upregulation and bile acid changes indicating amitriptyline induced steatosis in a rat model.* Toxicol Lett, 2020. **325**: p. 43-50.

208. Groseclose, M.R. and S. Castellino, *An Investigation into Retigabine (Ezogabine) Associated Dyspigmentation in Rat Eyes by MALDI Imaging Mass Spectrometry.* Chem Res Toxicol, 2019. **32**(2): p. 294-303.

References

209.   Chen, H., X. Zhou, and B. Song, *Toxicokinetics, Tissue Distribution, and Excretion of Dufulin Racemate and Its R (S)-Enantiomers in Rats.* J Agric Food Chem, 2018. **66**(28): p. 7265-7274.

210.   Marxen, E., et al., *Permeability Barriers for Nicotine and Mannitol in Porcine Buccal Mucosa Studied by High-Resolution MALDI Mass Spectrometry Imaging.* Mol Pharm, 2018. **15**(2): p. 519-526.

211.   Flinders, B., et al., *Optimization of Sample Preparation and Instrumental Parameters for the Rapid Analysis of Drugs of Abuse in Hair samples by MALDI-MS/MS Imaging.* J Am Soc Mass Spectrom, 2017. **28**(11): p. 2462-2468.

212.   Castellino, S., et al., *Central nervous system disposition and metabolism of Fosdevirine (GSK2248761), a non-nucleoside reverse transcriptase inhibitor: an LC-MS and Matrix-assisted laser desorption/ionization imaging MS investigation into central nervous system toxicity.* Chem Res Toxicol, 2013. **26**(2): p. 241-51.

213.   Fridjonsdottir, E., et al., *Mass spectrometry imaging identifies abnormally elevated brain l-DOPA levels and extrastriatal monoaminergic dysregulation in l-DOPA-induced dyskinesia.* Sci Adv, 2021. **7**(2).

214.   Gonnet, J., et al., *Mechanisms of innate events during skin reaction following intradermal injection of seasonal influenza vaccine.* J Proteomics, 2020. **216**: p. 103670.

215.   Fulop, A., et al., *New Derivatization Reagent for Detection of free Thiol-groups in Metabolites and Proteins in Matrix-Assisted Laser Desorption/Ionization Mass Spectrometry Imaging.* Anal Chem, 2020. **92**(9): p. 6224-6228.

216.   Sun, C., et al., *On-Tissue Derivatization Strategy for Mass Spectrometry Imaging of Carboxyl-Containing Metabolites in Biological Tissues.* Anal Chem, 2020. **92**(18): p. 12126-12131.

217.   Manier, M.L., et al., *A derivatization and validation strategy for determining the spatial localization of endogenous amine metabolites in tissues using MALDI imaging mass spectrometry.* J Mass Spectrom, 2014. **49**(8): p. 665-73.

218.   Smith, K.W., et al., *Spatial Localization of Vitamin D Metabolites in Mouse Kidney by Mass Spectrometry Imaging.* ACS Omega, 2020. **5**(22): p. 13430-13437.

219.   Harkin, C., et al., *On-tissue chemical derivatization in mass spectrometry imaging.* Mass Spectrom Rev, 2021.

220.   Chokkathukalam, A., et al., *Stable isotope-labeling studies in metabolomics: new insights into structure and dynamics of metabolic networks.* Bioanalysis, 2014. **6**(4): p. 511-24.

221.   Grey, A.C., et al., *Applications of stable isotopes in MALDI imaging: current approaches and an eye on the future.* Anal Bioanal Chem, 2021. **413**(10): p. 2637-2653.

222.   Louie, K.B., et al., *Mass spectrometry imaging for in situ kinetic histochemistry.* Sci Rep, 2013. **3**: p. 1656.

223.   Castro-Perez, J., et al., *In vivo isotopically labeled atherosclerotic aorta plaques in ApoE KO mice and molecular profiling by matrix-assisted laser desorption/ionization mass spectrometric imaging.* Rapid Commun Mass Spectrom, 2014. **28**(22): p. 2471-9.

224.   Ellis, S.R., et al., *Mass spectrometry imaging of phosphatidylcholine metabolism in lungs administered with therapeutic surfactants and isotopic tracers.* J Lipid Res, 2021. **62**: p. 100023.

225.   Yoshinaga, K., et al., *Selective Visualization of Administered Arachidonic and Docosahexaenoic Acids in Brain Using Combination of Simple Stable Isotope-Labeling Technique and Imaging Mass Spectrometry.* Anal Chem, 2020. **92**(13): p. 8685-8690.

226.   Kihara, M., et al., *Visualization of (57)Fe-Labeled Heme Isotopic Fine Structure and Localization of Regions of Erythroblast Maturation in Mouse Spleen by MALDI FTICR-MS Imaging.* J Am Soc Mass Spectrom, 2017. **28**(11): p. 2469-2475.

227.   Lusis, A.J., *Atherosclerosis.* Nature, 2000. **407**(6801): p. 233-41.

228.   Milutinovic, A., D. Suput, and R. Zorc-Pleskovic, *Pathogenesis of atherosclerosis in the tunica intima, media, and adventitia of coronary arteries: An updated review.* Bosn J Basic Med Sci, 2020. **20**(1): p. 21-30.

229. Tinajero, M.G. and A.I. Gotlieb, *Recent Developments in Vascular Adventitial Pathobiology: The Dynamic Adventitia as a Complex Regulator of Vascular Disease.* Am J Pathol, 2020. **190**(3): p. 520-534.

230. Stenmark, K.R., et al., *The adventitia: essential regulator of vascular wall structure and function.* Annu Rev Physiol, 2013. **75**: p. 23-47.

231. Gimbrone, M.A., Jr. and G. Garcia-Cardena, *Endothelial Cell Dysfunction and the Pathobiology of Atherosclerosis.* Circ Res, 2016. **118**(4): p. 620-36.

232. Maguire, E.M., S.W.A. Pearce, and Q. Xiao, *Foam cell formation: A new target for fighting atherosclerosis and cardiovascular disease.* Vascul Pharmacol, 2019. **112**: p. 54-71.

233. Moore, K.J. and I. Tabas, *Macrophages in the pathogenesis of atherosclerosis.* Cell, 2011. **145**(3): p. 341-55.

234. Badimon, L. and G. Vilahur, *Thrombosis formation on atherosclerotic lesions and plaque rupture.* J Intern Med, 2014. **276**(6): p. 618-32.

235. Doran, A.C., N. Meller, and C.A. McNamara, *Role of smooth muscle cells in the initiation and early progression of atherosclerosis.* Arterioscler Thromb Vasc Biol, 2008. **28**(5): p. 812-9.

236. Shi, X., et al., *Calcification in Atherosclerotic Plaque Vulnerability: Friend or Foe?* Front Physiol, 2020. **11**: p. 56.

237. Martin-Lorenzo, M., et al., *Molecular histology of arteries: mass spectrometry imaging as a novel ex vivo tool to investigate atherosclerosis.* Expert Review of Proteomics, 2016. **13**(1): p. 69-81.

238. Mushenkova, N.V., et al., *Modelling of atherosclerosis in genetically modified animals.* Am J Transl Res, 2019. **11**(8): p. 4614-4633.

239. Emini Veseli, B., et al., *Animal models of atherosclerosis.* Eur J Pharmacol, 2017. **816**: p. 3-13.

240. Golforoush, P., D.M. Yellon, and S.M. Davidson, *Mouse models of atherosclerosis and their suitability for the study of myocardial infarction.* Basic Research in Cardiology, 2020. **115**(6).

241. Getz, G.S. and C.A. Reardon, *Do the Apoe-/- and Ldlr-/- Mice Yield the Same Insight on Atherogenesis?* Arterioscler Thromb Vasc Biol, 2016. **36**(9): p. 1734-41.

242. Martin-Lorenzo, M., et al., *Molecular anatomy of ascending aorta in atherosclerosis by MS Imaging: Specific lipid and protein patterns reflect pathology.* Journal of Proteomics, 2015. **126**: p. 245-251.

243. Mezger, S.T.P., et al., *Trends in mass spectrometry imaging for cardiovascular diseases.* Analytical and Bioanalytical Chemistry, 2019. **411**(17): p. 3709-3720.

244. Martin-Lorenzo, M., et al., *30 mu m spatial resolution protein MALDI MSI: In-depth comparison of five sample preparation protocols applied to human healthy and atherosclerotic arteries.* Journal of Proteomics, 2014. **108**: p. 465-468.

245. Patterson, N.H., et al., *Three-dimensional imaging MS of lipids in atherosclerotic plaques: Open-source methods for reconstruction and analysis.* Proteomics, 2016. **16**(11-12): p. 1642-1651.

246. Lohofer, F., et al., *Mass Spectrometry Imaging of atherosclerosis-affine Gadofluorine following Magnetic Resonance Imaging.* Scientific Reports, 2020. **10**(1).

247. Moerman, A.M., et al., *Lipid signature of advanced human carotid atherosclerosis assessed by mass spectrometry imaging.* J Lipid Res, 2021. **62**: p. 100020.

248. Greco, F., et al., *Mass Spectrometry Imaging as a Tool to Investigate Region Specific Lipid Alterations in Symptomatic Human Carotid Atherosclerotic Plaques.* Metabolites, 2021. **11**(4).

249. Velnar, T., T. Bailey, and V. Smrkolj, *The wound healing process: an overview of the cellular and molecular mechanisms.* J Int Med Res, 2009. **37**(5): p. 1528-42.

250. Wilkinson, H.N. and M.J. Hardman, *Wound healing: cellular mechanisms and pathological outcomes.* Open Biol, 2020. **10**(9): p. 200223.

251. Koh, T.J. and L.A. DiPietro, *Inflammation and wound healing: the role of the macrophage.* Expert Rev Mol Med, 2011. **13**: p. e23.

252.   Midwood, K.S., L.V. Williams, and J.E. Schwarzbauer, *Tissue repair and the dynamics of the extracellular matrix.* Int J Biochem Cell Biol, 2004. **36**(6): p. 1031-7.

253.   Rousselle, P., F. Braye, and G. Dayan, *Re-epithelialization of adult skin wounds: Cellular mechanisms and therapeutic strategies.* Adv Drug Deliv Rev, 2019. **146**: p. 344-365.

254.   Darby, I.A., et al., *Fibroblasts and myofibroblasts in wound healing.* Clin Cosmet Investig Dermatol, 2014. **7**: p. 301-11.

255.   Sami, D.G., H.H. Heiba, and A. Abdellatif, *Wound healing models: A systematic review of animal and non-animal models.* Wound Medicine, 2019. **24**(1): p. 8-17.

256.   Pils, V., et al., *The role of lipid-based signalling in wound healing and senescence.* Mech Ageing Dev, 2021. **198**: p. 111527.

257.   Han, G. and R. Ceilley, *Chronic Wound Healing: A Review of Current Management and Treatments.* Adv Ther, 2017. **34**(3): p. 599-610.

258.   Lau, F.H. and B. Pomahac, *Wound healing in acutely injured fascia.* Wound Repair Regen, 2014. **22 Suppl 1**: p. 14-7.

259.   Hart, P.J. and M.R. Clench, *MALDI-MSI of Lipids in Human Skin.* Methods Mol Biol, 2017. **1618**: p. 29-36.

260.   Lewis, E.E.L., et al., *Examination of the skin barrier repair/wound healing process using a living skin equivalent model and matrix-assisted laser desorption-ionization-mass spectrometry imaging.* Int J Cosmet Sci, 2018. **40**(2): p. 148-156.

261.   Komprda, T., et al., *The effect of different fatty acid sources on wound healing in rats assessed by matrix-assisted-laser-desorption-ionization mass-spectroscopy-imaging.* Acta Veterinaria Brno, 2019. **88**(4): p. 443-+.

262.   Franz, M.G., et al., *Fascial incisions heal faster than skin: a new model of abdominal wall repair.* Surgery, 2001. **129**(2): p. 203-8.

263.   Liu, H., et al., *Examination of lipid profiles in abdominal fascial healing using MALDI-TOF to identify potential therapeutic targets.* Journal of Mass Spectrometry and Advances in the Clinical Lab, 2021. **20**: p. 35-41.

264.   Hanahan, D. and R.A. Weinberg, *The hallmarks of cancer.* Cell, 2000. **100**(1): p. 57-70.

265.   Zheng, J., *Energy metabolism of cancer: Glycolysis versus oxidative phosphorylation (Review).* Oncol Lett, 2012. **4**(6): p. 1151-1157.

266.   Cooper, G.M., *The Development and Causes of Cancer*, in *The Cell: A Molecular Approach*. 2000.

267.   Poste, G. and I.J. Fidler, *The pathogenesis of cancer metastasis.* Nature, 1980. **283**(5743): p. 139-46.

268.   Koppenol, W.H., P.L. Bounds, and C.V. Dang, *Otto Warburg's contributions to current concepts of cancer metabolism.* Nat Rev Cancer, 2011. **11**(5): p. 325-37.

269.   Liberti, M.V. and J.W. Locasale, *The Warburg Effect: How Does it Benefit Cancer Cells?* Trends Biochem Sci, 2016. **41**(3): p. 211-218.

270.   Almuhaideb, A., N. Papathanasiou, and J. Bomanji, *18F-FDG PET/CT imaging in oncology.* Ann Saudi Med, 2011. **31**(1): p. 3-13.

271.   Li, T. and A. Le, *Glutamine Metabolism in Cancer.* Adv Exp Med Biol, 2018. **1063**: p. 13-32.

272.   Hensley, C.T., A.T. Wasti, and R.J. DeBerardinis, *Glutamine and cancer: cell biology, physiology, and clinical opportunities.* J Clin Invest, 2013. **123**(9): p. 3678-84.

273.   Venneti, S., et al., *Glutamine-based PET imaging facilitates enhanced metabolic evaluation of gliomas in vivo.* Sci Transl Med, 2015. **7**(274): p. 274ra17.

274.   Marjanovic, N.D., R.A. Weinberg, and C.L. Chaffer, *Cell plasticity and heterogeneity in cancer.* Clin Chem, 2013. **59**(1): p. 168-79.

275.   Martinez-Reyes, I. and N.S. Chandel, *Cancer metabolism: looking forward.* Nat Rev Cancer, 2021.

276.   Kumari, S., et al., *Reactive Oxygen Species: A Key Constituent in Cancer Survival.* Biomark Insights, 2018. **13**: p. 1177271918755391.

277.   Becker, H.M., *Carbonic anhydrase IX and acid transport in cancer.* Br J Cancer, 2020. **122**(2): p. 157-167.

278.   Seth Nanda, C., et al., *Defining a metabolic landscape of tumours: genome meets metabolism.* Br J Cancer, 2020. **122**(2): p. 136-149.

279.   Engelman, J.A., et al., *Effective use of PI3K and MEK inhibitors to treat mutant Kras G12D and PIK3CA H1047R murine lung cancers.* Nat Med, 2008. **14**(12): p. 1351-6.

280.   Cardaci, S., et al., *Pyruvate carboxylation enables growth of SDH-deficient cells by supporting aspartate biosynthesis.* Nat Cell Biol, 2015. **17**(10): p. 1317-26.

281.   Hoang, G., S. Udupa, and A. Le, *Application of metabolomics technologies toward cancer prognosis and therapy.* Int Rev Cell Mol Biol, 2019. **347**: p. 191-223.

282.   Whiteside, T.L., *The tumor microenvironment and its role in promoting tumor growth.* Oncogene, 2008. **27**(45): p. 5904-12.

283.   Schulz, S., et al., *Advanced MALDI mass spectrometry imaging in pharmaceutical research and drug development.* Curr Opin Biotechnol, 2019. **55**: p. 51-59.

284.   Kampa, J.M., et al., *Glioblastoma multiforme: Metabolic differences to peritumoral tissue and IDH-mutated gliomas revealed by mass spectrometry imaging.* Neuropathology, 2020. **40**(6): p. 546-558.

285.   Paine, M.R.L., et al., *Three-Dimensional Mass Spectrometry Imaging Identifies Lipid Markers of Medulloblastoma Metastasis.* Sci Rep, 2019. **9**(1): p. 2205.

286.   Wildburger, N.C., et al., *ESI-MS/MS and MALDI-IMS Localization Reveal Alterations in Phosphatidic Acid, Diacylglycerol, and DHA in Glioma Stem Cell Xenografts.* J Proteome Res, 2015. **14**(6): p. 2511-9.

287.   Zhai, X.H., et al., *Novel sphingomyelin biomarkers for brain glioma and associated regulation research on the PI3K/Akt signaling pathway.* Oncol Lett, 2019. **18**(6): p. 6207-6213.

288.   Zhou, D., et al., *Mass spectrometry imaging of small molecules in biological tissues using graphene oxide as a matrix.* Anal Chim Acta, 2017. **962**: p. 52-59.

289.   Cimino, J., et al., *Towards lipidomics of low-abundant species for exploring tumor heterogeneity guided by high-resolution mass spectrometry imaging.* Int J Mol Sci, 2013. **14**(12): p. 24560-80.

290.   Bien, T., et al., *MALDI-2 Mass Spectrometry and Immunohistochemistry Imaging of Gb3Cer, Gb4Cer, and Further Glycosphingolipids in Human Colorectal Cancer Tissue.* Anal Chem, 2020. **92**(10): p. 7096-7105.

291.   Mas, S., et al., *MALDI imaging mass spectrometry and chemometric tools to discriminate highly similar colorectal cancer tissues.* Talanta, 2020. **208**: p. 120455.

292.   Patterson, N.H., et al., *Assessment of pathological response to therapy using lipid mass spectrometry imaging.* Sci Rep, 2016. **6**: p. 36814.

293.   Blomme, A., et al., *Murine stroma adopts a human-like metabolic phenotype in the PDX model of colorectal cancer and liver metastases.* Oncogene, 2018. **37**(9): p. 1237-1250.

294.   Schmidt, J., et al., *Lipid and protein tumor markers for head and neck squamous cell carcinoma identified by imaging mass spectrometry.* Oncotarget, 2020. **11**(28): p. 2702-2717.

295.   Krasny, L., et al., *Spatial segmentation of MALDI FT-ICR MSI data: a powerful tool to explore the head and neck tumor in situ lipidome.* J Am Soc Mass Spectrom, 2015. **26**(1): p. 36-43.

296.   Rabe, J.H., et al., *Fourier Transform Infrared Microscopy Enables Guidance of Automated Mass Spectrometry Imaging to Predefined Tissue Morphologies.* Sci Rep, 2018. **8**(1): p. 313.

297.   Neumann, J.M., et al., *A new technological approach in diagnostic pathology: mass spectrometry imaging-based metabolomics for biomarker detection in urachal cancer.* Lab Invest, 2021. **101**(9): p. 1281-1288.

References

298.   Bednarczyk, K., et al., *Discrimination of normal oral mucosa from oral cancer by mass spectrometry imaging of proteins and lipids.* J Mol Histol, 2019. **50**(1): p. 1-10.

299.   Uchiyama, Y., et al., *Imaging mass spectrometry distinguished the cancer and stromal regions of oral squamous cell carcinoma by visualizing phosphatidylcholine (16:0/16:1) and phosphatidylcholine (18:1/20:4).* Anal Bioanal Chem, 2014. **406**(5): p. 1307-16.

300.   Prade, V.M., et al., *De novo discovery of metabolic heterogeneity with immunophenotype-guided imaging mass spectrometry.* Mol Metab, 2020. **36**: p. 100953.

301.   Shimma, S., et al., *MALDI-based imaging mass spectrometry revealed abnormal distribution of phospholipids in colon cancer liver metastasis.* J Chromatogr B Analyt Technol Biomed Life Sci, 2007. **855**(1): p. 98-103.

302.   Sun, C., et al., *1,1'-binaphthyl-2,2'-diamine as a novel MALDI matrix to enhance the in situ imaging of metabolic heterogeneity in lung cancer.* Talanta, 2020. **209**: p. 120557.

303.   Kirchberger-Tolstik, T., et al., *Nondestructive molecular imaging by Raman spectroscopy vs. marker detection by MALDI IMS for an early diagnosis of HCC.* Analyst, 2021. **146**(4): p. 1239-1252.

304.   Fernandez, R., et al., *Analysis of the lipidome of xenografts using MALDI-IMS and UHPLC-ESI-QTOF.* J Am Soc Mass Spectrom, 2014. **25**(7): p. 1237-46.

305.   Bregeon, F., et al., *MALDI-ToF mass spectrometry for the rapid diagnosis of cancerous lung nodules.* PLoS One, 2014. **9**(5): p. e97511.

306.   Morita, Y., et al., *Lysophosphatidylcholine acyltransferase 1 altered phospholipid composition and regulated hepatoma progression.* J Hepatol, 2013. **59**(2): p. 292-9.

307.   Ellis, S.R., et al., *More from less: high-throughput dual polarity lipid imaging of biological tissues.* Analyst, 2016. **141**(12): p. 3832-41.

308.   Pirman, D.A., et al., *Changes in cancer cell metabolism revealed by direct sample analysis with MALDI mass spectrometry.* PLoS One, 2013. **8**(4): p. e61379.

309.   Barre, F.P.Y., et al., *Specific Lipid and Metabolic Profiles of R-CHOP-Resistant Diffuse Large B-Cell Lymphoma Elucidated by Matrix-Assisted Laser Desorption Ionization Mass Spectrometry Imaging and in Vivo Imaging.* Anal Chem, 2018. **90**(24): p. 14198-14206.

310.   Guo, S., et al., *Tissue imaging and serum lipidomic profiling for screening potential biomarkers of thyroid tumors by matrix-assisted laser desorption/ionization-Fourier transform ion cyclotron resonance mass spectrometry.* Anal Bioanal Chem, 2014. **406**(18): p. 4357-70.

311.   Drake, R.R., et al., *Defining the human kidney N-glycome in normal and cancer tissues using MALDI imaging mass spectrometry.* J Mass Spectrom, 2020. **55**(4): p. e4490.

312.   Neef, S.K., et al., *Optimized protocol for metabolomic and lipidomic profiling in formalin-fixed paraffin-embedded kidney tissue by LC-MS.* Anal Chim Acta, 2020. **1134**: p. 125-135.

313.   Jirasko, R., et al., *MALDI Orbitrap Mass Spectrometry Profiling of Dysregulated Sulfoglycosphingolipids in Renal Cell Carcinoma Tissues.* J Am Soc Mass Spectrom, 2017. **28**(8): p. 1562-1574.

314.   Hajek, R., et al., *HILIC/ESI-MS determination of gangliosides and other polar lipid classes in renal cell carcinoma and surrounding normal tissues.* Anal Bioanal Chem, 2018. **410**(25): p. 6585-6594.

315.   Tu, A., N. Said, and D.C. Muddiman, *Spatially resolved metabolomic characterization of muscle invasive bladder cancer by mass spectrometry imaging.* Metabolomics, 2021. **17**(8): p. 70.

316.   Briggs, M.T., et al., *MALDI Mass Spectrometry Imaging of Early- and Late-Stage Serous Ovarian Cancer Tissue Reveals Stage-Specific N-Glycans.* Proteomics, 2019. **19**(21-22): p. e1800482.

317.   Steurer, S., et al., *MALDI mass spectrometric imaging based identification of clinically relevant signals in prostate cancer using large-scale tissue microarrays.* Int J Cancer, 2013. **133**(4): p. 920-8.

318.   Lou, S., et al., *Prognostic Metabolite Biomarkers for Soft Tissue Sarcomas Discovered by Mass Spectrometry Imaging.* J Am Soc Mass Spectrom, 2017. **28**(2): p. 376-383.

319. Acland, M., et al., *Mass Spectrometry Analyses of Multicellular Tumor Spheroids.* Proteomics Clin Appl, 2018. **12**(3): p. e1700124.

320. Tucker, L.H., et al., *Untargeted Metabolite Mapping in 3D Cell Culture Models Using High Spectral Resolution FT-ICR Mass Spectrometry Imaging.* Anal Chem, 2019. **91**(15): p. 9522-9529.

321. Mascini, N.E., et al., *Tumor classification with MALDI-MSI data of tissue microarrays: A case study.* Methods, 2018. **151**: p. 21-27.

322. Hinsch, A., et al., *MALDI imaging mass spectrometry reveals multiple clinically relevant masses in colorectal cancer using large-scale tissue microarrays.* J Mass Spectrom, 2017. **52**(3): p. 165-173.

323. Buck, A., et al., *Distribution and quantification of irinotecan and its active metabolite SN-38 in colon cancer murine model systems using MALDI MSI.* Anal Bioanal Chem, 2015. **407**(8): p. 2107-16.

324. Giordano, S., et al., *Heterogeneity of paclitaxel distribution in different tumor models assessed by MALDI mass spectrometry imaging.* Sci Rep, 2016. **6**: p. 39284.

325. Bianga, J., et al., *Complementarity of MALDI and LA ICP mass spectrometry for platinum anticancer imaging in human tumor.* Metallomics, 2014. **6**(8): p. 1382-6.

326. Huber, K., et al., *Novel approach of MALDI drug imaging, immunohistochemistry, and digital image analysis for drug distribution studies in tissues.* Anal Chem, 2014. **86**(21): p. 10568-75.

327. Tsubata, Y., et al., *Evaluation of the heterogeneous tissue distribution of erlotinib in lung cancer using matrix-assisted laser desorption ionization mass spectrometry imaging.* Sci Rep, 2017. **7**(1): p. 12622.

328. Connell, J.J., et al., *Localization of sunitinib in in vivo animal and in vitro experimental models by MALDI mass spectrometry imaging.* Anal Bioanal Chem, 2015. **407**(8): p. 2245-53.

329. Fuchs, K., et al., *Mapping of drug distribution in the rabbit liver tumor model by complementary fluorescence and mass spectrometry imaging.* J Control Release, 2018. **269**: p. 128-135.

330. Ryu, S., et al., *Visualization of the distribution of nanoparticle-formulated AZD2811 in mouse tumor model using matrix-assisted laser desorption ionization mass spectrometry imaging.* Sci Rep, 2020. **10**(1): p. 15535.

331. Mascini, N.E., et al., *Mass Spectrometry Imaging of the Hypoxia Marker Pimonidazole in a Breast Tumor Model.* Anal Chem, 2016. **88**(6): p. 3107-14.

332. Wang, Y. and A.B. Hummon, *Mass spectrometry imaging of multicellular tumor spheroids and organoids as an emerging tool for personalized medicine and drug discovery.* J Biol Chem, 2021: p. 101139.

333. Libby, P., *Inflammation in atherosclerosis.* Arterioscler Thromb Vasc Biol, 2012. **32**(9): p. 2045-51.

334. Mezger, S.T.P., et al., *Trends in mass spectrometry imaging for cardiovascular diseases.* Anal Bioanal Chem, 2019. **411**(17): p. 3709-3720.

335. Martin-Lorenzo, M., et al., *30mum spatial resolution protein MALDI MSI: In-depth comparison of five sample preparation protocols applied to human healthy and atherosclerotic arteries.* J Proteomics, 2014. **108**: p. 465-8.

336. Patterson, N.H., et al., *Three-dimensional imaging MS of lipids in atherosclerotic plaques: Open-source methods for reconstruction and analysis.* Proteomics, 2016. **16**(11-12): p. 1642-51.

337. Visscher, M., et al., *Data Processing Pipeline for Lipid Profiling of Carotid Atherosclerotic Plaque with Mass Spectrometry Imaging.* J Am Soc Mass Spectrom, 2019. **30**(9): p. 1790-1800.

338. Zaima, N., et al., *Imaging mass spectrometry-based histopathologic examination of atherosclerotic lesions.* Atherosclerosis, 2011. **217**(2): p. 427-32.

339. Martin-Lorenzo, M., et al., *Molecular histology of arteries: mass spectrometry imaging as a novel ex vivo tool to investigate atherosclerosis.* Expert Rev Proteomics, 2016. **13**(1): p. 69-81.

340. Diehl, P., et al., *Lysophosphatidylcholine is a Major Component of Platelet Microvesicles Promoting Platelet Activation and Reporting Atherosclerotic Plaque Instability.* Thromb Haemost, 2019. **119**(8): p. 1295-1310.

341.   Li, Y.F., et al., *Lysophospholipids and their G protein-coupled receptors in atherosclerosis.* Front Biosci (Landmark Ed), 2016. **21**: p. 70-88.

342.   Schmitz, G. and K. Ruebsaamen, *Metabolism and atherogenic disease association of lysophosphatidylcholine.* Atherosclerosis, 2010. **208**(1): p. 10-8.

343.   Wurtz, P., et al., *Metabolite profiling and cardiovascular event risk: a prospective study of 3 population-based cohorts.* Circulation, 2015. **131**(9): p. 774-85.

344.   Kohno, S., et al., *Lipidomic insight into cardiovascular diseases.* Biochem Biophys Res Commun, 2018. **504**(3): p. 590-595.

345.   Stegemann, C., et al., *Lipidomics profiling and risk of cardiovascular disease in the prospective population-based Bruneck study.* Circulation, 2014. **129**(18): p. 1821-31.

346.   Djekic, D., et al., *Serum untargeted lipidomic profiling reveals dysfunction of phospholipid metabolism in subclinical coronary artery disease.* Vasc Health Risk Manag, 2019. **15**: p. 123-135.

347.   Ward-Caviness, C.K., et al., *Improvement of myocardial infarction risk prediction via inflammation-associated metabolite biomarkers.* Heart, 2017. **103**(16): p. 1278-1285.

348.   Bot, M., et al., *Lysophosphatidic acid triggers mast cell-driven atherosclerotic plaque destabilization by increasing vascular inflammation.* J Lipid Res, 2013. **54**(5): p. 1265-74.

349.   Bot, M., et al., *Atherosclerotic lesion progression changes lysophosphatidic acid homeostasis to favor its accumulation.* Am J Pathol, 2010. **176**(6): p. 3073-84.

350.   Kurano, M., et al., *Possible involvement of minor lysophospholipids in the increase in plasma lysophosphatidic acid in acute coronary syndrome.* Arterioscler Thromb Vasc Biol, 2015. **35**(2): p. 463-70.

351.   Spector, A.A., *Plaque rupture, lysophosphatidic acid, and thrombosis.* Circulation, 2003. **108**(6): p. 641-3.

352.   Bot, M., et al., *Lysophospholipids: two-faced mediators in atherosclerosis.* Future Lipidology, 2007. **2**(3): p. 341-356.

353.   Robertson-Gray, O.J., et al., *l-alpha-Lysophosphatidylinositol (LPI) aggravates myocardial ischemia/reperfusion injury via a GPR55/ROCK-dependent pathway.* Pharmacol Res Perspect, 2019. **7**(3): p. e00487.

354.   Kikuchi-Yanoshita, R., et al., *Preferential hydrolysis of phosphatidylethanolamine in rat ischemic heart homogenates during in vitro incubation.* J Biochem, 1993. **114**(1): p. 33-8.

355.   Law, S.H., et al., *An Updated Review of Lysophosphatidylcholine Metabolism in Human Diseases.* Int J Mol Sci, 2019. **20**(5).

356.   Lehti, S., et al., *Spatial distributions of lipids in atherosclerosis of human coronary arteries studied by time-of-flight secondary ion mass spectrometry.* Am J Pathol, 2015. **185**(5): p. 1216-33.

357.   Schlitt, A., et al., *Further evaluation of plasma sphingomyelin levels as a risk factor for coronary artery disease.* Nutr Metab (Lond), 2006. **3**: p. 5.

358.   Jiang, X.C., et al., *Plasma sphingomyelin level as a risk factor for coronary artery disease.* Arterioscler Thromb Vasc Biol, 2000. **20**(12): p. 2614-8.

359.   Li, Z., et al., *The effect of dietary sphingolipids on plasma sphingomyelin metabolism and atherosclerosis.* Biochim Biophys Acta, 2005. **1735**(2): p. 130-4.

360.   Cao, J.H., et al., *Atheroma-Specific Lipids in ldlr(-/-) and apoe(-/-) Mice Using 2D and 3D Matrix-Assisted Laser Desorption/Ionization Mass Spectrometry Imaging.* Journal of the American Society for Mass Spectrometry, 2020. **31**(9): p. 1825-1832.

361.   Libby, P., P.M. Ridker, and G.K. Hansson, *Progress and challenges in translating the biology of atherosclerosis.* Nature, 2011. **473**(7347): p. 317-325.

362.   Iliou, A., et al., *Metabolic phenotyping and cardiovascular disease: an overview of evidence from epidemiological settings.* Heart, 2021. **107**(14): p. 1123-1129.

363. Ussher, J.R., et al., *The Emerging Role of Metabolomics in the Diagnosis and Prognosis of Cardiovascular Disease.* J Am Coll Cardiol, 2016. **68**(25): p. 2850-2870.

364. Vorkas, P.A., et al., *Untargeted UPLC-MS profiling pipeline to expand tissue metabolome coverage: application to cardiovascular disease.* Anal Chem, 2015. **87**(8): p. 4184-93.

365. Jung, S., et al., *Metabolic phenotyping of human atherosclerotic plaques: Metabolic alterations and their biological relevance in plaque-containing aorta.* Atherosclerosis, 2018. **269**: p. 21-28.

366. Vorkas, P.A., et al., *Metabolic Phenotyping of Atherosclerotic Plaques Reveals Latent Associations between Free Cholesterol and Ceramide Metabolism in Atherogenesis.* Journal of Proteome Research, 2015. **14**(3): p. 1389-1399.

367. Mayr, M., et al., *Proteomics, metabolomics, and immunomics on microparticles derived from human atherosclerotic plaques.* Circ Cardiovasc Genet, 2009. **2**(4): p. 379-88.

368. Martin-Lorenzo, M., et al., *Cytoskeleton deregulation and impairment in amino acids and energy metabolism in early atherosclerosis at aortic tissue with reflection in plasma.* Biochimica Et Biophysica Acta-Molecular Basis of Disease, 2016. **1862**(4): p. 725-732.

369. Chughtai, K. and R.M.A. Heeren, *Mass Spectrometric Imaging for Biomedical Tissue Analysis.* Chemical Reviews, 2010. **110**(5): p. 3237-3277.

370. Martin-Lorenzo, M., et al., *KLK1 and ZG16B proteins and arginine-proline metabolism identified as novel targets to monitor atherosclerosis, acute coronary syndrome and recovery (vol 11, 1056, 2015).* Metabolomics, 2016. **12**(12).

371. Barre, F., et al., *Faster raster matrix-assisted laser desorption/ionization mass spectrometry imaging of lipids at high lateral resolution.* International Journal of Mass Spectrometry, 2019. **437**: p. 38-48.

372. Tan, B., et al., *Identification of endogenous acyl amino acids based on a targeted lipidomics approach.* J Lipid Res, 2010. **51**(1): p. 112-9.

373. Tomczyk, M.M. and V.W. Dolinsky, *The Cardiac Lipidome in Models of Cardiovascular Disease.* Metabolites, 2020. **10**(6).

374. Houslay, M.D., M. Sullivan, and G.B. Bolger, *The multienzyme PDE4 cyclic adenosine monophosphate-specific phosphodiesterase family: intracellular targeting, regulation, and selective inhibition by compounds exerting anti-inflammatory and antidepressant actions.* Adv Pharmacol, 1998. **44**: p. 225-342.

375. Nie, J., et al., *A novel function of the human CLS1 in phosphatidylglycerol synthesis and remodeling.* Biochim Biophys Acta, 2010. **1801**(4): p. 438-45.

376. Zhang, J., et al., *Mitochondrial phosphatase PTPMT1 is essential for cardiolipin biosynthesis.* Cell Metab, 2011. **13**(6): p. 690-700.

377. Stanacev, N.Z., Y.Y. Chang, and E.P. Kennedy, *Biosynthesis of cardiolipin in Escherichia coli.* J Biol Chem, 1967. **242**(12): p. 3018-9.

378. Paradies, G., et al., *Role of Cardiolipin in Mitochondrial Function and Dynamics in Health and Disease: Molecular and Pharmacological Aspects.* Cells, 2019. **8**(7).

379. Schulze, P.C., K. Drosatos, and I.J. Goldberg, *Lipid Use and Misuse by the Heart.* Circ Res, 2016. **118**(11): p. 1736-51.

380. Jennings, W. and R.M. Epand, *CDP-diacylglycerol, a critical intermediate in lipid metabolism.* Chem Phys Lipids, 2020. **230**: p. 104914.

381. Libby, P. and G.K. Hansson, *From Focal Lipid Storage to Systemic Inflammation: JACC Review Topic of the Week.* J Am Coll Cardiol, 2019. **74**(12): p. 1594-1607.

382. Dang, V.T., et al., *Comprehensive Plasma Metabolomic Analyses of Atherosclerotic Progression Reveal Alterations in Glycerophospholipid and Sphingolipid Metabolism in Apolipoprotein E-deficient Mice.* Scientific Reports, 2016. **6**.

References

383.   Ahsan, F., et al., *Targeting to macrophages: role of physicochemical properties of particulate carriers--liposomes and microspheres--on the phagocytosis by macrophages.* J Control Release, 2002. **79**(1-3): p. 29-40.

384.   Fidler, I.J., et al., *Design of liposomes to improve delivery of macrophage-augmenting agents to alveolar macrophages.* Cancer Res, 1980. **40**(12): p. 4460-6.

385.   Stegemann, C., et al., *Comparative lipidomics profiling of human atherosclerotic plaques.* Circ Cardiovasc Genet, 2011. **4**(3): p. 232-42.

386.   Nelson, J.C., et al., *Plasma sphingomyelin and subclinical atherosclerosis: findings from the multi-ethnic study of atherosclerosis.* Am J Epidemiol, 2006. **163**(10): p. 903-12.

387.   Chatterjee, S., *Sphingolipids in atherosclerosis and vascular biology.* Arterioscler Thromb Vasc Biol, 1998. **18**(10): p. 1523-33.

388.   Schlitt, A., et al., *Further evaluation of plasma sphingomyelin levels as a risk factor for coronary artery disease.* Nutrition & Metabolism, 2006. **3**.

389.   Jiang, X.C., et al., *Plasma sphingomyelin level as a risk factor for coronary artery disease.* Arteriosclerosis Thrombosis and Vascular Biology, 2000. **20**(12): p. 2614-2618.

390.   Wang, Z.N., et al., *Gut flora metabolism of phosphatidylcholine promotes cardiovascular disease.* Nature, 2011. **472**(7341): p. 57-U82.

391.   Strott, C.A. and Y. Higashi, *Cholesterol sulfate in human physiology: what's it all about?* J Lipid Res, 2003. **44**(7): p. 1268-78.

392.   Merten, M., et al., *Cholesterol sulfate: a new adhesive molecule for platelets.* Circulation, 2001. **103**(16): p. 2032-4.

393.   Badimon, L., T. Padro, and G. Vilahur, *Atherosclerosis, platelets and thrombosis in acute ischaemic heart disease.* Eur Heart J Acute Cardiovasc Care, 2012. **1**(1): p. 60-74.

394.   Seneff, S., et al., *A novel hypothesis for atherosclerosis as a cholesterol sulfate deficiency syndrome.* Theor Biol Med Model, 2015. **12**: p. 9.

395.   Koeth, R.A., et al., *Intestinal microbiota metabolism of L-carnitine, a nutrient in red meat, promotes atherosclerosis.* Nat Med, 2013. **19**(5): p. 576-85.

396.   Backhed, F., *Meat-metabolizing bacteria in atherosclerosis.* Nat Med, 2013. **19**(5): p. 533-4.

397.   Wang, C., M. Wang, and X. Han, *Applications of mass spectrometry for cellular lipid analysis.* Mol Biosyst, 2015. **11**(3): p. 698-713.

398.   Kohler, A., et al., *Effectiveness of Prophylactic Intraperitoneal Mesh Implantation for Prevention of Incisional Hernia in Patients Undergoing Open Abdominal Surgery: A Randomized Clinical Trial.* JAMA Surg, 2019. **154**(2): p. 109-115.

399.   Jairam, A.P., et al., *Prevention of incisional hernia with prophylactic onlay and sublay mesh reinforcement versus primary suture only in midline laparotomies (PRIMA): 2-year follow-up of a multicentre, double-blind, randomised controlled trial.* Lancet, 2017. **390**(10094): p. 567-576.

400.   Xing, L.Y., et al., *Early laparotomy wound failure as the mechanism for incisional hernia formation.* Journal of Surgical Research, 2013. **182**(1): p. E35-E42.

401.   Bosanquet, D.C., et al., *Systematic Review and Meta-Regression of Factors Affecting Midline Incisional Hernia Rates: Analysis of 14,618 Patients.* PLoS One, 2015. **10**(9): p. e0138745.

402.   Gillion, J.F., et al., *The economic burden of incisional ventral hernia repair: a multicentric cost analysis.* Hernia, 2016. **20**(6): p. 819-830.

403.   Poulose, B.K., et al., *Epidemiology and cost of ventral hernia repair: making the case for hernia research.* Hernia, 2012. **16**(2): p. 179-183.

404.   Kumka, M. and J. Bonar, *Fascia: a morphological description and classification system based on a literature review.* J Can Chiropr Assoc, 2012. **56**(3): p. 179-91.

405.   Franz, M.G., et al., *Fascial incisions heal faster than skin: A new model of abdominal wall repair.* Surgery, 2001. **129**(2): p. 203-208.

406.   Dubay, D.A., et al., *Fascial fibroblast kinetic activity is increased during abdominal wall repair compared to dermal fibroblasts.* Wound Repair and Regeneration, 2004. **12**(5): p. 539-545.

407.   Lemonnier, F., et al., *Some metabolic differences between human skin and aponeurosis fibroblasts in culture.* J Cell Physiol, 1980. **104**(3): p. 415-23.

408.   Muysoms, F.E., et al., *European Hernia Society guidelines on the closure of abdominal wall incisions.* Hernia, 2015. **19**(1): p. 1-24.

409.   Diener, M.K., et al., *Elective midline laparotomy closure: the INLINE systematic review and meta-analysis.* Ann Surg, 2010. **251**(5): p. 843-56.

410.   Santos, A.L. and G. Preta, *Lipids in the cell: organisation regulates function.* Cellular and Molecular Life Sciences, 2018. **75**(11): p. 1909-1927.

411.   Muro, E., G.E. Atilla-Gokcumen, and U.S. Eggert, *Lipids in cell biology: how can we understand them better?* Mol Biol Cell, 2014. **25**(12): p. 1819-23.

412.   Vaughan, E.M., et al., *Lipid domain-dependent regulation of single-cell wound repair.* Mol Biol Cell, 2014. **25**(12): p. 1867-76.

413.   Demoyer, J.S., T.C. Skalak, and M.E. Durieux, *Lysophosphatidic acid enhances healing of acute cutaneous wounds in the mouse.* Wound Repair Regen, 2000. **8**(6): p. 530-7.

414.   Oh, S.Y., et al., *Arachidonic acid promotes skin wound healing through induction of human MSC migration by MT3-MMP-mediated fibronectin degradation.* Cell Death & Disease, 2015. **6**.

415.   Dhall, S., et al., *Arachidonic acid-derived signaling lipids and functions in impaired healing.* Wound Repair and Regeneration, 2015. **23**(5): p. 644-656.

416.   Wijesinghe, D.S. and C.E. Chalfant, *Systems-Level Lipid Analysis Methodologies for Qualitative and Quantitative Investigation of Lipid Signaling Events During Wound Healing.* Adv Wound Care (New Rochelle), 2013. **2**(9): p. 538-548.

417.   Leopold, J., et al., *Recent Developments of Useful MALDI Matrices for the Mass Spectrometric Characterization of Lipids.* Biomolecules, 2018. **8**(4).

418.   Cerruti, C.D., et al., *MALDI imaging mass spectrometry of lipids by adding lithium salts to the matrix solution.* Anal Bioanal Chem, 2011. **401**(1): p. 75-87.

419.   Schiller, J., et al., *Matrix-assisted laser desorption and ionization time-of-flight (MALDI-TOF) mass spectrometry in lipid and phospholipid research.* Prog Lipid Res, 2004. **43**(5): p. 449-88.

420.   Lewis, E.E.L., et al., *Examination of the skin barrier repair/wound healing process using a living skin equivalent model and matrix-assisted laser desorption-ionization-mass spectrometry imaging.* International Journal of Cosmetic Science, 2018. **40**(2): p. 148-156.

421.   Occleston, N.L., et al., *Therapeutic improvement of scarring: mechanisms of scarless and scar-forming healing and approaches to the discovery of new treatments.* Dermatol Res Pract, 2010. **2010**.

422.   Zugel, M., et al., *Fascial tissue research in sports medicine: from molecules to tissue adaptation, injury and diagnostics: consensus statement.* Br J Sports Med, 2018. **52**(23): p. 1497.

423.   Franz, M.G., *The biology of hernia formation.* Surg Clin North Am, 2008. **88**(1): p. 1-15, vii.

424.   Vogels, R.R.M., et al., *Critical overview of all available animal models for abdominal wall hernia research.* Hernia, 2017. **21**(5): p. 667-675.

425.   Velnar, T., T. Bailey, and V. Smrkoli, *The Wound Healing Process: an Overview of the Cellular and Molecular Mechanisms.* Journal of International Medical Research, 2009. **37**(5): p. 1528-1542.

426.   Childs, D.R. and A.S. Murthy, *Overview of Wound Healing and Management.* Surgical Clinics of North America, 2017. **97**(1): p. 189-+.

427.   Werner, S. and R. Grose, *Regulation of wound healing by growth factors and cytokines.* Physiological Reviews, 2003. **83**(3): p. 835-870.

428. Barrientos, S., et al., *Growth factors and cytokines in wound healing.* Wound Repair and Regeneration, 2008. **16**(5): p. 585-601.

429. Ridiandries, A., J.T.M. Tan, and C.A. Bursill, *The Role of Chemokines in Wound Healing.* International Journal of Molecular Sciences, 2018. **19**(10).

430. Gharaee-Kermani, M. and S.H. Phan, *Role of cytokines and cytokine therapy in wound healing and fibrotic diseases.* Current Pharmaceutical Design, 2001. **7**(11): p. 1083-1103.

431. Balazs, L., et al., *Topical application of the phospholipid growth factor lysophosphatidic acid promotes wound healing in vivo.* American Journal of Physiology-Regulatory Integrative and Comparative Physiology, 2001. **280**(2): p. R466-R472.

432. Shea, B.S. and A.M. Tager, *Sphingolipid regulation of tissue fibrosis.* Open Rheumatol J, 2012. **6**: p. 123-9.

433. Yasukawa, K., T. Okuno, and T. Yokomizo, *Eicosanoids in Skin Wound Healing.* Int J Mol Sci, 2020. **21**(22).

434. Jiang, D., et al., *Injury triggers fascia fibroblast collective cell migration to drive scar formation through N-cadherin.* Nat Commun, 2020. **11**(1): p. 5653.

435. Serhan, C.N., et al., *Lipid mediators in the resolution of inflammation.* Cold Spring Harb Perspect Biol, 2014. **7**(2): p. a016311.

436. Kanno, K., et al., *Structure and function of phosphatidylcholine transfer protein (PC-TP)/StarD2.* Biochim Biophys Acta, 2007. **1771**(6): p. 654-62.

437. Li, Z. and D.E. Vance, *Phosphatidylcholine and choline homeostasis.* J Lipid Res, 2008. **49**(6): p. 1187-94.

438. Calzada, E., O. Onguka, and S.M. Claypool, *Phosphatidylethanolamine Metabolism in Health and Disease.* Int Rev Cell Mol Biol, 2016. **321**: p. 29-88.

439. Sohlenkamp, C., I.M. Lopez-Lara, and O. Geiger, *Biosynthesis of phosphatidylcholine in bacteria.* Prog Lipid Res, 2003. **42**(2): p. 115-62.

440. van der Veen, J.N., et al., *The critical role of phosphatidylcholine and phosphatidylethanolamine metabolism in health and disease.* Biochim Biophys Acta Biomembr, 2017. **1859**(9 Pt B): p. 1558-1572.

441. Antonelli, E., V. Villanacci, and G. Bassotti, *Novel oral-targeted therapies for mucosal healing in ulcerative colitis.* World J Gastroenterol, 2018. **24**(47): p. 5322-5330.

442. Karner, M., et al., *First multicenter study of modified release phosphatidylcholine "LT-02" in ulcerative colitis: a randomized, placebo-controlled trial in mesalazine-refractory courses.* Am J Gastroenterol, 2014. **109**(7): p. 1041-51.

443. Kornilova, Z.K., A.A. Selishcheva, and M.I. Perel'man, *Effect of phosphatidylcholine liposome on regeneration of surgical wound in guinea pig lung.* Bull Exp Biol Med, 2001. **131**(2): p. 191-4.

444. Li, J., et al., *A review on phospholipids and their main applications in drug delivery systems.* Asian Journal of Pharmaceutical Sciences, 2015. **10**(2): p. 81-98.

445. desJardins-Park, H.E., D.S. Foster, and M.T. Longaker, *Fibroblasts and wound healing: an update.* Regenerative Medicine, 2018. **13**(5): p. 491-495.

446. Qu, X.L., et al., *Resolvins E1 and D1 inhibit interstitial fibrosis in the obstructed kidney via inhibition of local fibroblast proliferation.* Journal of Pathology, 2012. **228**(4): p. 506-519.

447. Mkrtschjan, M.A., et al., *Lipid signaling affects primary fibroblast collective migration and anchorage in response to stiffness and microtopography.* Journal of Cellular Physiology, 2018. **233**(4): p. 3672-3683.

448. Frisz, J.F., et al., *Direct chemical evidence for sphingolipid domains in the plasma membranes of fibroblasts.* Proceedings of the National Academy of Sciences of the United States of America, 2013. **110**(8): p. E613-E622.

449.   Kraft, M.L., *Sphingolipid Organization in the Plasma Membrane and the Mechanisms That Influence It.* Frontiers in Cell and Developmental Biology, 2017. **4**.

450.   Oga, T., et al., *Prostaglandin F(2alpha) receptor signaling facilitates bleomycin-induced pulmonary fibrosis independently of transforming growth factor-beta.* Nat Med, 2009. **15**(12): p. 1426-30.

451.   Yao, C.H., et al., *Exogenous Fatty Acids Are the Preferred Source of Membrane Lipids in Proliferating Fibroblasts.* Cell Chemical Biology, 2016. **23**(4): p. 483-493.

452.   Zheng, C.P., et al., *Design, synthesis and biological evaluation of new ganglioside GM3 analogues as potential agents for cancer therapy.* European Journal of Medicinal Chemistry, 2020. **189**.

453.   Dam, D.H.M. and A.S. Paller, *Gangliosides in Diabetic Wound Healing.* Gangliosides in Health and Disease, 2018. **156**: p. 229-239.

454.   Wang, X.Q., et al., *Ganglioside GM3 Depletion Reverses Impaired Wound Healing in Diabetic Mice by Activating IGF-1 and Insulin Receptors.* Journal of Investigative Dermatology, 2014. **134**(5): p. 1446-1455.

455.   van den Hil, L.C.L., et al., *Comparability of histological outcomes in rats and humans in a hernia model.* Journal of Surgical Research, 2018. **229**: p. 271-276.

456.   Warburg, O., F. Wind, and E. Negelein, *The Metabolism of Tumors in the Body.* J Gen Physiol, 1927. **8**(6): p. 519-30.

457.   Cluntun, A.A., et al., *Glutamine Metabolism in Cancer: Understanding the Heterogeneity.* Trends Cancer, 2017. **3**(3): p. 169-180.

458.   Mitruka, M., et al., *Undetectable Free Aromatic Amino Acids in Nails of Breast Carcinoma: Biomarker Discovery by a Novel Metabolite Purification VTGE System.* Front Oncol, 2020. **10**: p. 908.

459.   Cai, Y., et al., *Tumor Tissue-Specific Biomarkers of Colorectal Cancer by Anatomic Location and Stage.* Metabolites, 2020. **10**(6).

460.   Tsai, C.K., et al., *Nuclear Magnetic Resonance Metabolomics Biomarkers for Identifying High Risk Patients with Extranodal Extension in Oral Squamous Cell Carcinoma.* J Clin Med, 2020. **9**(4).

461.   Wang, C.Y., et al., *Gene signatures and potential therapeutic targets of amino acid metabolism in estrogen receptor-positive breast cancer.* Am J Cancer Res, 2020. **10**(1): p. 95-113.

462.   Ijare, O.B., et al., *Elevated levels of circulating betahydroxybutyrate in pituitary tumor patients may differentiate prolactinomas from other immunohistochemical subtypes.* Scientific Reports, 2020. **10**(1).

463.   Zhang, M.X., et al., *A pilot investigation of a urinary metabolic biomarker discovery in renal cell carcinoma.* International Urology and Nephrology, 2020. **52**(3): p. 437-446.

464.   Lautaoja, J.H., et al., *Muscle and serum metabolomes are dysregulated in colon-26 tumor-bearing mice despite amelioration of cachexia with activin receptor type 2B ligand blockade.* American Journal of Physiology-Endocrinology and Metabolism, 2019. **316**(5): p. E852-E865.

465.   Loras, A., et al., *Bladder cancer recurrence surveillance by urine metabolomics analysis.* Scientific Reports, 2018. **8**.

466.   Duskova, K., et al., *Differences in Urinary Amino Acid Patterns in Individuals with Different Types of Urological Tumor Urinary Amino Acid Patterns as Markers of Urological Tumors.* In Vivo, 2018. **32**(2): p. 425-429.

467.   Neurauter, G., et al., *Serum phenylalanine concentrations in patients with ovarian carcinoma correlate with concentrations of immune activation markers and of isoprostane-8.* Cancer Letters, 2008. **272**(1): p. 141-147.

468.   Matthews, D.E., *An overview of phenylalanine and tyrosine kinetics in humans.* Journal of Nutrition, 2007. **137**(6): p. 1549s-1555s.

469.   Damink, S.W.M.O., et al., *Isoleucine infusion during "simulated" upper gastrointestinal bleeding improves liver and muscle protein synthesis in cirrhotic patients.* Hepatology, 2007. **45**(3): p. 560-568.

470. Groen, B.B.L., et al., *Post-Prandial Protein Handling: You Are What You Just Ate.* Plos One, 2015. **10**(11).

471. Safaei, A., et al., *Metabolomic analysis of human cirrhosis, hepatocellular carcinoma, non-alcoholic fatty liver disease and non-alcoholic steatohepatitis diseases.* Gastroenterol Hepatol Bed Bench, 2016. **9**(3): p. 158-73.

472. Bedard, P.L., et al., *Tumour heterogeneity in the clinic.* Nature, 2013. **501**(7467): p. 355-64.

473. Dagogo-Jack, I. and A.T. Shaw, *Tumour heterogeneity and resistance to cancer therapies.* Nat Rev Clin Oncol, 2018. **15**(2): p. 81-94.

474. Berger, M.F. and E.R. Mardis, *The emerging clinical relevance of genomics in cancer medicine.* Nat Rev Clin Oncol, 2018. **15**(6): p. 353-365.

475. Zhang, Y., et al., *Imaging Mass Spectrometry Reveals Tumor Metabolic Heterogeneity.* iScience, 2020. **23**(8): p. 101355.

476. van Eijk, H.M.H., et al., *High sensitivity measurement of amino acid isotope enrichment using liquid chromatography-mass spectrometry.* Journal of Chromatography B-Analytical Technologies in the Biomedical and Life Sciences, 2012. **905**: p. 31-36.

477. Koopman, R., et al., *Ingestion of a protein hydrolysate is accompanied by an accelerated in vivo digestion and absorption rate when compared with its intact protein.* American Journal of Clinical Nutrition, 2009. **90**(1): p. 106-115.

478. Furuya, M., et al., *Pathophysiology of tumor neovascularization.* Vasc Health Risk Manag, 2005. **1**(4): p. 277-90.

479. Smith, A.J., *Guidelines for planning and conducting high-quality research and testing on animals.* Lab Anim Res, 2020. **36**: p. 21.

480. Tapia-Vieyra, J.V., B. Delgado-Coello, and J. Mas-Oliva, *Atherosclerosis and Cancer; A Resemblance with Far-reaching Implications.* Arch Med Res, 2017. **48**(1): p. 12-26.

481. Lindholm, C. and R. Searle, *Wound management for the 21st century: combining effectiveness and efficiency.* Int Wound J, 2016. **13 Suppl 2**: p. 5-15.

482. Sen, C.K., et al., *Human skin wounds: a major and snowballing threat to public health and the economy.* Wound Repair Regen, 2009. **17**(6): p. 763-71.

483. Buck, A., et al., *High-resolution MALDI-FT-ICR MS imaging for the analysis of metabolites from formalin-fixed, paraffin-embedded clinical tissue samples.* J Pathol, 2015. **237**(1): p. 123-32.

484. Li, F.X., et al., *In situ Metabolite Mass Spectrometry Imaging: New Insights into the Adrenal Gland.* Hormone and Metabolic Research, 2020. **52**(6): p. 435-447.

485. Sun, N., et al., *Mass Spectrometry Imaging Establishes 2 Distinct Metabolic Phenotypes of Aldosterone-Producing Cell Clusters in Primary Aldosteronism.* Hypertension, 2020. **75**(3): p. 634-644.

486. Urban, C., et al., *PAXgene fixation enables comprehensive metabolomic and proteomic analyses of tissue specimens by MALDI MSI.* Biochim Biophys Acta Gen Subj, 2018. **1862**(1): p. 51-60.

487. Lahiri, P., et al., *Comprehensive Evaluation of PAXgene Fixation on Oral Cancer Tissues Using Routine Histology, Immunohistochemistry, and FTIR Microspectroscopy.* Biomolecules, 2021. **11**(6).

488. Zhou, Q.Q., A. Fulop, and C. Hopf, *Recent developments of novel matrices and on-tissue chemical derivatization reagents for MALDI-MSI.* Analytical and Bioanalytical Chemistry, 2021. **413**(10): p. 2599-2617.

489. Esteve, C., et al., *Mass spectrometry imaging of amino neurotransmitters: a comparison of derivatization methods and application in mouse brain tissue.* Metabolomics, 2016. **12**(2).

490. Cao, J.H., et al., *Mass spectrometry imaging of L-[ring-C-13(6)]-labeled phenylalanine and tyrosine kinetics in non-small cell lung carcinoma.* Cancer & Metabolism, 2021. **9**(1).

491. Arts, M., et al., *Detection of Localized Hepatocellular Amino Acid Kinetics by using Mass Spectrometry Imaging of Stable Isotopes.* Angewandte Chemie-International Edition, 2017. **56**(25): p. 7146-7150.

492.   Zhao, C. and Z. Cai, *Three-dimensional quantitative mass spectrometry imaging in complex system: From subcellular to whole organism.* Mass Spectrom Rev, 2020.

493.   Maynard, J. and P. Hart, *The Opportunities and Use of Imaging to Measure Target Engagement.* Slas Discovery, 2020. **25**(2): p. 127-136.

494.   Ellis, S.R., et al., *Mass spectrometry imaging of phosphatidylcholine metabolism in lungs administered with therapeutic surfactants and isotopic tracers.* Journal of Lipid Research, 2021. **62**.

495.   Eckelmann, D., S. Kusari, and M. Spiteller, *Stable Isotope Labeling of Prodiginines and Serratamolides Produced by Serratia marcescens Directly on Agar and Simultaneous Visualization by Matrix-Assisted Laser Desorption/Ionization Imaging High-Resolution Mass Spectrometry.* Analytical Chemistry, 2018. **90**(22): p. 13167-13172.

496.   Zahraei, A., et al., *Mapping glucose metabolites in the normal bovine lens: Evaluation and optimisation of a matrix-assisted laser desorption/ionisation imaging mass spectrometry method.* Journal of Mass Spectrometry, 2021. **56**(4).

497.   Sugiura, Y., et al., *Visualization and quantification of cerebral metabolic fluxes of glucose in awake mice.* Proteomics, 2014. **14**(7-8): p. 829-38.

498.   Seaman, C., et al., *"Afterlife Experiment": Use of MALDI-MS and SIMS Imaging for the Study of the Nitrogen Cycle within Plants.* Analytical Chemistry, 2014. **86**(20): p. 10071-10077.

499.   Sugiyama, E., I. Yao, and M. Setou, *Visualization of local phosphatidylcholine synthesis within hippocampal neurons using a compartmentalized culture system and imaging mass spectrometry.* Biochemical and Biophysical Research Communications, 2018. **495**(1): p. 1048-1054.

500.   Kihara, M., et al., *Visualization of Fe-57-Labeled Heme Isotopic Fine Structure and Localization of Regions of Erythroblast Maturation in Mouse Spleen by MALDI FTICR-MS Imaging.* Journal of the American Society for Mass Spectrometry, 2017. **28**(11): p. 2469-2475.

501.   Sugiyama, E., et al., *Detection of a High-Turnover Serotonin Circuit in the Mouse Brain Using Mass Spectrometry Imaging.* Iscience, 2019. **20**: p. 359-+.

502.   Diehl, P., et al., *Lysophosphatidylcholine is a Major Component of Platelet Microvesicles Promoting Platelet Activation and Reporting Atherosclerotic Plaque Instability.* Thrombosis and Haemostasis, 2019. **119**(8): p. 1295-1310.

503.   Chen, Y. and G.J. Guillemin, *Kynurenine pathway metabolites in humans: disease and healthy States.* Int J Tryptophan Res, 2009. **2**: p. 1-19.

504.   Chiang, J.Y., *Bile acids: regulation of synthesis.* J Lipid Res, 2009. **50**(10): p. 1955-66.

505.   Glatz, J.F., J.J. Luiken, and A. Bonen, *Membrane fatty acid transporters as regulators of lipid metabolism: implications for metabolic disease.* Physiol Rev, 2010. **90**(1): p. 367-417.

506.   Kanemitsu, Y., et al., *Comprehensive and semi-quantitative analysis of carboxyl-containing metabolites related to gut microbiota on chronic kidney disease using 2-picolylamine isotopic labeling LC-MS/MS.* Sci Rep, 2019. **9**(1): p. 19075.

507.   Niehaus, M., et al., *Transmission-mode MALDI-2 mass spectrometry imaging of cells and tissues at subcellular resolution.* Nature Methods, 2019. **16**(9): p. 925-+.

508.   Barre, F.P.Y., et al., *Enhanced Sensitivity Using MALDI Imaging Coupled with Laser Postionization (MALDI-2) for Pharmaceutical Research.* Analytical Chemistry, 2019. **91**(16): p. 10840-10848.

509.   Spraggins, J.M., et al., *High-Performance Molecular Imaging with MALDI Trapped Ion-Mobility Time-of-Flight (timsTOF) Mass Spectrometry.* Analytical Chemistry, 2019. **91**(22): p. 14552-14560.

510.   Ramsey, S.A., E.S. Gold, and A. Aderem, *A systems biology approach to understanding atherosclerosis.* EMBO Mol Med, 2010. **2**(3): p. 79-89.

511.   Kleemann, R., et al., *Atherosclerosis and liver inflammation induced by increased dietary cholesterol intake: a combined transcriptomics and metabolomics analysis.* Genome Biol, 2007. **8**(9): p. R200.

512.   Sarnak, M.J., et al., *Kidney disease as a risk factor for development of cardiovascular disease - A statement from the American Heart Association Councils on kidney in cardiovascular disease, high blood*

pressure research, clinical cardiology, and epidemiology and prevention. Hypertension, 2003. **42**(5): p. 1050-1065.

513.   Karlsson, F.H., et al., *Symptomatic atherosclerosis is associated with an altered gut metagenome.* Nature Communications, 2012. **3**.

514.   Bennett, B.J., et al., *Trimethylamine-N-oxide, a metabolite associated with atherosclerosis, exhibits complex genetic and dietary regulation.* Cell Metab, 2013. **17**(1): p. 49-60.

515.   Wishart, D.S., *Metabolomics for Investigating Physiological and Pathophysiological Processes.* Physiological Reviews, 2019. **99**(4): p. 1819-1875.

516.   Wang, Z., et al., *Gut flora metabolism of phosphatidylcholine promotes cardiovascular disease.* Nature, 2011. **472**(7341): p. 57-63.

517.   Duivenvoorden, R. and Z.A. Fayad, *Utility of atherosclerosis imaging in the evaluation of high-density lipoprotein-raising therapies.* Curr Atheroscler Rep, 2011. **13**(3): p. 277-84.

518.   Van de Plas, R., et al., *Image fusion of mass spectrometry and microscopy: a multimodality paradigm for molecular tissue mapping.* Nat Methods, 2015. **12**(4): p. 366-72.

519.   Abdelmoula, W.M., et al., *Automatic 3D Nonlinear Registration of Mass Spectrometry Imaging and Magnetic Resonance Imaging Data.* Anal Chem, 2019. **91**(9): p. 6206-6216.

520.   Buchberger, A.R., et al., *Mass Spectrometry Imaging: A Review of Emerging Advancements and Future Insights.* Analytical Chemistry, 2018. **90**(1): p. 240-265.

521.   Aichler, M., et al., *Spatially resolved quantification of gadolinium(III)-based magnetic resonance agents in tissue by MALDI imaging mass spectrometry after in vivo MRI.* Angew Chem Int Ed Engl, 2015. **54**(14): p. 4279-83.

522.   Goodwin, R.J., et al., *Qualitative and quantitative MALDI imaging of the positron emission tomography ligands raclopride (a D2 dopamine antagonist) and SCH 23390 (a D1 dopamine antagonist) in rat brain tissue sections using a solvent-free dry matrix application method.* Anal Chem, 2011. **83**(24): p. 9694-701.

523.   de Korte, C.L., H.H. Hansen, and A.F. van der Steen, *Vascular ultrasound for atherosclerosis imaging.* Interface Focus, 2011. **1**(4): p. 565-75.

524.   Corti, R. and V. Fuster, *Imaging of atherosclerosis: magnetic resonance imaging.* Eur Heart J, 2011. **32**(14): p. 1709-19b.

525.   Rudd, J.H., et al., *Atherosclerosis inflammation imaging with 18F-FDG PET: carotid, iliac, and femoral uptake reproducibility, quantification methods, and recommendations.* J Nucl Med, 2008. **49**(6): p. 871-8.

526.   Lohofer, F., et al., *Mass Spectrometry Imaging of atherosclerosis-affine Gadofluorine following Magnetic Resonance Imaging.* Sci Rep, 2020. **10**(1): p. 79.

527.   Iskander-Rizk, S., et al., *Micro Spectroscopic Photoacoustic (musPA) imaging of advanced carotid atherosclerosis.* Photoacoustics, 2021. **22**: p. 100261.

528.   Porta Siegel, T., et al., *Mass Spectrometry Imaging and Integration with Other Imaging Modalities for Greater Molecular Understanding of Biological Tissues.* Mol Imaging Biol, 2018. **20**(6): p. 888-901.

529.   Capolupo, L., et al., *Sphingolipid Control of Fibroblast Heterogeneity Revealed by Single-Cell Lipidomics.* bioRxiv, 2021: p. 2021.02.23.432420.

530.   Takahashi, Y., et al., *Combination of postmortem mass spectrometry imaging and genetic analysis reveals very long-chain acyl-CoA dehydrogenase deficiency in a case of infant death with liver steatosis.* Forensic Science International, 2014. **244**: p. E34-E37.

531.   Scupakova, K., et al., *Spatial Systems Lipidomics Reveals Nonalcoholic Fatty Liver Disease Heterogeneity.* Anal Chem, 2018. **90**(8): p. 5130-5138.

532.   Kazdal, D., et al., *Digital PCR After MALDI-Mass Spectrometry Imaging to Combine Proteomic Mapping and Identification of Activating Mutations in Pulmonary Adenocarcinoma.* Proteomics Clin Appl, 2019. **13**(1): p. e1800034.

533. Xie, P., et al., *Mass Spectrometry Imaging Combined with Metabolomics Revealing the Proliferative Effect of Environmental Pollutants on Multicellular Tumor Spheroids.* Anal Chem, 2020. **92**(16): p. 11341-11348.

534. Tabassum, R., et al., *Genetic architecture of human plasma lipidome and its link to cardiovascular disease.* Nat Commun, 2019. **10**(1): p. 4329.

535. Jha, P., et al., *Genetic Regulation of Plasma Lipid Species and Their Association with Metabolic Phenotypes.* Cell Syst, 2018. **6**(6): p. 709-721 e6.

536. Didangelos, A., C. Stegemann, and M. Mayr, *The -omics era: proteomics and lipidomics in vascular research.* Atherosclerosis, 2012. **221**(1): p. 12-7.

537. Deonarine, K., et al., *Gene expression profiling of cutaneous wound healing.* J Transl Med, 2007. **5**: p. 11.

538. Kalkhof, S., et al., *Proteomics and metabolomics for in situ monitoring of wound healing.* Biomed Res Int, 2014. **2014**: p. 934848.

539. Furuta, E., et al., *Metabolic genes in cancer: their roles in tumor progression and clinical implications.* Biochim Biophys Acta, 2010. **1805**(2): p. 141-52.

540. Li, L., et al., *Transcriptional Regulation of the Warburg Effect in Cancer by SIX1.* Cancer Cell, 2018. **33**(3): p. 368-385 e7.

541. Georgakopoulos-Soares, I., et al., *EMT Factors and Metabolic Pathways in Cancer.* Front Oncol, 2020. **10**: p. 499.

542. Dewez, F., et al., *MS Imaging-Guided Microproteomics for Spatial Omics on a Single Instrument.* Proteomics, 2020. **20**(23): p. e1900369.

543. Beck, A.P. and D.K. Meyerholz, *Evolving challenges to model human diseases for translational research.* Cell Tissue Res, 2020. **380**(2): p. 305-311.

544. Bryda, E.C., *The Mighty Mouse: the impact of rodents on advances in biomedical research.* Mo Med, 2013. **110**(3): p. 207-11.

545. Kaiser, G.M., et al., *General handling and anesthesia for experimental surgery in pigs.* J Surg Res, 2006. **130**(1): p. 73-9.

546. Mestas, J. and C.C. Hughes, *Of mice and not men: differences between mouse and human immunology.* J Immunol, 2004. **172**(5): p. 2731-8.

547. Chen, Y.C. and K. Peter, *Determining the characteristics of human atherosclerosis: A difficult but indispensable task providing the direction and proof of concept for pioneering atherosclerosis research in animal models.* Atherosclerosis, 2015. **241**(2): p. 595-6.

548. Libby, P., P.M. Ridker, and G.K. Hansson, *Progress and challenges in translating the biology of atherosclerosis.* Nature, 2011. **473**(7347): p. 317-25.

549. Richmond, A. and Y. Su, *Mouse xenograft models vs GEM models for human cancer therapeutics.* Dis Model Mech, 2008. **1**(2-3): p. 78-82.

550. von Scheidt, M., et al., *Applications and Limitations of Mouse Models for Understanding Human Atherosclerosis.* Cell Metab, 2017. **25**(2): p. 248-261.

551. VanderLaan, P.A., C.A. Reardon, and G.S. Getz, *Site specificity of atherosclerosis: site-selective responses to atherosclerotic modulators.* Arterioscler Thromb Vasc Biol, 2004. **24**(1): p. 12-22.

552. Guo, S. and L.A. Dipietro, *Factors affecting wound healing.* J Dent Res, 2010. **89**(3): p. 219-29.

553. Harji, D., et al., *A systematic review of outcome reporting in incisional hernia surgery.* BJS Open, 2021. **5**(2).

554. Okur, M.E., et al., *Recent trends on wound management: New therapeutic choices based on polymeric carriers.* Asian J Pharm Sci, 2020. **15**(6): p. 661-684.

555. Dorsett-Martin, W.A., *Rat models of skin wound healing: a review.* Wound Repair Regen, 2004. **12**(6): p. 591-9.

556.   Wong, V.W., et al., *Surgical approaches to create murine models of human wound healing.* J Biomed Biotechnol, 2011. **2011**: p. 969618.

557.   Moller, N., et al., *The kidney is an important site for in vivo phenylalanine-to-tyrosine conversion in adult humans: A metabolic role of the kidney.* Proceedings of the National Academy of Sciences of the United States of America, 2000. **97**(3): p. 1242-1246.

558.   Trim, P.J., *Rodent Whole-Body Sectioning and MALDI Mass Spectrometry Imaging.* Methods Mol Biol, 2017. **1618**: p. 175-189.

559.   Ledley, F.D., et al., *Mouse Phenylalanine-Hydroxylase - Homology and Divergence from Human Phenylalanine-Hydroxylase.* Biochemical Journal, 1990. **267**(2): p. 399-406.

560.   Moro, M., et al., *Patient-Derived Xenografts of Non Small Cell Lung Cancer: Resurgence of an Old Model for Investigation of Modern Concepts of Tailored Therapy and Cancer Stem Cells.* Journal of Biomedicine and Biotechnology, 2012.

561.   Eisenhauer, E.A., et al., *New response evaluation criteria in solid tumours: revised RECIST guideline (version 1.1).* Eur J Cancer, 2009. **45**(2): p. 228-47.

List of publications

List of publications

Jianhua Cao, Benjamin Balluff, Martijn Arts, Ludwig J. Dubois, Luc J. C. van Loon, Tilman M. Hackeng, Hans M. H. van Eijk, Gert Eijkel1, Lara R. Heij, Zita Soons, Steven W. M. Olde Damink, Ron M. A. Heeren. Mass spectrometry imaging of L-[ring-$^{13}C_6$]- labeled phenylalanine and tyrosine kinetics in non-small cell lung carcinoma *Cancer Metabolism*, 2021.

Hong Liu*, **Jianhua Cao***, Benjamin Balluff, Audrey C.H.M. Jongen, Marion J. Gijbels, Jarno Melenhorst, Ron M.A. Heeren, Nicole D. Bouvy. Examination of lipid profiles in abdominal fascial healing using MALDI-TOF to identify potential therapeutic targets *Journal of Mass Spectrometry and Advances in the Clinical Lab*, 2021. *Authors contributed equally

Jianhua Cao, Pieter Goossens, Marta Martin-Lorenzo, Frédéric Dewez, Britt S. R. Claes, Erik A. L. Biessen, Ron M. A. Heeren, and Benjamin Balluff. Atheroma-specific lipids in *ldlr*$^{-/-}$ and *apoe*$^{-/-}$ mice using 2D and 3D matrix-assisted laser desorption/ionization mass spectrometry imaging. *J. Am. Soc. Mass Spectrom*, 2020.

Pieter Goossens*, Chang Lu*, **Jianhua Cao**, Marion Gijbels, Joël Karel, Erwin Wijnands, Gregorio Fazzi, Kristiaan Wouters, Evgueni Smirnov, Marc van Zandvoort, Benjamin Balluff, Marjo Donners, Ron Heeren, Erik A. L. Biessen. Integrating multiplex immunofluorescent and mass spectrometry imaging to map tissue myeloid heterogeneity in its metabolic and cellular context. *Cell Metabolism*, 2022 (Accepted)

Jianhua Cao*, Marta Martin-Lorenzo*, Kim van Kuijk, Marion J. Gijbels, Britt S. R. Claes, Ron M.A. Heeren, Judith Sluimer, Gloria Alvarez-Llamas, Benjamin Balluff. Metabolic alterations of atherosclerosis in LDLR-deficient mice using matrix-assisted laser desorption/ionization mass spectrometry imaging. (In preparation). *Authors contributed equally

Patrick A de Hoogt*, **Jianhua Cao***, Benjamin Baluff, PhD, Tim C van Smaalen, Britt SR Claes, Maarten GJ Snoeijs, Ron MA Heeren, Carine J Peutz-Kootstra. Purine and myo-inositol metabolism decrease during warm ischemia in kidney tissue: spatiotemporal detection by mass spectrometry imaging. (In preparation). *Authors contributed equally

Roel Tans, Shoumit Dey, Nidhi Sharma Dey, **Jianhua Cao**, Prasanjit S. Paul, Grant Calder, Peter O'Toole, Paul M. Kaye, Ron M. A. Heeren. Mass spectrometry imaging identifies altered hepatic lipid signatures during experimental *Leishmania donovani* infection. *Frontiers in Immunology*. 2022. (Accepted)

Lifang Zhang, Xinyue Yao, **Jianhua Cao**, Haiyan Hong, Aili Zhang, Ruiyue Zhao, Yan Zhang, Zhihao Zha, Yajing Liu, Jinping Qiao, Lin Zhu*, and Hank F. Kung. In Vivo Ester Hydrolysis as a New Approach in Development of Positron Emission Tomography Tracers for Imaging Hypoxia. *Mol Pharmaceut*. 2019.

Jianhua Cao, Yajing Liu, Lifang Zhang, Fenghua Du, Yingqian Ci, Yan Zhang, Hao Xiao, Xinyue Yao, Shengyu Shi, Lin Zhu, Hank F. Kung and Jinping Qiao. Synthesis of novel PEG-modified nitroimidazole derivatives via "hot-click" reaction and their biological evaluation as potential PET imaging agent for tumors. *J Radioanal Nucl Ch.* 2017.

Jianhua Cao, Jie Han, Hao Xiao, Jinping Qiao, Mei Han. Effect of Tea Polyphenol Compounds on Anticancer Drugs in Terms of Anti-Tumor Activity, Toxicology, and Pharmacokinetics. *Nutrients*. 2016.

Conference presentations

Jianhua Cao*, Marta Martin-Lorenzo*, Kim van Kuijk, Marion J. Gijbels,4, Britt S. R. Claes, Ron M.A. Heeren, Judith Sluimer, Gloria Alvarez-Llamas, Benjamin Balluff. "In-situ lipid alterations of aortic atherosclerosis in LDLR-deficient mice using mass spectrometry imaging". *The 90th Europe Atherosclerosis Society Congress*, Italy, 2022 (Poster presentation)

Jianhua Cao*, Marta Martin-Lorenzo*, Kim van Kuijk, Marion J. Gijbels,4, Britt S. R. Claes, Ron M.A. Heeren, Judith Sluimer, Gloria Alvarez-Llamas, Benjamin Balluff. "Correlative multimodal imaging of the in situ metabolism of atherosclerosis in *ldlr$^{-/-}$* mice" *The Correlated Multimodal Imaging COMULIS Conference*, Sweden, 2021 (Oral presentation)

Jianhua Cao*, Marta Martin-Lorenzo*, Kim van Kuijk, Marion J. Gijbels,4, Britt S. R. Claes, Ron M.A. Heeren, Judith Sluimer, Gloria Alvarez-Llamas, Benjamin Balluff. "Metabolic alterations of atherosclerosis in LDLR-deficient mice using matrix-assisted laser desorption/ionization mass spectrometry imaging". *The 89th Europe Atherosclerosis Society Congress,* 2021 (Poster presentation)

Jianhua Cao, Pieter Goossens, Marta Martin-Lorenzo, Frédéric Dewez, Britt S. R. Claes, Erik A. L. Biessen, Ron M.A. Heeren, and Benjamin Balluff. "Atheroma-specific lipids in *ldlr$^{-/-}$* and *apoe$^{-/-}$* mice by MALDI-MSI". *The 88th Europe Atherosclerosis Society Congress*, 2020 (Poster presentation)

Jianhua Cao, Pieter Goossens, Marta Martin Lorenzo, Frédéric Dewez, B.S.R.Claes, Erik Biessen, Ron M.A. Heeren and Benjamin Balluff. "Investigation of atheroma-specific lipids using 3D-MALDI-MSI". *The OurCon VII Conference*, France, 2019 (Oral presentation)

Jianhua Cao, Pieter Goossens, Marta Martin Lorenzo, Klára Ščupáková, Frédéric Dewez, Erik Biessen, Ron M.A. Heeren, and Benjamin Balluff. "Three-dimensional mass spectrometry imaging of lipids in mouse aortic atherosclerotic plaque". *The 87th Europe Atherosclerosis Society Congress*, The Netherlands, 2018 (Poster presentation)

Jianhua Cao, Pieter Goossens, Klára Ščupáková, Marta Martin Lorenzo, Frédéric Dewez, Erik Biessen, Ron M.A. Heeren, and Benjamin Balluff. "Three-dimensional mass spectrometry imaging of lipids in atherosclerotic plaque". MSBM, Croatia, 2017 (Poster presentation)

Acknowledgements

It was always my dream to study in a very different country, experience distinct cultures, and meet different people in a very international environment. On September 24th 2017, I took my first international flight from Beijing (China) to Amsterdam (The Netherlands) to fulfill my international dream. I still remember how excited I was when I finally landed in Amsterdam and people were saying 'Hoi' to me. It was also an unforgettable experience to take the train in the NL for the first time from Amsterdam to Maastricht. Finally, I arrived at Maastricht and started my new life in M4i. I cannot believe I have already been here for more than 4 years and I have finished my Ph.D amid the COVID-19 pandemic.

Pursuing a PhD as an international student is very challenging, especially during the pandemic. Aside from overcoming research related difficulties, we also face many unspeakable issues in daily life. For instance, many Chinese students were living in fear because of a surge in anti-Asian hate crimes all over the world during the pandemic. I did not go back to my country for more than 3 years due to the coronavirus. This unexpected onslaught of the COVID-19 has shaken humanity to its heart, forcing us to rethink how we socialize, study, learn, protect ourselves, respect and take care of other people.

During the past 4 years, I have met so many amazing people who treat me like family. They helped me so much not only in research but also in life. I would like to express my gratitude to them in this chapter, even though it is impossible to cover everything I want to say.

Ron, firstly, thank you very much for giving me the opportunity to work in M4i. Your wisdom and attitude towards science and life always inspire me. Your incredible leadership and communication skills are continuously motivated me to learn and grow. I have to admit that I had a lot of difficulty speaking English at beginning of my Ph.D. and I felt very hard with a big cultural difference. You are constantly so kind and generous to give me space and time to adapt and improve, as well as help me as much as you can. Thank you so much for all the trust, patience, and supervision in science and in life. In addition, I appreciated a lot for the serious research discussion and so many casual conversations with you. Your compliments will stimulate me at all times to be a better person in every aspect in future.

Benjamin, thank you very much for being my daily supervisor taking care of me on different projects and daily routine. I have learned so much from you about how to do research, how to write scientific papers and funding proposals, as well as how to prepare and give a good presentation. You encouraged me and helped me all the time during my Ph.D. I will never forget that you helped me get the opportunity to have a short-term research stay in Spain. Moreover, I still remember so clearly that you gave me a lot of compliments and encouragement after oral presentations I gave and various small improvements I obtained. I am unfailingly grateful for all the positive feedback you gave to me as a researcher and as a person. You are an incredible supervisor and scientist. Thank you for having me as your student.

Marta, my Spanish sister, it is so extraordinary to know you as a lovely friend and as a great coworker. We knew each other because you were a postdoc of Benjamin's team. Our

friendship got stronger after I moved to your office. I was super lucky to have you around for almost two years. You were always there for me no matter what happened, especially during the hardest time in the first year of my Ph.D. I was super sad and felt so lost when you left M4i and went back to Madrid. However, you were still helping me out via WhatsApp or email when I have questions, even during weekends or holidays. Interestingly, I met you, Gloria and Aranzazu at the 87th EAS Congress in Maastricht again! We were joking that I will go to Madrid to do metabolomics one day. I cannot believe it was happening during pandemic 2021! Even though we went through many unbelievable difficulties before managing to go to Madrid and afterwards, I had so much fun in Madrid no matter in research or life in general (great weather, food, and drinks) with many stunning Spanish people. All the best to you!

Britt (*Britt Suzanne Robin Claes* or *Britt Beer Bread Claes*), my favorite gym buddy and my dear friend. I still remember you came to my office 4 years ago and talked to me for the first time when you were doing your master in M4i while I was just starting my Ph.D., but I do not remember how many times I asked you "what is your name again" (everybody knows I am super bad at names in general). I was so excited when you told me that you would start your Ph.D. in M4i too. Seriously, I really cannot imagine my Ph.D. life without you since you helped me almost in every project! You are super hardworking, independent, caring, funny, and positive. You are an amazing team player, great researcher, and sweet friend! I have learned so many things from you, especially your strong ability to handle hard situations and bad feelings during work. In daily life, you are such a great listener to hear my concerns and help me whenever I need you. I always feel so lucky to have you around from the beginning to the end of my Ph.D. You are always there for me! Thank you very much for everything!

Fred, we knew each other because we shared the same daily supervisor, and we were all living in the same neighborhood 'De Heeg Chinatown'. You are the first person in M4i to show me how to use HTX, rapiflex, etc. You also helped me get my PC in the office at the beginning of my Ph.D. You were always willing to help me when you were around, especially during the pandemic! I feel so grateful that I could share with you not only my happiness but also my sadness whenever and wherever I want. I appreciated so much that you always say that I am too funny and the best Chinese ever to everyone, even though I still cannot pronounce your name correctly. I am also glad that my Chinese friends gave you a great impression. Moreover, I will never forget that you chose Chinese restaurants to celebrate your several birthdays. In addition, the swimming training you gave me was super impressive! Last but not least, thank you for teaching me how to drive your car. You know I can talk and make fun of you endlessly…Nevertheless, I will end this paragraph with your favorite sentence "Les Français appartiennent à la Chine! bah c'est bien".

Pmax, you are the first French I know who is super interested in the culture, language, and food (which is the most important for you) of China. I am still very impressed that you

traveled to more cities in China than I did. As a researcher, you were super talented, hardworking, open-minded and willing to help anyone if you can. As my friend, I have to admit that you are an awesome friend anyone could ever have. You are authentic and honest. I will never forget that you helped me many times to improve my presentation skills at the beginning of my Ph.D. Moreover, whenever I was working late, you were always there to support me. You are always so patient to listen to any concern I had and you care about me on all occasions. I have to admit that the casual chitchatting with you has improved my English a lot (hahaha). Furthermore, I am very glad that you joined the trip to Spain in 2019 with a group of Chinese friends and had a lot of fun. In addition, I will never forget that you visited me and Marta when I was in Madrid in 2021. The trip to Granada with you was also so incredible. Thank you for having me as a friend and I wish you all the best for everything.

Florian, I hope you will not get upset because I said thank you to Fred and Pmax before you, hahaha. 'YOU WORRY NOT'. You are also my great friend and my beautiful brother! During my Ph.D., you always encouraged and helped me in many aspects. You always be patient to answer any question I had even after you started your new job. As a coworker, you were hardworking, ambitious, empathetic, and super funny. Your great skills at PowerPoint and presentation are always inspired me. Moreover, I still cannot believe your parents gave me so many delicious Macaron when they were visiting you! It was my great pleasure to talk with them during your defense party, even though you had to act as a translator. In addition, I have to say that your girlfriend **Fanny** (she is super nice) makes you an even more amazing person! Thank you for being my friend and sharing so many unforgettable moments during my Ph.D. Good luck for your new career!

Maxime, you are the quietest French compared to the others and the great listener ever as a friend (not just colleague, haha). You always told me that I should do meditation regularly as you do, however, I cannot stop laughing whenever I tried to do meditation. Additionally, many thanks for the unforgettable ice cream (dark chocolate) gathering in Chinatown together with Fred and Charles in the 2020 summer. I am super appreciative to know you and your rock (**Nina**, the best girl for Maxime) during my Ph.D. Even though I was always making fun of you about your interesting rule of 'colleague' and 'friend', you are always my great friend in my deep heart!

Naomi, as you said, your name was the first one I remembered at the beginning since it was kind of 'Chinese', haha. As a scientist, you are super hard working and talented. You are the one to give me the training of rapiflex, and now I was the one responsible for it! As a friend, you are always kind to me and always encourage me. I will never forget the first swimming course you gave in Maastricht. Moreover, I am so glad that you joined me when I got my first piercing in my life (OMG, the left gun and the right gun were shooting my ears at the same time). Thank you very much for being my friend and all the best for you!

Bea, my another Spanish sister, it was my great pleasure to know you at M4i too! You are always super nice, kind, and willing to help at any time. I was super happy when you visited

me in Madrid during the pandemic, because we did not see each other for almost 3 years. A few weeks later, I visited you back in A Coruña, you and your **Dani** showed me around your middle school, high school, your village, and even the research center you worked. Madre Mía! te pienso to puto día! The ocean, the food, and the drink… You and Dani treated me like family, I had so much fun! The experience I had was so invaluable, thank you very much to be my great friend and family in Europe! All the best for you and Dani.

Anjusha, my sweet friend from India, you are always the sweetest with your very sweet voice (you knew that I could never talk as gently as you do). I have to admit that you are the first Indian friend I made. I am still surprised we can become such great friends even though we have so different personalities. I guess it might considerably relate to that we are all nice people and you are also living in "Chinatown"! I am very glad to know you at M4i, your passion for instrumentation inspired me all the time since I think it is super difficult! You are very talented, resilient and determined to stand up for what you believe in. As my friend, you are always so patient to listen to my difficulties in life, and you unfailingly try to encourage me and come up with good ideas to make me happy. I am so glad that you feel comfortable to open your heart to me and I am almost an open book for you. Thank you so much for sharing so many great moments with me in Maastricht. We will keep in touch with each other forever. All the best for your Ph.D. and future career.

Charles, you are the only French in M4i so far. You are as nice as the other French friends I have! Thank you for showing me around Lille and meeting the other French this year. Thank you very much for all the coffee break sessions, the Chinatown party with your best friends from France, and your *Inspire* team. I am so happy that you joined M4i since the other French have left. You are so talented, hardworking, and caring person. You are always there for me during my hardest time the last year. I am very grateful to you for all your help. I always believe that a true friend shows empathy to each other and support each other consistently through ups and downs! Everyone deserves a real friend like you! Moreover, your girlfriend **Camille** is a very amazing girl. I am very lucky to know her and I am so happy to be invited to attend your wedding next year! I wish you all the best for your Ph.D.!

Bryn, thanks for all the genuine encouragement you gave to me during my PhD. I remembered that you are the first person told me that my first paper has been published online and you were so proud of me! Thank you for all the help with suncollect, solarix or any instrument in our lab! You are the best we could have in M4i and I am so happy that you are back to M4i again! All the best for you!

Tiffany, I am also very grateful to know you and your husband **David**. The French food you made was very delicious. I wish you all the best in your new career in Germany.

Sylvia, thank you for helping me with the special crime document (you know what I mean (❀´‿`❀)) to go to Spain in 2021. Good luck for everything!

Thank you to people from pathological department. **Erik**, thank you for all the kind supervision for the collaboration project! **Pieter**, thank you for all the help and all the encouragements! Thank you **Chang** (感谢一直以来的支持和帮助！希望一切顺利！), **Marion**, **Kim**, **Judith**, **Patrick**, **Carine**, and **Maarten**. Thank you very much for all the support during my Ph.D.

Thank you to people from Surgery department. **Steven**, thank you for offering the isotopic labeling project and thank you for all the encouragements and help! Thank you **Hong** (师兄，感谢一直以来的帮助和支持), **Lin** (陈琳, 感谢在博士最后几个月收留我， 虽然我们会因为各种乱七八糟的小事争吵，我知道我们都是善良的人。不管博士有多难，希望你相信自己，坚持到最后, 我知道我们肯定行!), **Xinwei** (**新伟**， 恭喜你已经是博士了! 希望你在广州一切都好!), **Min** (邓敏，从来没有见过对家庭如此用心的男生! 感谢所有的帮忙，马上也要毕业了，加油啊! 你一定可以), **Xiu-Xiang** (秀香，感谢在论文封面上的帮助，感谢一起旅行的日子，希望你以后一切顺利!), **Yan** (孙妍，感谢你所有的鼓励和帮助，很高兴能认识你这样志同道合的朋友。希望你实现所有你想要实现的愿望!). **Annet** (thank you for all the help for everything and hotpot sessions; Je bent geweldig!), **Marissa** (We had so much fun when you were around, thank you very much for all the help at beginning of my Ph.D.), **Yvonne** (Thank you for cooking the 1st dutch meal for me. It was so amazing to know you and your husband), **Sanaz** (thank you for all the fun time before covid), **Renee**, **Evie** (thank you all the kind words and fun time), **Merel**, **Alexander**, **Mirjam**, **Kees**, **Bas**, **Mo**, **Sander**, **Annemarie**, **Jorne**, and **Lars**.

Thank you very much for my officemates, **Anna** (beautiful karaoke girl, Justin Bieber fan, Picture perfect, you don't need filter. Thank you for always being sweet), **Aurelia** (fashion girl, you are amazing), **Sade** (7 am at Gym while everyone is sleeping), **Zaid** (What's up man? Gentlemen with mixed blood and great personality), and **Francesca** (sweet girl with sweet voice). It was always so much fun in the office. You are so amazing to make the office feel like a home. I will never forget all the nice moments we had together. "No more CRAZY NEW YEAR, Alsjeblief 2022".

"¡Vaya, vaya! (aquí no hay playa), jajaja!!!". Muchas gracias **Gloria** (eres un líder de grupo increíble y mis mejores deseos para tu hermosa familia); **Aranzazu** (¡Eres una chica genial con un corazón súper hermoso! ¡Por favor guárdelo!); **Ariadna** (Espero que aún recuerdes cómo escribir tu nombre chino); **Mirjam** (¡Créeme! ¡Eres maravilloso!); **Alma** (Eres tan hermosa como tú nombre; tienes un novio increíble; tu ciudad natal es súper hermosa y tus amigos son súper amables; Todavía estoy emocionado de ser invitado a tu increíble defensa de doctorado); **Sergio** (el mejor español de todos los tiempos); **Emilio** (Un gran futbolista y un apuesto científico); **Vanesa** (Eres super amable. Fue un placer conocerte).

I would also thank two special coaches from UM sports, **Lieke** and **Jack**, thank you for giving me great training to make me stronger. Thank you very much for all the chatting time. I should start training as soon as possible!

最后，非常感谢我的中国亲友们。**罗倩**，感谢在博士开始几个月收留我，没有你我都不知道怎么开始我的艰难博士生涯。希望你在山东一切都好。**路畅**和**丁玲玲**，感谢你们和我一起旅游，一起过圣诞的日子！谢谢**雅文**（我们可是一起来的大荷兰啊！），谢谢**泺潼**，希望你在英国一切都好。

最后，感谢我的**家人**，没有你们，就没有我的现在，我一直很愧疚不能在你们需要的时候陪在你们身边，以后要多陪陪你们！

Curriculum Vitae

Jian-Hua Cao (曹建花)

I was born in the west of Shanxi province, People's Republic of China. After graduating from high school in 2010, I moved to Taiyuan (the capital of Shanxi Province) to pursue a Bachelor of Science in chemistry. During my bachelor, I was honored to receive an Outstanding Undergraduate Research Funding to investigate the synthesis and characterization of conjugated compounds containing triphenylamine for 2 years under the supervision Prof. Zhao Zhang.

After obtaining my bachelor degree in 2014, I moved to Beijing to pursue my master's degree in medicinal chemistry and molecular engineering at the National Key Laboratory of Radiopharmaceuticals. There I have mainly studied radiopharmaceuticals for positron emission tomography imaging of cancer and neurodegenerative diseases under the supervision of Prof. Lin Zhu and Dr. Jinping Qiao. During my bachelor and master studies, I have been awarded many times the National Academic Scholarships and National Endeavor Fellowships.

Afterwards, I started my Ph.D. at the Maastricht Multimodal Molecular Imaging Institute (M4i), Maastricht University, The Netherlands, under the supervision of Prof. Ron M.A. Heeren and Dr. Benjamin Balluff. Since then, I have focused my research on investigating the *in situ* metabolism of different diseases (atherosclerosis, lung cancer, and wound healing) using matrix-assisted laser desorption/ionization mass spectrometry imaging. During my Ph.D., I obtained a COST (European Cooperation in Science and Technology) STSM (Short-term Scientific Mission) research fellowship to visit the IIS-Fundación Jiménez Díaz in Madrid (Spain) for 3 months. There I focused on a translational study to identify atherosclerotic markers under the supervision of Dr. Gloria Alvarez-Llamas and Dr. Marta Martin-Lorenzo.

In January 2022 I started as a postdoctoral fellow to investigate leishmaniasis under the supervision of Prof. Ron M.A. Heeren (M4i) and Prof. Paul Kaye (York University, The United Kingdom). In this project, I am focusing on correlating lipidomics, mass spectrometry imaging, and spatially resolved proteomics and transcriptomics for a more holistic understanding of this tropical infectious disease.